SYNTHESIS, SPECTROSCOPIC, AND THERMODYNAMIC STUDY OF URANYL AND NEODYMIUM PHOSPHATE SOLID PHASES

By

CHRISTOPHER ROBERT ARMSTRONG

A dissertation submitted in partial fulfillment of

the requirements for the degree of

DOCTOR OF PHILOSOPHY

WASHINGTON STATE UNIVERSITY

Department of Chemistry

DECEMBER 2009

To the Faculty of Washington State University:

The members of the Committee appointed to examine the dissertation of CHRISTOPHER ROBERT ARMSTRONG find it satisfactory and recommend that it be accepted.

_____

Sue B. Clark, Ph.D., Chair

_____

Kenneth L. Nash, Ph.D.

_____

Peter R. Griffiths, Ph.D.

_____

James O. Schenk, Ph.D.

ACKNOWLEDGEMENTS

I acknowledge the following people, without whom the work presented herein would not have been possible. I gratefully acknowledge my advisor, Dr. Sue Clark, for her guidance, patience and support; and for giving me the latitude to explore my own research interests. Dr. Ken Nash is thanked for his good-natured attitude, exemplary editorial skills, and simply for teaching me so much about solution chemistry and solvent extraction. Dr. Peter Griffiths is thanked for sharing his incredible knowledge in the field of IR spectroscopy. Many of the scientific findings presented in this dissertation are directly related to the knowledge he has shared with me. Dr. Louis Scudiero is acknowledged for his assistance with running the TGA and DSC instruments, and Dr. Andrew Felmy is thanked for his help with thermodynamic interpretations. Lastly, I acknowledge all of the members, past and present, of the Clark, Nash, Benny and Wall groups at WSU. The help, guidance and support I received from them are immeasurable.

SYNTHESIS, SPECTROSCOPIC, AND THERMODYNAMIC STUDY OF URANYL AND NEODYMIUM PHOSPHATE SOLID PHASES

Abstract

by Christopher Robert Armstrong, Ph.D.

Washington State University

December 2009

Chair: Sue B. Clark

Hydrated uranyl phosphates comprise some of the most refractory U-bearing minerals in oxidizing environments. As such, these solids are expected to precipitate where in-situ phosphate amendments are employed in contaminant remediation scenarios. However, the structure, stability, and mechanisms by which these hydrated uranyl phosphates form are not well understood. The work presented herein is largely focused on (1) synthesis of a suite of hydrated uranyl phosphates, (2) characterization of these phases using a variety of analytical techniques, (3) analysis of the solution phases associated with the solids that form, and (4) development of thermodynamic data for these hydrated uranyl phosphates. In a related study, the uptake of the lanthanide cation neodymium onto hydroxylapatite (HA): $Ca_5(PO_4)_3OH$ was also investigated.

The following novel contributions are presented in this study.

1. We synthesized, for the first time, the mixed actinide and lanthanide phosphate, francoisite-(Nd):$Nd[(UO_2)_3OOH(PO_4)_2)]\bullet 5H_2O$.
2. The transformation of chernikovite: $H_3O[(UO_2)(PO_4)]\bullet 4H_2O$ into triuranyl diphosphate tetrahydrate (TDT):$(UO_2)_2(PO_4)_3\bullet 4H_2O$ was demonstrated.
3. The solubility of triuranyl diphosphate tetrahydrate (TDT) was measured at 23 and 50^oC, and we report the first log Ksp data for elevated temperature.
4. The energetics of hydration were investigated for the natural meta autunite mineral $(Ca[(UO_2)(PO_4)]_2 \bullet 6.5H_2O$ and synthetic sodium autunite: $Na_2[(UO_2)(PO_4)]_2 \bullet 3H_2O$.
5. We show that the uptake mechanism of Nd onto HA is highly pH dependent. Whereas at high pH (ca. 10), isomorphic Nd-Ca substitution is observed, at lower pH (ca. 4), the precipitation of a discrete hydrated $NdPO_4$ phase is evidenced.

TABLE OF CONTENTS

LIST OF FIGURES

LIST OF TABLES

ATTRIBUTIONS

All of the work reported in this dissertation was conducted by myself in consultation with the following people. My advisor, Dr. Sue B. Clark and committee members, Drs. Kenneth L. Nash and Peter R. Griffiths share authorship of the work presented in Chapter Two. Chapter Five acknowledges Drs. Andrew R. Felmy and Sue B. Clark as coauthors. Dr. Sue B. Clark and I share exclusive authorship in all of the other submitted manuscripts (Chapters Three, Four, Six and Seven) resulting from this dissertation.

CHAPTER ONE

INTRODUCTION

1.0 Actinide Contamination

The development and production of nuclear weapons and energy in the United States has resulted in significant contamination to soil and groundwater systems (Abdelouas et al., 1999). Nuclear waste packages that come in contact with groundwater are susceptible to corrosion resulting in the release of radionuclides into the biosphere. Comprising the most abundant radionuclide in U.S. Department of Energy (DOE) complexes, Uranium is present in the soil and groundwater of twelve DOE sites (Wellman et al., 2006). Although in many cases the oxidation of U(IV) to U(VI) results in the formation of refractory U mineral phases, the exact mechanisms of U(VI) incorporation and the structure and stability of these phases are not well understood.

Addressing some of these problems, particularly as they pertain to U(VI) phosphates, is the key motivation for the research presented in this dissertation. The following sections discuss recent studies that have been carried out pertinent to the work undertaken in this thesis, followed by a discussion of additional research that needs to be addressed, thereby providing the reader with a brief overview of the salient topics presented in this work. The bulk of the experimental studies carried out in the following chapters pertain to the chemistry of hydrated uranyl phosphates. In addition, a related study of f-element and apatite interactions is also presented.

1.1 U-bearing phosphate mineral stability

In a study investigating the long-term stability of U phosphate mineral phases in natural systems, Jerden et al. (2003) examined the paragenesis of U-bearing mineral phases at the Coles Hill

uranium deposit, Virginia. These workers reported that dissolved U was effectively sequestered due to the oxidation of relatively abundant uraninite ($U^{IV}O_2$) and subsequent U^{6+} phosphate precipitation. Jerden et al. (2003) further concluded that the natural system had reached a steady state with respect to U mobility, and by extrapolationg their experimental findings, they estimated a time-scale of U-phosphate (meta autunite) stability to be 250,000 years.

1.2 U-bearing mineral crystal structures

Using primarily single crystal x-ray diffraction (XRD), Burns and coworkers (Burns et al., 1999; Burns, 2005) presented a comprehensive overview of the topologies of a variety of uranyl bearing minerals. The uranyl phosphates generally comprise the least soluble suite of uranyl minerals (Gorman-Lewis, 2008). As such, detailed structural characterization of these materials has been carried out by several workers (Locock and Burns, 2002; Locock and Burns, 2003a; Burns, 2005; Bray et al., 2008; Yu et al., 2008; and references therein). Of these uranyl phosphates, the autunite mineral family has received the most attention, including single crystal XRD studies to determine the structure of mono- (Locock et al., 2004), di- (Locock and Burns, 2003b) and trivalent (Khosrawan-Sazedj, 1982) autunite minerals. Using the anion topology developed by Burns et al. (1996), these workers showed that the autunite mineral system is composed of sheets containing uranyl square bipyramids bound to phosphate tetrahedra via oxygen atoms. These polyhedra typically share vertices and are structurally similar to the uranyl silica group uranophane. In all cases, cations coordinated by varying numbers of water molecules are located in the interlayer. The hydrated cation in turn is bonded to either the phosphate or uranyl oxygen (or both) via long range electrostatic attraction or more directly through oxygen bridging (Burns, 1999). Locock and Burns (2002) also determined the crystal structure (orthorhombic crystal system) of synthetic triuranyl diphosphate tetrahydrate (TDT:

$(UO_2)_3(PO_4)_2{\cdot}4H_2O)$). It is comprised of the uranophane anion sheet topology. As such, the crystal structure of TDT consists of sheet-like motifs of pentagonal uranyl bipyramids coordinated by phosphate tetrahedra via oxygen bridges (Fig. 1). In contrast to the autunite family, however, the uranyl and phosphate groups in TDT share oxygen edges. In addition, a uranyl bipyramid occupies the "interlayer" resulting in an open framework structure. Recent uranyl phosphate structural studies have extended these investigations to include interstitial organic ligands, such as $C_6H_{14}N_2^{2+}$ (Bray et al., 2008) and 4,4'-bipyridyl (Yu and Albrecht-Schmitt, 2008) and mixed-metal uranyl compounds (Yu et al., 2008).

1.3 U-bearing mineral solubility

In oxidizing environments, uranium primarily occurs in the hexavalent state as the uranyl cation (UO_2^{2+}). As noted above, spent nuclear fuel corrosion can result in the precipitation of highly stable uranyl solids (Abdelouas et al., 1999). Of these minerals, the oxides, silicates, and particularly the phosphates are the most stable, and thus are expected to comprise important sinks for uranium under oxidizing conditions. Consequently, several experimental studies have been conducted on the solubility of the more common naturally occurring uranyl-bearing minerals such as uranyl phosphates (Vesely et al., 1965; Markovic et al., 1983; Felmy et al., 2005; Rai et al., 2005), silicates (Nguyen, et al., 1992; Ilton et al., 2006; Gorman-Lewis et al., 2007), oxy-hydroxides (Rai et al., 2002; Giammar and Hering, 2002) and carbonates (Meinrath et al., 1993; Elless and Lee, 1998).

However, thermodynamic data obtained from experimental solubility studies of U^{6+} solids yield log K_{sp} values that are in some cases highly disparate (Gorman-Lewis et al., 2008). Slight physico-chemical variations in the solid (e.g., degree of crystallinity, particle size, natural

vs. synthetic sample, chemical impurities etc.) can lead to very different results (Gorman-Lewis et al., 2008). In addition, quantification of the aqueous hydrogen ion concentration is often improperly conducted leading to significantly erroneous measurements. Moreover, inadequate characterization of both the initial solid and the final equilibrated solid can lead to misleading interpretations. In this dissertation (Chapter 4) we show that under favorable conditions, complete structural transformation of one hydrated uranyl phosphate into another occurs. Hydrothermal treatment caused a complete reorganization in the structural unit, whereby uranyl square bipyramids (in chernikovite) converted to uranyl pentagonal bipyramids (in TDT). This finding stresses the importance of rigorously characterizing both the starting material and the end product, particularly in thermodynamic studies that involve variations in the physico-chemical conditions of the aqueous systems, e.g., temperature and/or ionic strength. Thus, one aim of this study is to conduct a thorough characterization of both the starting material and the end product in solubility studies with varying ionic strength and temperature, as described in detail in Chapter 5 of this dissertation.

1.4 The role of water in hydrated oxysalts

One of the main goals of this study is to delineate the different roles of water in the hydrated uranyl phosphates investigated in this dissertation. To this end, we have adopted the operational definitions of water initially developed by Hawthorne (1992), and later expanded to include uranyl oxysalts by Schindler and Hawthorne (2008). For hydrated oxysalts, Hawthorne defined a structural unit and an interstitial complex. The structural unit is the "backbone" of the solid (i.e., the sheet) where the majority of the covalent bonding takes place. In our case the structural unit comprises the uranyl and phosphate polyhedra. The interstitial complex (i.e., the interlayer)

effectively stitches the two-dimensional structural units together, comprising variably bonded and oriented water molecules and polyvalent cations.

In hydrated oxysalts, water typically resides in the structural unit, coordinated to the metal cation, and in the interstitial complex, either directly coordinated to the interstitial metal or occupying available free space, held in place by hydrogen bonding (i.e., occluded). In addition, water is also present in hydrated oxysalts on the surfaces of the solid due to physisorption, effectively in equilibrium with atmospheric water.

Water is thus delineated into four categories:

i. Structural water (within the sheet)
ii. Interstitial (coordinated) water (within the interlayer)
iii. Occluded water (within the interlayer)
iv. Physisorbed water

The crystallographic structure of TDT is shown in Fig. 1 (Burns, 2005). The image at left shows the open framework structure of TDT consisting of i) the structural unit in which lateral chains of uranyl pentagonal bipyramids (yellow) and phosphate tetrahedra (grey) are bonded (along z-axis) and, ii) the interstitial region (interlayer) consisting of uranyl pentagonal bipyramids sharing vertices with phosphate tetrahedra in the structural unit (along y-axis). The structural unit is not hydrated; however, the interstitial uranyl bipyramids are coordinated by three water molecules (interstitial water). In addition four "free" water molecules are present in the open spaces between the uranyl polyhedra (occluded water) held in place by hydrogen bonding. These occluded waters are not shown in Fig. 1. The image at right depicts the structure of the two dimensional sheet, composed of edge-sharing phosphate and uranyl polyhedra. Bonding between the vertices of adjoining phosphate and uranyl polyhedra effectively bonds the chains into a two-dimensional sheet-like structure (x-axis).

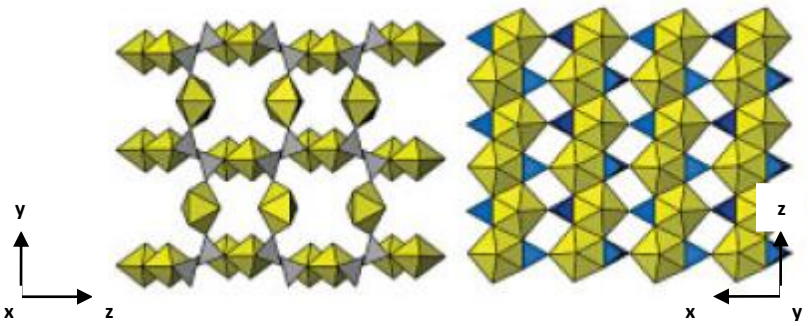

Fig. 1. Crystallographic structure of triuranyl diphosphate tetrahydrate (TDT) (Burns, 2005).

The assignment of water in synthetic materials and minerals is a challenging problem. Different conventions are used to define water in these solids; and the different approaches are somewhat contradictory. For example, using thermogravimetric analysis (TGA), the Vochten group concluded that all water not observed above 60^{o}C was due to physisorption and, therefore, are not included in the empirical formula, and that all water present above 60 ^{o}C was stoichiometric water (Vochten et al., 1984). Others include the waters below 100^{o}C in the empirical formulas (Rai et al., 2005). Unfortunately, for complex materials such hydrated uranyl oxysalts, "the increase in complexity comes with an increase in ignorance" (Hawthorne and Schindler, 2008).

A principal goal of this thesis is to delineate water such that specific populations are reflected in the empirical formula of the material following the Hawthorne method. As such, with the exception of physisorbed water, all other water populations are included in the empirical formula. For example, take the mineral metavoltine (Hawthorne and Schindler, 2008),

$K_2Na_6Fe(H_2O)_6[Fe_3O(SO_4)_6(H_2O)_3]_2(H_2O)_6$. Here the formula clearly delineates stoichiometric water. The first water group (from left to right) represents interstitial-coordinated, the second water group is indicative of structural water and the last water group is attributed to weakly bound (occluded) interstitial water.

1.5 Spectroscopic studies

With the exception of recent Raman studies as described below, vibrational spectroscopic investigations of uranyl phosphates have received little attention. Cejka (1999) presented a thorough overview of all the available thermal and IR studies for U-bearing minerals. Pham-Thi and Colomban (1985) conducted an exhaustive study investigating a trio of hydrated uranyl phosphates, including TDT and chernikovite, $H_3O[UO_2PO_4]\cdot 4H_2O$. These workers provided both IR and Raman data on these phases. The Vochten group reported a series of U-mineral IR studies (Vochten et al., 1984; Vochten, 1990; Van Haverbeke et al., 1996). More recently, the Frost group has conducted numerous Raman spectroscopic investigations on uranyl-bearing minerals (Frost and Weir, 2004a; Frost et al., 2004b; Frost et al., 2006a; Frost et al., 2006b).

1.6 Apatite Minerals

Apatites are ubiquitous in nature and are present in igneous (Piccoli and Candela, 2002) sedimentary (Knudsen and Gunter, 2002) and metamorphic (Spear and Pyle, 2002) regimes. Hydroxylapatite, $Ca_5(PO_4)_3OH$), fluorapatite ($Ca_5(PO_4)_3F$) and chlorapatite ($Ca_5(PO_4)_3Cl$) represent the three end members in the apatite mineral family; and all of these minerals are stable in soil environments (Bruno et al., 1995; Finch and Murakami, 1999; Jerden et al., 2003).

Apatite readily incorporates a host of polyvalent metals and anionic complexes while retaining the same overall crystal structure (isomorphic substitution). In fact, apatite accommodates half of the periodic table into its lattice arrangement (Hughes and Rakovan, 2002). Additionally, apatites are very important in biological systems. Hydroxylapatite (HA) is the main constituent in bones and teeth accounting for about 1% of our body weight (Huminicki and Hawthorne, 2002). It was initially believed that metal ion uptake by apatite was predominantly electrostatically-driven, since the apatite surface exhibits a point of zero charge (PZC) at pH ca. 8 (Bell et al., 1972). However, it has since been recognized that the process(es) governing metal ion and apatite interactions is more complicated, as discussed below.

1.7 f-element – HA Interactions

The application of apatite phases in natural systems for the removal of transition metals has been extensively studied. However, research focusing on actinide and lanthanide interactions with apatite is rather limited.

In one of the earlier U-apatite studies, Jeanjean et al., (1995) determined that HA dissolution and subsequent U precipitation was the most important metal removal mechanism compared to a sorption process. In separate studies on the use of apatite as a contaminant remediation strategy, Fuller et al. (2002, 2003) concluded that the predominant uptake mechanism of U onto apatite was sorption followed by precipitation. These authors observed almost complete U removal from the system. The initial predominant uptake mechanism was sorption; however, as the concentration of U increased at the surface of the solid, a positive local saturation index resulted in the rapid precipitation of U-bearing phosphate phases. In a similar study of uranyl uptake by apatite, Ohnuki et al. (2004) observed sorption followed by surface

mineralization as autunite precipitated on the surface of apatite even though the bulk solution was undersaturated with respect to autunite. Workers from Florida State University (Thakur et al., 2005) conducted additional uranyl-hydroxylapatite investigations. This study was the first to present sorption edge curves as a function of pH for uranyl sorption onto hydroxylapatite. Very little data exists for lanthanide uptake by HA; however, in an investigation of apatite sequestration of Eu^{3+} and uranyl, Knox et al. (2003) observed complete metal ion removal by apatite and provided partition coefficient data (Kd) as evidence to support a sorption hypothesis.

It is evident that systems involving the removal of metals by apatite phases are highly complex. Such metal characteristics as oxidation state, ionic radius, coordination number, hard or soft acid character all contribute to the process by which a given metal is sequestered by apatite. Solution/suspension pH, background electrolyte and temperature are also very important factors (Xu et al., 1994 and references therein).

1.8 Lanthanide phosphate minerals

Lanthanides account for approximately 40% of the total mass of uranium fission products. In addition, these rare earth elements (REE) are reasonable chemical analogues of trivalent actinides such as Am^{3+}, Cm^{3+}, Pu^{3+}, etc. (Choppin, 1983; 1986; 1989; Nitsche, 1990).

A significant proportion of mined phosphates are obtained from lanthanide phosphate minerals (e.g., $REE(PO_4)$ (s)). Such phosphates exhibit a 1:1 REE to phosphate ratio, and are highly stable and ubiquitous in nature (Boatner, 2002). Monazite, the mineral name assigned to the light rare earth (LREE) orthophosphates (e.g., La, Ce, Nd), incorporates a variety of cations into its structure. Not only is monazite economically important for acquiring LREE, but U and Th are also extracted from monazite (Boatner, 2002).

1.9 Research and Objectives

The following is a summary of the objectives of this study:

1. Develop an effective analytical strategy to rigorously characterize synthetic and natural hydrated uranyl phosphates.
2. Define and delineate the roles of water in hydrated uranyl compounds.
3. Investigate the energetics of both natural and synthetic U-phosphates, including studying the thermodynamics of hydration and solubility at elevated temperature.
4. Investigate the processes and mechanisms controlling the partitioning of Nd to HA as a function of pH.

1.10 Overview

The following chapters are a collection of individual research topics, each of which is written in manuscript format for submission to various scientific journals. Chapter Two reports data on the synthesis, spectroscopic and thermal characterization of selected synthetic hydrated uranyl phosphates, entitled "Spectroscopic and Thermal Study of Hydrated Uranyl Phosphates: Francoisite-(Nd) and Triuranyl Diphosphate Tetrahydrate". This study is being submitted to *American Mineralogist*. Chapter Three discusses the need for using a complementary approach involving both infrared spectroscopy and powder x-ray diffraction to effectively characterize hydrated uranyl phosphates. This work, entitled "Delineating Hydrated Uranyl Phosphates: Powder XRD and ATR-IR Studies", is being submitted to *Journal of Physics: Conference Series* as part of the proceedings of the Actinides 2009 conference. Chapter Four, entitled "The Hydrothermal Transformation of Chernikovite into Triuranyl Diphosphate Tetrahydrate (TDT)", reports the complete conversion of one hydrated phosphate into another due to hydrothermal

treatment, namely chernikovite to triuranyl diphosphate tetrahydrate (TDT). This contribution is being submitted to *American Mineralogist*. Chapter Five is a thermodynamic study, reporting data on the solubility of TDT at 23 and 50^{o}C. This work, entitled "Experimental solubility of triuranyl diphosphate tetrahydrate (TDT) at 23^{o}C and 50^{o}C", is being submitted to *Radiochimica Acta* as part of the proceedings of the Migration 2009 conference. Chapter Six is another thermodynamic study; however this one involves the use of differential scanning calorimetry (DSC) to obtain the enthalpy associated with discrete water populations in hydrated uranyl phosphates. This work, entitled "The effect of hydration on the enthalpy for U^{6+} solids: A thermal study", is being submitted to the *Journal of Solid State Chemistry* for publication. Chapter Seven reports data on the uptake of Nd onto hydroxylapatite entitled "Partitioning of Neodymium into Hydroxylapatite ($Ca_5(PO_4)_3OH$)". This work is being submitted to *Radiochimica Acta* as part of the proceedings of the Migration 2009 conference.

References

Abdelouas, A.; Lutze, W., and Nuttal, H.E. In *Uranium: Mineralogy, Geochemistry, and the Environment*; Burns, P.C., Finch, R., Eds. Reviews in Mineralogy 38; Mineralogical Society of America: Washington, DC, **1999,** 433-474.

Bell, L.C., Posner, A.M., Quirk, J.P. *Nature.* **1972**, 239, 515-517.

Boatner, L.A. In: Phosphates*: Geochemical, geobiological, and Materials Importance.* Kohn, M.J., Rakovan J., Hughes, J.M., Eds. *Reviews in Mineralogy, 48*, Mineralogical Society of America: Washington, DC. **2002**, 87-121.

Bray, T.H., Gorden, J.D., Albrecht-Schmitt, T.E. (2008) Synthesis and structure of $[C_6H_{14}N_2][(UO_2)_4(HPO_4)_2(PO_4)_2(H_2O)]\cdot H_2O$: An expanded open-framework amine-bearing uranyl phosphate. *J. Sol. State Chem.* **181**, 2199-2204.

Burns, P.C., Miller, M.L., Ewing, R.C. (1996) U^{6+} minerals and inorganic phases: A comparison and hierarchy of crystal structures. *Can. Mineral.* **34**. 845-880.

Burns, P.C. (1999) The crystal chemistry of uranium. In: Reviews in Mineralogy Vol. 38. Eds. Burns, P.C., Finch, R. Mineralogical Society of America. 23-86.

Burns, P.C. (2005) U^{6+} minerals and inorganic compounds: Insights into an expanded structural hierarchy of crystal structures. *Can. Mineral*. **43**, 1839-1894.

Bruno, J.; de Pablo, J.; Duro, L.; Figuerola, E. *Geochem. Cosmochim. Acta*, **1995**, *59(20)*, 4113-4123.

Cejka, J. (1999) Infrared spectroscopy and thermal analysis of uranyl minerals. In: Reviews in Mineralogy Vol. 38. Eds. Burns, P.C., Finch, R. Mineralogical Society of America. 521-622.

Choppin, G.R. *J. Less-Common Metals,* **1983,** 93, 323-330.

Choppin, G.R. *J. Less-Common Met.,* **1986,** 126, 307-313.

Choppin, G.R. *Mar. Chem.*, **1989,** 28, 19-26.

Elless, M.P., Lee, S.Y. (1998) Uranium solubility of carbonate-rich uranium-contaminated soils. *Water, Air, Soil Pollut*. **107**, 147-162.

Felmy, A.R., Xia, Y., Wang, Z. (2005) The solubility product of $NaUO_2PO_4\cdot xH_2O$ determined in phosphate and carbonate solutions. *Radiochim. Acta.* **93**, 401-408.

Finch, R.J., Murakami, T. In *Uranium: Mineralogy, Geochemistry, and the Environment*; Burns, P.C., Finch, R., Eds. Reviews in Mineralogy 38; Mineralogical Society of America: Washington, DC, **1999,** 91-181.

Frost, R.L., Weir, M. (2004a) Raman Spectroscopy of autunite minerals at liquid nitrogen temperature. *Spectrochim. Acta Part A.* **60**, 2399-2409.

Frost, R.L., Weir, M., Adebajo, M.O. (2004b) Thermal decomposition of metazeunerite – a high-resolution thermogravimetric and hot-stage Raman spectroscopic study. *Thermochim. Acta*. **419**, 119-129.

Frost, R.L., Cejka, J., Weir, M. (2006a) Raman spectroscopic study of uranyl oxyhydroxide hydrates: bequerelite, billietite, curite, shoepite, and vandendriesscheite. *J. Raman Spec.* **38**, 460-466.

Frost, R.L., Weir, M.L., Martens, W., Cejka, J. (2006b) The structure of phurcalite – A vibrational spectroscopic study. *Vib. Spec.* **41**, 205-212.

Fuller, C.C, Bargar, J.R., Davis, J.A., Piana, M.J. *Environ. Sci. Technol.* **2002,** *36*, 158-165.

Fuller, C.C, Bargar, J.R., Davis, J.A. *Environ. Sci. Technol.,* **2003,** *37*, 4642-4649.

Giammar, D.E. Xie, L., Pasteris, J.D. (2008) Immobilization of lead with nanocrystalline carbonated apatite present in fish bone. *Environ. Eng. Sci*. **25**, 725-736.

Gorman-Lewis, D.J., Mazeina, L., Fein, B., Szymanowski, J., Burns, P.C., Navrotzky, A. (2007) Thermodynamic properties of soddyite from solubility and calorimetry measurements. *J. Chem. Thermodyn*. **39**, 568-575.

Gorman-Lewis, D., Burns, P.C., Fein, J.B. Review of uranyl mineral solubility measurements. J. Chem. Thermodyn. **40** (2008) 335-352.

Hawthorne, F.C. (1992) The role of OH and H_2O in oxide and oxysalt minerals. *Zeit. Fur Kristall*. **201**, 183-206.

Hawthorne, F.C., Schindler, M. (2008) Understanding the weakly bonded constituents in oxysalt minerals. *Zeit. Fur Kristall*. **223**, 41-68.

Hughes, J.M., Rakovan, J. In: Phosphates*: Geochemical, geobiological, and Materials Importance.* Kohn, M.J., Rakovan J., Hughes, J.M., Eds. *Reviews in Mneralogy, 48,* Mineralogical Society of America: Washington, DC. **2002**, 1-13.

Huminicki, D.M.C., Hawthorne, F.C. In: Phosphates*: Geochemical, geobiological, and Materials Importance.* Kohn, M.J., Rakovan J., Hughes, J.M., Eds. *Reviews in Mneralogy, 48,* Mineralogical Society of America: Washington, DC. **2002**, 123-255.

Ilton, E.S., Liu, C.X., Yantasee, W., Wang, Z.M., Moore, D.A., Felmy, A.R., Zachara, J.M. (2006) The dissolution of synthetic Na-boltwoodite in sodium carbonate solutions. *Geochim. Cosmochim. Acta.* **70**, 4836-4849.

Jeanjean, J., Rouchaud, J.C., Tran, L., Federoff, M. *J. Radioanal. Nucl. Chem., Letters*, **1995**, 6, 529-539.

Jerden, J.L., Sinha, A.K., Zelanzny, L. *Chem. Geol*., **2003**, 199, 129-157.

Khosrawan-Sazedj, F. (1982) On the space group of threadgoldite. *Tschermaks Mineral. Petrogr. Mitt*. **30**, 111-115.

Knox, A.S., Kaplan, D.I., Adriano, D.C., Hinotn, T.G., Wilson, M.D. *J. Environ. Qual.*, **2003**, 32, 515-525.

Knudsen, A.C., Gunter, M.E. In: Phosphates*: Geochemical, geobiological, and Materials Importance.* Kohn, M.J., Rakovan J., Hughes, J.M., Eds. *Reviews in Mneralogy, 48*, Mineralogical Society of America: Washington, DC. **2002**, 363-391.

Locock, A.J., Burns, P.C. (2002) The crystal structure of triuranyl diphosphate tetrahydrate. *J. Sol. State Chem*. **163**, 275-280.

Locock, A.J., Burns, P.C. (2003a) Crystal structures and synthesis of the copper-dominant members of the autunite and meta-autunite groups: torbenite, zeunerite, metatorbernite and metazeunerite. *Can. Mineral*. **41**, 489-502.

Locock, A.J., Burns, P.C. (2003b) The crystal structure of synthetic autunite. *Amer. Mineral.* **88**, 240-244.

Locock, A.J., Burns, P.C, Duke, M.J.M., Flynn, T.M. (2004) Monovalent cations in structures of the meta-autunite group. *Can. Mineral.* **42**, 973-996.

Markovic., M., Pavkovic, N. (1983) Solubility and equilibrium constants of uranyl(2+) in phosphate solutions. *Inorg. Chem.* 22, 978-982.

Meinrath, G., Kimura, T. (1993) Behavior of uranium (VI) solids under conditions of natural aquatic systems. *Inorg. Chem. Acta*. **204**, 79-85.

Nitsche, H. *Basic research for assessment of geologic nuclear waste repositories: What solubility and speciation studies of transuranium elements can tell us.* Paper presented at the Intl. Symp. on Sci. Basis for Nuclear Waste Management, Boston, MA Conf. Proceedings, **1990.**

Nguyen, S.N., Silva, R.J., Weed, H.C., Andrews, J.E. (1992) Standard Gibbs free energies of formation at the temperature 303.15 K of four uranyl silicates: soddyite, uranophane, sodium boltwoodite, and sodium weeksite. *J. Chem. Thermodyn*. **24**, 359-376.

Ohnuki, T., Kozai, N., Samadfam, M., Yasuda, R., Yamamoto, S., Narumi, K., Naramoto, H., Murakami, T. *Chem. Geol.,* **2004,** 211, 1-14.

Pham-Thi, M., Colomban, Ph. (1985) Morphological, X-ray and vibrational study of various uranyl phosphate hydrates. *J. Less-Common Met*. **108**, 189-216.

Piccoli, P.M, Candela, P.A. In: Phosphates*: Geochemical, geobiological, and Materials Importance.* Kohn, M.J., Rakovan J., Hughes, J.M., Eds. *Reviews in Mineralogy, 48*, Mineralogical Society of America: Washington, DC. **2002**, 255-293.

Rai, B.D., Felmy, A.R., Hess, N.J., LeGore, V.L., McCready, D.E. (2002) Thermodynamics of the U(VI)-Ca^{2+}-Cl^{-}-OH^{-}-H_2O system: Solubility product of becquerelite. *Radiochim. Acta* **90**, 495-503.

Rai, B.D., Xia, Y., Rao, L., Hess, N.J., Felmy, A.R., Moore, D.A., McCready, D.E. (2005) Solubility of $(UO_2)_3(PO_4)_2 \cdot 4H_2O$ in H^+-Na^+-OH^-- H_2PO_4 -PO_4^{3-} - H_2O and its comparison to the analogous PuO_2^{2+} system. *J. Sol. Chem.* **34**, 469-498.

Schindler, M., Hawthorne, F.C. (2008) The stereochemistry and chemical composition of interstitial complexes in uranyl-oxysalt minerals. *Can. Mineral*. **46**, 467-501.

Spear, F.S., Pyle, J.M. In: Phosphates*: Geochemical, geobiological, and Materials Importance.* Kohn, M.J., Rakovan J., Hughes, J.M., Eds. *Reviews in Mineralogy, 48*, Mineralogical Society of America: Washington, DC. **2002**, 337-363.

Thakur, P., Moore, R.C., Choppin, G.R. *Radiochim. Acta*, **2005,** 93, 385-391.

Van Haverbeke, Vochten, R., Van Springel, K. (1996) Solubility and spectrochemical characteristics of synthetic chernikovite and meta-ankoleite. *Mineral. Mag.* **60**, 759-766.

Vesely, V., Pekarek, V., Abbrent, M. (1965) A study of uranyl phosphates III Solubility products of uranyl hydrogen phosphate, uranyl orthophosphate and some alkali uranyl phosphates. *J. Inorg. Nucl. Chem*. **27**, 1159-1166.

Vochten, R., De Grave, E., Pelsmaekers, J. (1984) Mineralogical study of bassetite in relation to its oxidation. *Amer. Mineral.* **69**, 967-978.

Vochten, R. (1990) Transformation of chernikovite and sodium autunite into lehnerite. *Amer. Mineral*. **75**, 221-225.

Wellman, D.M., McNamara, B.K., Burton, S.D., Geiszler, K.N., Baum, S.R., Butler, B.C. *In Remediation of Contaminated Sediments.* Olfenbuttel, R.F., White, P.J., Eds. Proceedings of the Third International Conference on Remediation of Contaminated Sediments. New Orleans, Lousiana. Battelle Press, Columbus, OH, **2006.**

Xu, Y., Schwartz, F.W. *Environ. Sci. Technol.,* **1994**, 28, 1472-1480.

Yu, Y., Albrecht-Schmitt, T.E. (2008) Incorporation of tetrahedral Co(II) into a mixed-metal uranyl phosphate framework: Synthesis and structure of $K_2[UO_2Co(PO_4)_2] \cdot H_2O$. *Sol. State Sci.* **10**, 821-824.

Yu, Y., Zhan, W., Albrecht-Schmitt, T.E. (2008) $[H_2bipy]_2[(UO_2)_6Zn_2(PO_3OH)_4(PO_4)_4]\cdot H_2O$: An open framework uranyl zinc phosphate templated by diprotonated 4,4'-bipyridyl. *Inorg. Chem*. **47**, 9050-9054.

CHAPTER TWO

Spectroscopic and Thermal Study of Hydrated Uranyl Phosphates: Francoisite-(Nd) and Triuranyl Diphosphate Tetrahydrate

Christopher R. Armstrong,[a,] Kenneth L. Nash,[a] Peter R. Griffiths,[b] Sue B. Clark,[a,*]

[a]*Department of Chemistry, Washington State University, Pullman, WA 99164, U.S.A.*
[b]*Department of Chemistry, University of Idaho, Moscow, ID 83844, U.S.A.*

Abstract

In this report we present data on the bulk and nanoscale characterization of triuranyl diphosphate tetrahydrate (TDT) and the novel francoisite-(Nd) (empirical formulas below). Experimental studies including chemical digestion, thermogravimetric analysis (TGA), differential scanning calorimetry (DSC), attenuated total reflection infrared spectrometry (ATR-IR), Raman spectroscopy and powder x-ray diffraction (PXRD) were conducted. The stoichiometry and related degree of hydration for TDT and francoisite were determined to be $Nd[(UO_2)_{3.4}O(OH)(PO_4)_{2.0}]\bullet 5.2H_2O$ and $(UO_2)_{3.1}(PO_4)_{2.0}\bullet 3.9H_2O$ respectively. Both phases are hygroscopic, readsorbing 40 % and 86 % of initial water content respectively upon reheating to 500^oC; however, no structural changes were observed. The local bonding environments of uranyl and water were investigated with ATR-IR and Raman spectroscopy. The uranyl-oxygen (uranyl group) and O-O bond (hydrogen bonded oxygen and water) lengths were calculated from the vibrational frequencies of the antisymmetric and symmetric modes of uranyl and the stretching modes of water. The calculated values obtained for the materials synthesized in this study agree well with literature values for the synthetic TDT and natural francoisite-(Nd). The IR spectra of protiated and deuterated francoisite-(Nd) confirmed a coordinated hydroxyl group bridging vicinal uranyl groups in the francoisite-(Nd) structural unit. These studies provide the basis for further thermodynamic (solubility, sorption) and geochemical modeling investigations of these and other uranyl phosphate compounds.

Key words: francoisite-(Nd), triuranyl diphosphate tetrahydrate, uranyl, spent nuclear fuel

1. INTRODUCTION

In an effort to better understand the mobility of *f*-elements in natural systems, fundamental investigations into the chemistry of these metal cations at the solid-solution interface have received considerable attention. Uranium primarily occurs in the hexavalent state as uranyl (UO_2^{2+}) in oxidizing environments. Uranyl compounds have been introduced into the biosphere primarily as the result of corrosion of spent nuclear fuel (SNF) (Kim et al., 1999), leakage of underground storage tanks (Womack and Larkin, 1971) and the extraction and purification of uranium ores for weapons production (Buck et al., 1996). Of these uranyl solids, the oxides, silicates and phosphates are the most stable and thus are expected to comprise the most important sinks for uranium in oxidizing waste disposal environments. Consequently, solubility studies of the more common naturally occurring uranyl-bearing minerals such as uranyl phosphates (Vesely et al., 1965; Markovic et al., 1983; Felmy et al., 2005; Rai et al., 2005) silicates (Nguyen, et al., 1992; Ilton et al., 2006; Gorman-Lewis et al., 2007), oxy-hydroxides (Rai et al., 2002; Giammar and Hering, 2002) and carbonates (Meinrath et al., 1993; Elless and Lee, 1998) have been conducted. Phosphate solids are highly stable in aqueous systems under ambient conditions throughout a wide pH range. Showing a high potential for reducing the mobility of aqueous metals including actinide cations, phosphates may serve as effective remediation amendments both as solids, in various forms of synthetic (Wright and Conca, 2002) and natural apatite, e.g., fish bone (Giammar et al., 2008), and in the solution phase, e.g., polyphosphates (Wellman et al., 2006). To predict the environmental fate of mixed actinide phosphates over a geological timescale, it is necessary to elucidate the structure and stability of solid phases that result from these phosphate-induced metal stabilization strategies.

Triuranyl diphosphate tetrahydrate (TDT), ($[(UO_2)_3(PO_4)_2]\cdot 4H_2O$, and francoisite-(Nd), ($Nd[(UO_2)_3O(OH)(PO_4)_2]\cdot 5H_2O$, were selected for this study for two reasons. First, both of

these materials are sparingly soluble and are thus expected to limit the concentration of aqueous uranyl ion. Additionally, francoisite-(Nd) contains both an actinide (U) and a lanthanide (Nd) atom. The trivalent Nd ion is a reasonable analog for Am and Cm ions because of its similarity in ionic radius and oxidation state. Thus francoisite-(Nd) serves as a good model of a mixed actinide solid that may form as the result of anthropogenic actinide infiltration, particularly in locations where phosphate amendments (apatite, polyphosphates) may be used in remediation scenarios.

In this contribution, we provide characterization data of the uranyl phosphates, TDT and the novel francoisite-(Nd) with an emphasis on understanding the role of water in these materials. The goal of this study is to (i) characterize select hydrated uranyl phosphates, francoisite-(Nd) and triuranyl diphosphate tetrahydrate (TDT) and, (ii) investigate the role of water in these materials. The delineation of distinct water populations in these uranyl phosphates can assist us in predicting the stability of these phases. For example, the assignment of distinct standard state free energies of formation of water, reflecting different water occupancies, yields a more accurate estimation of the thermodynamic properties of a broad range of uranyl solids for which experimental thermodynamic data are highly disparate or not presently available.

In this report, we endeavor to delineate water such that specific populations are reflected in the empirical formula of the material following the Hawthorne method, as described in Chapter One of this thesis. As such, with the exception of physisorbed water, all other water populations are included in the empirical formula. For example, take the mineral metavoltine (Hawthorne and Schindler, 2008), $K_2Na_6Fe(H_2O)_6[Fe_3O(SO_4)_6(H_2O)_3]_2(H_2O)_6$. Here the formula clearly delineates stoichiometric water. The first water group (from left to right) represents interstitial-coordinated, the second water group is indicative of structural water and the last water group is attributed to weakly bound (occluded) interstitial water.

1.1. Vibrational spectroscopic studies

Until quite recently, vibrational spectroscopic studies of uranyl phosphates, particularly Raman spectroscopy, have received little attention. Cejka (1999) presented a thorough overview of all the available thermal and infrared (IR) spectroscopic studies of U-bearing minerals. Pham-Thi and Colomban (1985) conducted an exhaustive study investigating a trio of uranyl phosphates. These workers provided both IR and Raman data on these materials. The Vochten group reported a series of U-mineral characterization studies of which IR data is only a part (Vochten et al., 1984; Vochten, 1990; Van Haverbeke et al., 1996). The Frost group has conducted numerous Raman spectroscopic investigations on uranyl-bearing minerals (Frost and Weir, 2004a; Frost et al., 2004b; Frost et al., 2006a; Frost et al., 2006b).

2. EXPERIMENTAL MATERIALS AND METHODS

Chemicals

All chemicals are reagent grade or higher. Deionized (18 MΩ) and boiled water was used in preparations of all solutions. Standards used for ICP-OES analyses were 99.9% purity.

Synthesis

The pH was measured with a ThermoElectron Corp. Orion 4 Star pH meter equipped with a Ross combination pH electrode (Orion Model 8102). Prior to each use, the pH electrode was calibrated with NIST standards. For hydrothermal reactions, 23- and 45-mL Teflon® liners were placed inside stainless steel Parr acid digestion bombs.

Francoisite-(Nd) synthesis

Francoisite-(Nd) crystals were synthesized by two methods. In the first, stoichiometric volumes of 0.05M $Nd(NO_3)•6H_2O$, H_3PO_4 and $UO_2(NO_3)•6H_2O$ were mixed in a jacketed reaction vessel at 40 ± 0.1°C. The initial pH was low (ca. 1.8) and a pale yellow precipitate was observed immediately. The pH was adjusted to 5 and maintained with a small amount of 1 M NaOH. As the pH was increased to ca. 5, a color change to bright yellow was observed in the solid. Once adjusted, the pH remained at ca. 5 throughout the synthesis. The second method involved the use of Nd and uranyl acetate salts instead of the nitrates (with the same concentrations and stoichiometric proportions as the nitrate procedure above). Note: All of the experiments conducted in this study involved the francoisite-(Nd) synthesized by this acetate method. The initial pH was ca. 4.5 and a bright yellow precipitate was observed immediately. The pH was raised and maintained at ca. 5 with 1 M NaOH. The suspension was stirred overnight under N_2 gas at 40ºC, and was subsequently allowed to settle and age overnight under N_2 at 40ºC. 1-mL samples of the mother liquor were taken in duplicate and acidified with concentrated HNO_3 and diluted with ultrapure deionized water (DIW) and stored for further analysis. The solid was extracted and vacuum-filtered through 0.45-µm Millipore membranes and rinsed three times with boiling DIW. The resulting filtrate was covered and stored in the dark to dry until constant weight was obtained. The solid was then ground with an agate mortar and pestle and sieved (100 mesh) to an approximate 150-µm particle size. Duplicate powder samples of approximately 10 mg were digested in concentrated HNO_3 and diluted to 100 mL in a volumetric flask with DIW. Dissolved metal determination from both the solid and mother liquor was carried out on a Perkin-Elmer Optima 3200 axial torch inductively-coupled optical emission spectrometer (ICP-OES). See Table 1 for detection limit details. For all samples, three replicate intensities were recorded from which the average and standard deviation was calculated.

Table 1. Analytes and corresponding wavelengths and detection limits in this study.

Analyte	Line (nm)	Detection limit (mg/L)	1σ
Na	330.237	2.00	0.09
Nd	401.225	0.05	0.01
P	213.617	0.08	0.03
U	367.007	0.30	0.02

Triuranyl diphosphate tetrahydrate (TDT) synthesis

Microcrystalline TDT was synthesized according to the modified method of Rai et al. (2005). Stoichiometric volumes of 0.7M H_3PO_4 and 0.05M $UO_2(NO_3)_2 \cdot 6H_2O$ were mixed in a jacketed reaction vessel under N_2 atmosphere at 40^{o}C (± 0.1). The suspension was stirred overnight at 40^{o}C and subsequently allowed to settle. Twice the supernatant was decanted and replaced with degassed DIW at 40^{o}C. The suspension was vacuum filtered through 0.45-µm Millipore membranes, rinsed three times with boiling DIW and dried overnight at 30^{o}C. Solids were crushed with a mortar and pestle and sieved (100 mesh) to an approximate 150 µm particle size. Both the solid and the mother liquor were prepared for elemental analysis in the same manner as francoisite-(Nd) mentioned above.

2.1 D_2O studies

Deuterated francoisite-(Nd) and TDT were synthesized in the same manner as described above. In all cases, 99% D_2O (Cambridge Isotope Laboratories) was used to prepare the stock solutions for synthesis. These solutions were sealed and stored in a desiccator. In addition, the deuterated samples were dried under an Ar atmosphere and promptly sealed to avoid H_2O/ D_2O exchange.

2.2 Powder x-ray diffraction (PXRD)

PXRD was performed on fine grained samples (~ 150 μm) of francoisite-(Nd) and TDT at room temperature using a Siemens Kristalloflex D500 diffractometer with the following parameters: Copper source (Kα; 1.54018 Å); 35 keV, 30 mA, Kβ filter: Ni; scintillation counter detector; Continuous mode: 0.02d/min; 2θ range: 5-60. The diffractograms were produced using MDI Data Scan 4 and Jade 8 software packages. No background corrections or smoothing was applied.

2.3 Thermal Analyses (TGA and DSC)

To assess the degree of hydration in the synthetic francoisite-(Nd) and triuranyl diphosphate samples, thermogravimetric analysis (TGA) and differential scanning calorimetry (DSC) were conducted using a Perkin-Elmer TGA-7 and Perkin-Elmer DSC-7 instruments, respectively. For TGA, the powders were analyzed inside a platinum pan. The TGA was calibrated with a 10 mg standard weight furnished by Perkin-Elmer. For DSC, the samples were crimped inside aluminum pans. The DSC was calibrated with pure zinc and indium metal standards. For both TGA and DSC, the scan rate was 5^{o}C/min and the experimental temperature ranged from 25^{o}C to 500^{o}C. Approximately 10 mg of solid was used in all of these experiments, which were completed in duplicate.

2.4 ATR-IR Spectrometry

For the studies presented herein, attenuated total reflection infrared (ATR-IR) spectra were measured. ATR has several advantages over conventional mid-infrared transmission techniques. Because the depth of penetration, d_p, is only about a quarter of the wavelength, a very thin sample (<10 μm) is not necessary. Ion exchange between diluents such as KBr and the sample can result in band broadening and lower intensity (Cejka, 1999; Griffiths and de Haseth, 2007). In ATR, solid samples do not need to be diluted (e.g., with KBr) and can be analyzed in their neat state thus obviating any ion exchange issues. All that is required is sufficient contact between the sample and the internal reflection element (IRE). Because samples do not have to be ground very finely, as required for mineral oil mulls or KBr disks, changes in spectral characteristics due to morphological changes in the sample on grinding are not usually observed with ATR.

Measurements were made on solids in this study using a Nicolet 6700 FT-IR spectrometer with an ATR accessory equipped with a ThermoElectron Smart Nexus Orbit single-reflection diamond IRE. Spectra were measured between 4000 and 400 cm^{-1} at 8 cm^{-1} resolution. A total of 200 scans were averaged for each sample and background. The system was purged with desiccated N_2 at 30 psi. As noted above, the solid samples were ground with an agate mortar and pestle and sieved to an approximate 150 μm particle size. To account for the wavelength dependence of d_p, an ATR correction built into the OMNIC software was applied.

2.5 Raman Spectrometry

Experiments were conducted on ~ 150 μm particle size powders of francoisite-(Nd) and TDT at room temperature using a Delta Nu Advantage 633 Raman spectrometer with the following

parameters. Laser: HeNe (632.8 nm); CCD detector; integration time 30s; spectral range: 1200 – 400 cm^{-1}. All spectra represent the average of ten scans.

3. RESULTS

3.1. Elemental Analysis

3.1a. Francoisite-(Nd)

Average concentrations of the duplicate chemical digestion samples are shown in Table 2. These dissolved elemental concentrations were used to determine the following empirical formula.

$$\mathbf{Nd[(UO_2)_{3.38}O(OH)(PO_4)_2]\bullet 5.16H_2O}$$

This may be compared to the empirical formula of natural francoisite (Piret et al., 1988):

$$\mathbf{0.94Nd[(UO_2)_{3.15}\ O(OH)(PO_4)_{1.92}]\bullet xH_2O}$$

The elemental composition reported herein is in reasonable agreement with the natural francoisite-(Nd) sample. However, residual sodium was detected in the synthetic francoisite-(Nd). In addition the natural sample had a host of trace impurities that were detected in the elemental analysis (Piret et al., 1988). Thus, small compositional differences between the synthetic and natural samples are expected.

3.1b. TDT

The chemical digestion data of the average concentration of duplicates shown in Table 2 were used to determine the following empirical formula:

$$\mathbf{(UO_2)_{3.13}(PO_4)_2\bullet 3.91H_2O}$$

Table 2. Chemical digestion data for francoisite-(Nd) (top) and TDT (bottom).

Component	Concentration (M)	1 σ	Molar Ratio
UO_2^{2+}	$2.44 \cdot 10^{-4}$	$1.86 \cdot 10^{-5}$	3.38
PO_4^{3-}	$1.57 \cdot 10^{-4}$	$3.77 \cdot 10^{-5}$	2.17
Nd^{3+}	$7.22 \cdot 10^{-5}$	$2.92 \cdot 10^{-6}$	1.00
H_2O	$6.03 \cdot 10^{-4}$	$4.21 \cdot 10^{-4}$	8.35
Component	**Concentration (M)**	**1 σ**	**Molar Ratio**
UO_2^{2+}	$6.68 \cdot 10^{-4}$	$3.06 \cdot 10^{-6}$	3.13
PO_4^{3-}	$4.27 \cdot 10^{-4}$	$1.40 \cdot 10^{-5}$	2.00
H_2O	$2.05 \cdot 10^{-3}$	$1.99 \cdot 10^{-4}$	4.81

The stoichiometry obtained herein for TDT is in agreement with published work (Pham-Thi and Columban, 1985; Locock and Burns, 2003; Rai et al., 2005).

Note: The degree of hydration for both francoisite-(Nd) and TDT was obtained by calculating the water loss upon heating the powders via thermogravimetric analysis (see next section).

3.2. Thermal Analysis

3.2a. Francoisite-(Nd)

The gradual weight loss of the powdered francoisite-(Nd) as a function of temperature can be seen in Fig. 2A and the first derivative of this profile is shown in Fig. 2B. Interestingly, a distinct color change was observed upon heating to 500°C, from a pale yellow to a burnt orange.

A plateau region is observed at ca. 495-500^{o}C suggesting complete water expulsion at high temperature.

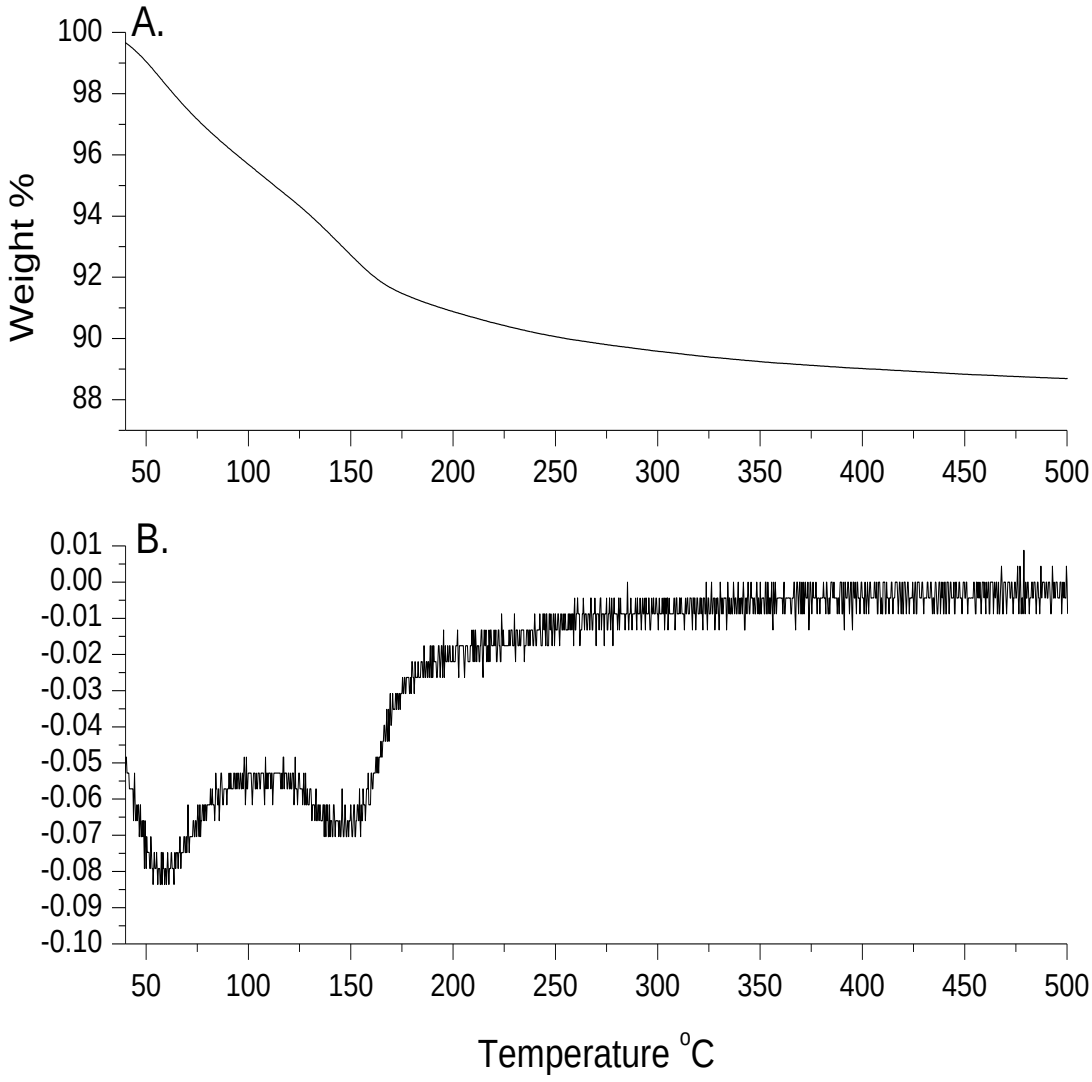

Fig. 2. Panel A. TGA of francoisite-(Nd). The TGA temperature profile represents the average of duplicate runs. All runs were conducted at 5 ^{o}C/min scan rate. Panel B. 1st derivative of TGA profile.

The broad curves in the DSC temperature profile are indicative of local maxima suggesting separate endothermic events (Fig. EA-1; Supplementary Data). Although the TGA derivative profile appears to exhibit the most conspicuous evidence, the complementary data accrued from both the TGA and DSC yield two well-defined water loss events, along with a more diffuse water release event at high temperature (above 245^{o}C) . These events, together with approximate temperature ranges, are shown in Table 3. Below 100ºC and centered at ca. 60ºC , roughly 3.2 moles of water are released and are attributed to physisorption. From 100ºC to 500ºC, a broad dehydration event is observed centered at ca. 150ºC resulting in the release of approximately 5.2 moles of water. These waters are likely occluded in the interstitial region. From these data, a maximum of 8.36 moles of water per formula unit of francoisite-(Nd) were calculated. The waters associated with the solid below ca. 100ºC are attributed to physisorption and are thus not counted as stoichiometric water (Rai et al., 2005). Hence, the formula unit according to the method of Hawthorne (1992) based upon elemental and thermal analyses is: **$Nd[(UO_2)_3O(OH)(PO_4)_2]\cdot 5.2H_2O$.**

3.2b. TDT

The dehydration of TDT crystals as a function of temperature was investigated in a similar manner to that of francoisite-(Nd). Weight loss events can be evaluated by examining the TGA temperature profiles depicted in Fig. 3 and DSC (Fig. EA-2; Supplementary Data). Three dehydration events evidenced by slope changes in the TGA thermogram and the corresponding derivative plot (Figs. 3A and 3B, respectively) are clearly visible. A minor event is observed between 25 and 100ºC with a peak at ca. 60ºC.

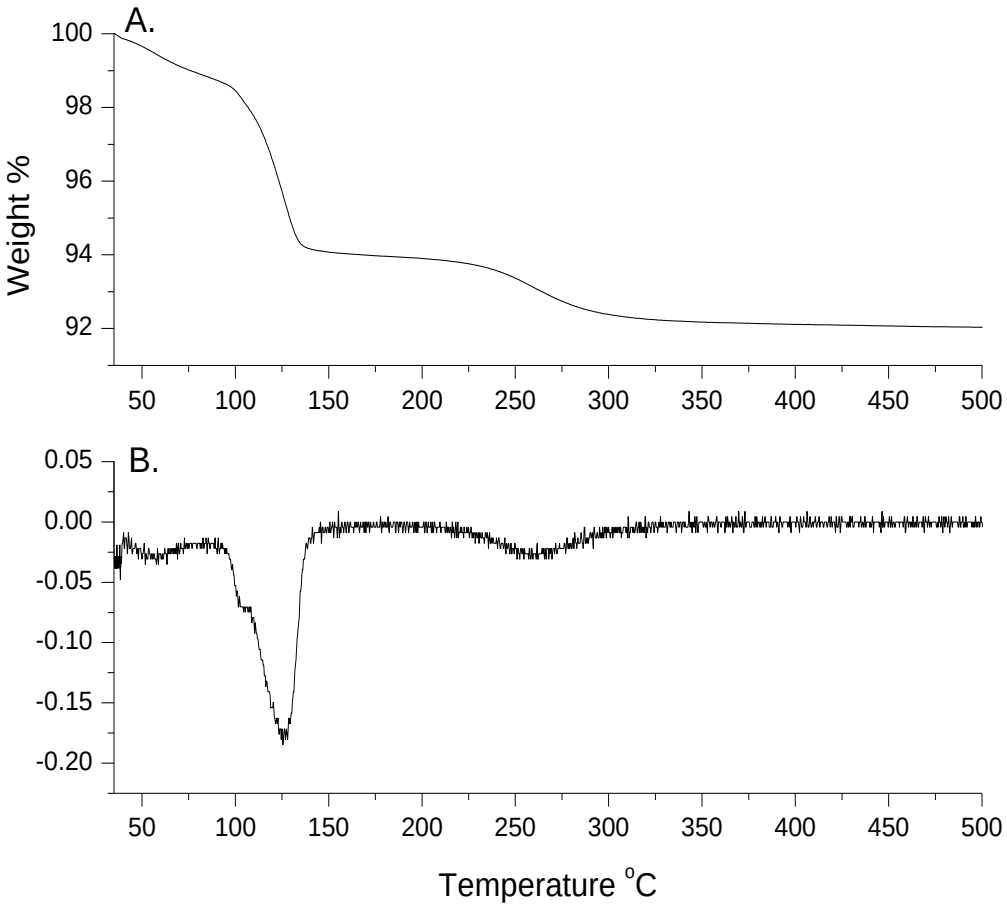

Fig. 3. Panel A. TGA plot of TDT representing the average of duplicate runs conducted at a scan rate of 5 ^{o}C/min. Panel B. 1st derivative of profile shown in Panel A.

The major water loss event is centered at ca. 125ºC and a weak feature can be seen at ca. 260ºC. These events are also evidenced in the characteristic endothermic peaks in the DSC curve at approximately corresponding temperatures, although the endothermic events appear to be shifted to a higher temperature (Fig. EA-2; Supplemental Data). This may be due to the fact that the TGA samples are ran uncovered on the platinum pan whereas the DSC samples are crimped inside aluminum pans. Thus in the case of the DSC, a slightly higher temperature may be

required to expel water from the surface of the solid. A plateau region past ca. 400ºC suggests that all the waters have been released by this point. A maximum of 4.81 moles of water per formula unit of TDT were calculated (Table 3).

Table 3. Approximate francoisite-(Nd) (top) and TDT (bottom) dehydration events as a function of temperature from TGA analyses.

Temperature Range (°C)	**H_2O Lost (mol)**	**1σ**
25-100	3.186	0.020
100-245	4.092	0.039
245-500	1.066	0.058
Total H_2O loss	**8.355**	0.073
Stoichiometric water (mol)	**5.169**	0.076
Temperature Range (°C)	**H_2O Lost (mol)**	**1σ**
25-100	0.905	0.002
100-135	2.602	0.003
135-500	1.304	0.003
Total H_2O loss	**4.811**	0.005
Stoichiometric water (mol)	**3.906**	0.006

From these findings, the following local bonding environments of water are inferred. From room temperature to ca. 100ºC, 0.9 moles of water are lost; these are attributed to physisorbed (non-stoichiometric) water. Approximately 2.6 moles of water are released between

100ºC and 135ºC and are attributed to occluded interstitial water. From ca. 135ºC to 500ºC, roughly 1.3 moles of water are released and these water molecules are attributed to interstitial (coordinated) water. Thus the formula unit according to the method of Hawthorne (1999) based upon elemental and thermal analyses requires that the interstitial uranyl and water groups be delineated and, accounting for charge balance, becomes: $\mathbf{UO_2(H_2O)_{1.3}[(UO_2)_5(PO_4)_4]\cdot 2.6H_2O}$

These results are in good agreement with Rai et al. (2005) who reported four moles of water lost in TGA and DSC experiments conducted under similar conditions. However, as mentioned previously, these workers included the physisorbed water in the unit formula of TDT.

3.3 Powder x-ray diffraction (PXRD)

3.3a Francoisite-(Nd) and TDT

The diffractograms of PXRD analyses of francoisite-(Nd) and TDT are shown in Fig. 4. The most prominent francoisite-(Nd) reflection occurs at $2\theta = 11.34^{o}$ at a d-spacing of 7.8 Å (d-spacing value not shown). This is the same 2θ location and d-spacing as the most intense reflection in the natural francoisite-(Nd) sample reported by Piret et al., 1988 (PDF card: 42-1314). In general, very good agreement was observed between the synthetic francoisite-(Nd) diffractogram from this study and that of the natural sample.

The most prominent band in the TDT diffractogram appears at $2\theta = 21^{o}$ and a d-spacing of 4.2 Å (d-spacing value not shown). The powder diffraction data were compared to the International Centre for Diffraction Data (ICDD) powder diffraction card 37-0369 and very good agreement was observed. However it has been shown that the positions of the XRD reflections

vary slightly in TDT samples, in some cases shifting to higher d-spacing distances as a function of hydration (Pham-Thi and Columban, 1985; Thomas et al., 2001; Rai et al., 2005).

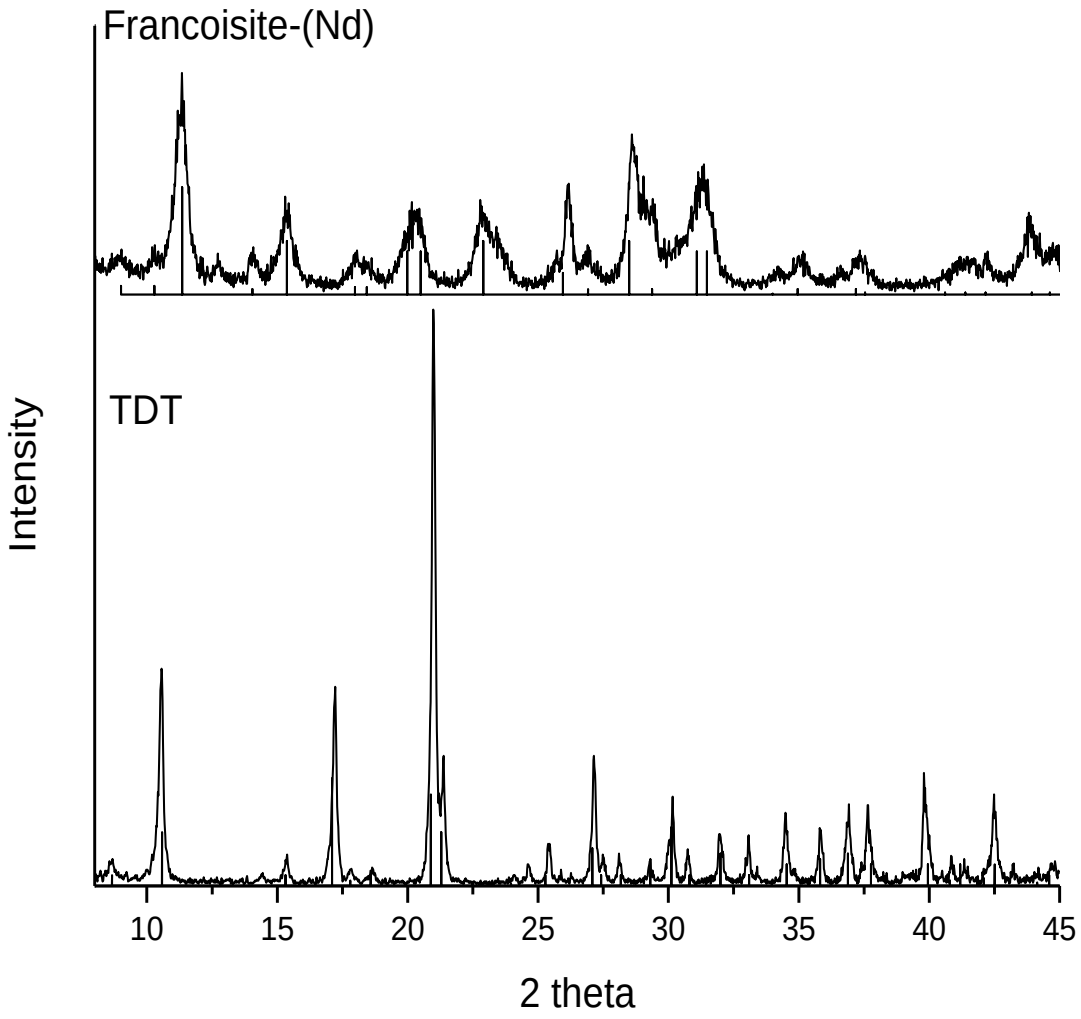

Fig. 4. Powder XRD diffractograms of francoisite-(Nd) (top) and TDT (bottom), together with the corresponding powder diffraction files (PDF), 42-1314 and 37-0369 respectively.

A qualitative comparison of the XRD patterns of francoisite-(Nd) and TDT clearly shows sharper peaks with higher intensity in the TDT diffractogram. The TDT powder is likely more crystalline; and the broader peaks observed in the francoisite-(Nd) sample may be attributed to an amorphous contribution.

3.4 ATR-IR and Raman Spectroscopy

3.4a Water elucidation with IR spectroscopy

The presence of water observed in TGA and DSC analyses is confirmed by the IR spectra of both francoisite-(Nd) and TDT. The broad OH stretching (ca. 3000 -3600 cm^{-}) and bending (ca. 1600-1640 cm^{-1}) modes are very prominent features in both spectra (Figs. 5 and 6; Tables 4 and 5). The OH stretching and bending bands in the spectrum of francoisite-(Nd) are quite similar to those of bulk water, suggesting that the water molecules are not in a defined position in the crystal lattice. These features may also suggest the presence of physisorbed water. The gradual decrease in the francoisite-(Nd) TGA profile (Fig. 2) also supports this hypothesis. The bands above 3000 cm^{-1} are the unresolved symmetric (ν_1) and antisymmetric (ν_3) OH stretching modes. Their width is largely a result of the extent of hydrogen bonding in the system (Schiffer et al., 1976). Bands in the OH stretching region are further broadened by the first overtone of the water bending mode overlapping the symmetric stretching mode and possibly being enhanced by Fermi resonance (Libowitzky and Beran, 2006). The spectrum of TDT in these regions is quite different from that of francoisite-(Nd). In addition to a broad band at 3330 cm^{-1}, the TDT spectrum features a very sharp band with relatively high intensity that is clearly visible at 3540 cm^{-1} and a weaker, but still narrow, band at 3625 cm^{-1}. The H-O-H bending mode is also sharper, at lower frequency and split into a doublet.

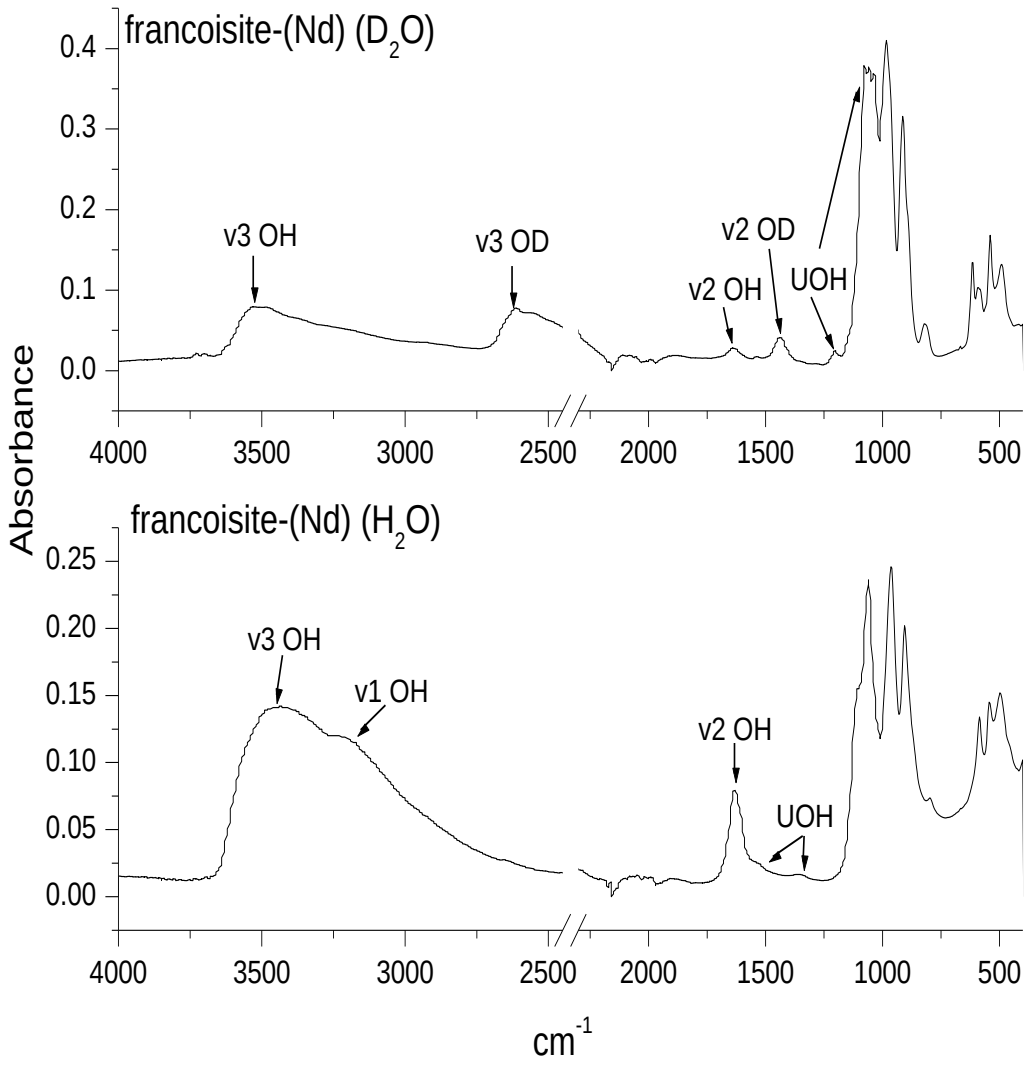

Fig. 5. ATR-IR spectrum of francoisite-(Nd) in the mid-infrared spectrum. Top panel: deuterated sample; bottom panel: protiated sample. Additional band assignments for the protiated spectrum can be seen in Table 4. No spectral features were observed in the region between ca. 2500 cm^{-1} and 2000 cm^{-1}; therefore part of this region was omitted for clarity.

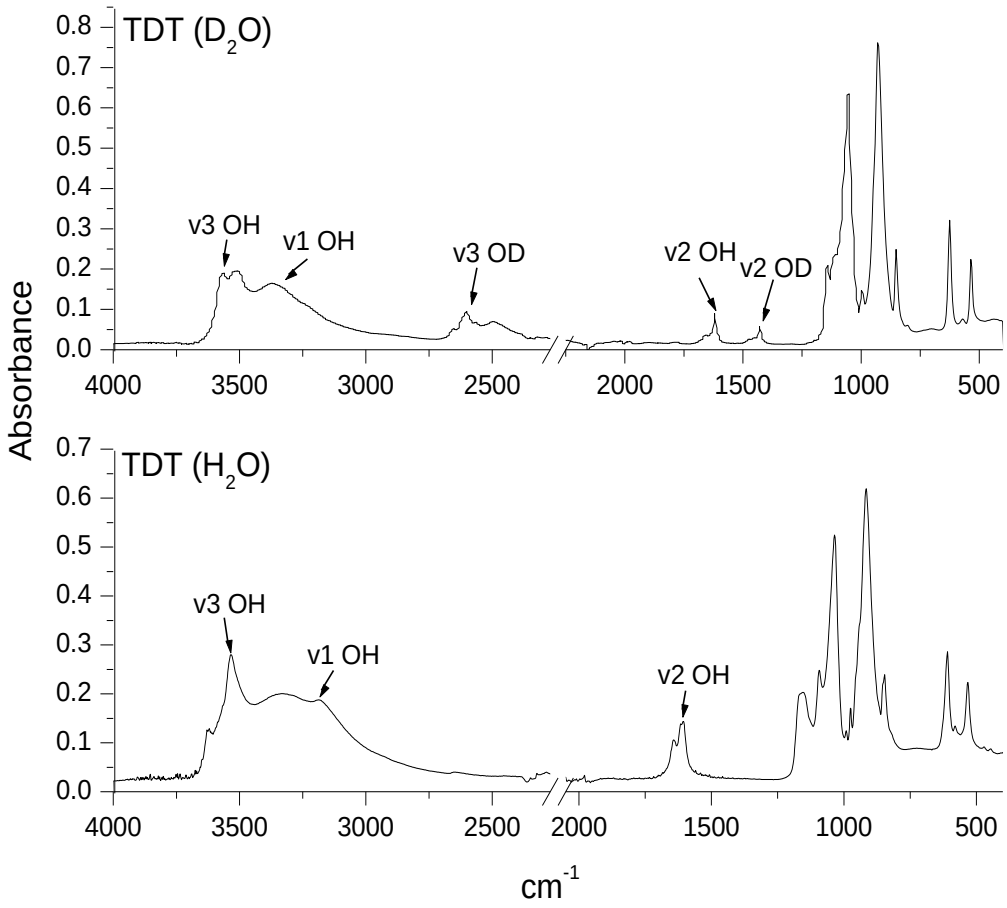

Fig. 6. ATR-IR spectrum of TDT in the mid-infrared spectrum. Deuterated sample: top panel; Protiated sample: bottom panel. Tentative band assignments for full spectrum of the protiated TDT are displayed in Table 5. No spectral features were observed in the region between ca. 2500 cm^{-1} and 2000 cm^{-1}; therefore part of this region was omitted for clarity.

Table 4. IR band assignments for francoisite-(Nd).

Wavenumber (cm^{-1})	**Group**	**Vibrational Mode**
493	PO_4^{3-}	Degenerate bend; ν4
542	PO_4^{3-}	Degenerate bend; ν4
585	PO_4^{3-}	Degenerate bend; ν4
798	UOH	In-plane bend; δ or out-of-plane bend; γ
905	UO_2^{2+}	Antisymmetric stretch; ν3
960	PO_4^{3-}	Antisymmetric stretch; ν3
1060	PO_4^{3-}	Antisymmetric stretch; ν3
1360	UOH	In-plane bend; δ
1530	UOH	In-plane bend; δ
1630	H_2O	Bending; ν2
3205	OH	Symmetric stretching; ν1
3430	OH	Antisymmetric stretching; ν3

Table 5. IR band assignments for TDT.

Wavenumber (cm^{-1})	Group	Vibrational Mode
531	PO_4^{3-}	Degenerate bend; ν4
611	PO_4^{3-}	Degenerate bend; ν4
847	UO_2^{2+}	Antisymmetric stretch; ν3
917	UO_2^{2+}	Antisymmetric stretch; ν3
1034	PO_4^{3-}	Antisymmetric stretch; ν3
1090	PO_4^{3-}	Antisymmetric stretch; ν3
1160	H_2O	Librational
1607	H_2O	Bending; ν2
3180	H_2O	Symmetric stretching; ν1
3330	H_2O	ν1/ ν3
3540	H_2O	Antisymmetric stretching; ν3
3625	H_2O	ν1/ ν3

Typically the breadth of the OH stretching and H-O-H bending modes of water is indicative both of the degree of hydrogen bonding, particularly where several water bonding environments exist, and of the degree by which the location of the OH group is constrained. Thus these bands in the spectrum of TDT indicate that the water is located in a more definite position in the lattice than it is in the structure of francoisite-(Nd), a finding that is supported in

another TDT study (Locock and Burns, 2002). It is also probable that the bands due to coordinated and lattice water overlap and are unresolved (Vochten, 1990).

4. DISCUSSION

4.1. ATR-IR and Raman spectroscopy

4.1a Interstitial Metal Coordination

For hydrated metals in solids, it has been shown that a correlation exists between metal charge and the vibrational frequency of the coordinated water modes. Metal cations with higher oxidation states effectively shift the electronic charge in the oxygen atom, resulting in a lowering of the OH frequency (Vochten, 1990). This may explain the fact that the most prominent TDT ν_3 H_2O band (3540 cm^{-1}) is at higher frequency than that of francoisite-(Nd) (3430 cm^{-1}). The trivalent Nd coordinated by water molecules may result in a reduction in the frequency of the ν_3 mode relative to that of the divalent UO_2 in TDT.

In accordance with several workers who have associated the highest energy, most intense band to that of the antisymmetric stretching mode of water (Farmer and Lazarev, 1974; Cejka, 1999; Frost, 2006a), we have likewise assigned these bands to the antisymmetric stretching modes of water. That the highest frequency TDT band is both sharper and located at a higher wavenumber than francoisite-(Nd) can also be explained by the local coordination of the water molecules in both materials. In the case of francoisite-(Nd), it has been reported that five water molecules are coordinated to the interstitial Nd polyhedra (Piret et al., 1988). In addition, one occluded water resides in the open space between Nd polyhedra presumably weakly bonded to the coordinated water and/or oxygen via hydrogen bonding. In contrast, the TDT phase features

three coordinated water molecules to the interstitial U and four occluded water molecules (Locock and Burns, 2002).

The relative frequencies of the bending vibrations of water (ν_2) for TDT and francoisite-(Nd) provide further insight into the bonding environments of water in these materials. For example, we observed that higher stretching frequencies are associated with lower bending frequencies. In the case of TDT the most prominent stretching and bending modes are 3540 cm^{-1} and 1607 cm^{-1} respectively (Fig. 6; Table 5). The corresponding modes absorb at 3430 cm^{-1} and 1630 cm^{-1}, respectively for francoisite-(Nd) (Fig. 5; Table 4). This negative correlation is common and has been thoroughly addressed elsewhere (Nyquist, 1963; Novak, 1974). According to Nyquist (1963), forces that impede the torsion of the OH group result in an increase in bending frequency. Thus in general, the less freedom of motion, (i.e., more restricted torsion), the higher the frequency of the bending mode. Hence, the local environment surrounding a water molecule has a measurable effect on the stretching and bending modes such that a relatively free molecule exhibits high stretching frequencies, and correspondingly, lower bending frequencies, since the OH groups are less restricted and exhibit enhanced torsional displacement.

The above conclusions are in line with published single-crystal XRD results. The additional occluded water molecules in TDT relative to francoisite-(Nd) result in a greater overall contribution of relatively short OH bonds and thus higher OH antisymmetric stretching frequencies. Moreover, the greater spatial intermolecular distance of the occluded water results in higher torsional OH bending and, correspondingly, a reduced OH bending frequency.

4.1b O-O bond distances and H_2O vibrational frequencies

The relative strength of hydrogen bonds can often be deduced from IR spectroscopy. In the case of water, stronger hydrogen bonding results in longer OH intramolecular bonds, leading to lower OH vibrational frequencies. As a result, the distance between neighboring water molecules (intermolecular H-bonding) can be estimated from the IR spectrum. This scenario is likely to occur in francoisite-(Nd) and TDT by hydrogen bonding between the "free" occluded water(s) and the waters (or oxygens) coordinated to the metal (Nd or uranyl respectively) in the interstitial regions of the respective materials.

The correlation between OH vibrational frequencies and O-O bond length was investigated by Libowitzky (1999). In this study a relationship between the OH stretching mode and the associated O-O bond length was established for 65 different hydrated minerals. Libowitzky plotted these values and obtained the following mathematical relationship (R^2 = 0.96):

$$\nu = 3592 - 309 \cdot 10^9 \cdot \exp(-d/0.1321) \qquad (1)$$

where ν represents the wavenumber of the OH stretching mode and *d* is the O-O bond length in the hydrogen bond (Å). Equation (1) has been applied to the antisymmetric vibrational modes for francoisite-(Nd) and TDT obtained from IR (Figs. 5 and 6 and Tables 4 and 5, respectively) and the calculated oxygen – oxygen distances are displayed in Table 6.

Table 6. Comparison of the calculated O-O bond distances in Å (from Libowitzky, 1999) and their relationship to the frequency of the v3 H_2O mode. In addition, the experimentally obtained value (single-crystal XRD) for the natural francoisite sample is compared. Note the experimentally obtained value is the average of the total number of OH-O bond lengths reported by Piret et al. (1988). These bond lengths were not reported in the Locock and Burns (2002) single crystal analysis of TDT.

M*aterial*	**Mode**	**cm^{-1}**	**O(H)-O(calc)**	**O(H)-O (exp)**
Francoisite-(Nd)	*v*3 H_2O	3430	2.821 (±0.11)	2.822 (±0.05)
TDT	*v*3 H_2O	3530	2.948 (±0.12)	n/a

In their single-crystal XRD study of natural francoisite-(Nd), Piret et al. (1988) reported the O-O bond distances for all the hydrogen bonds (occluded and coordinated water). Interestingly, the average value of the total of these bonds matches the calculated value for the highest energy water mode in the synthetic francoisite-(Nd) sample in the IR spectrum (Table 6), and it is well within the error reported by Piret et al. (± 0.05 Å). Thus Equation (1) appears to be a viable approximation of the actual O-O bond distances for francoisite-(Nd). No experimental O-O bond length data for TDT are available at this time; however, based upon the agreement between the experimental and calculated values for francoisite-(Nd) it would appear that, even though the H-bonding is clearly very different, the calculated O-O bond length for TDT is a reasonable approximation.

4.1c. Calculating U=O bond lengths in francoisite-(Nd) and TDT

It has been widely shown that an inverse relationship exists between the bond length and the vibrational frequency of a particular moiety. This relationship can prove useful in determining bond lengths for systems where no crystallographic data exists, such as with synthetic francoisite-(Nd). Based on crystallographic and Raman data for a series of uranyl compounds, Bartlett and Cooney (1989) developed relatively simple relationships between the ν_1 and ν_3 modes of the uranyl ion and the corresponding U=O bond length. Typically the bond lengths for both U=O bonds in uranyl are very similar; however, in the case of non-negligible asymmetry, these calculations represent the average of the two U=O bond lengths.

For the uranyl symmetric stretching mode:

$$R_{UO}(pm) = 10650[\nu_1(cm^{-1})]^{-2/3} + 57.5 \quad (2)$$

while for the uranyl antisymmetric stretching mode:

$$R_{UO}(pm) = 9141[\nu_3(cm^{-1})]^{-2/3} + 80.4 \quad (3)$$

where R_{UO} represents the U=O bond length in picometers.

Since the ν_3 mode of uranyl is both Raman and IR active and the ν_1 mode is Raman active (and very prominent), both of these spectroscopic techniques can be used in a complementary manner to accrue U=O bond length information. The Raman spectra for francoisite-(Nd) and TDT are displayed in Figs. 7 and 8 respectively. The ν_1 and ν_3 UO_2 modes from Raman and ATR-IR experiments (respectively) in this study were used to calculate uranyl bond lengths for francoisite-(Nd) and TDT, the results of which are displayed in Table 7.

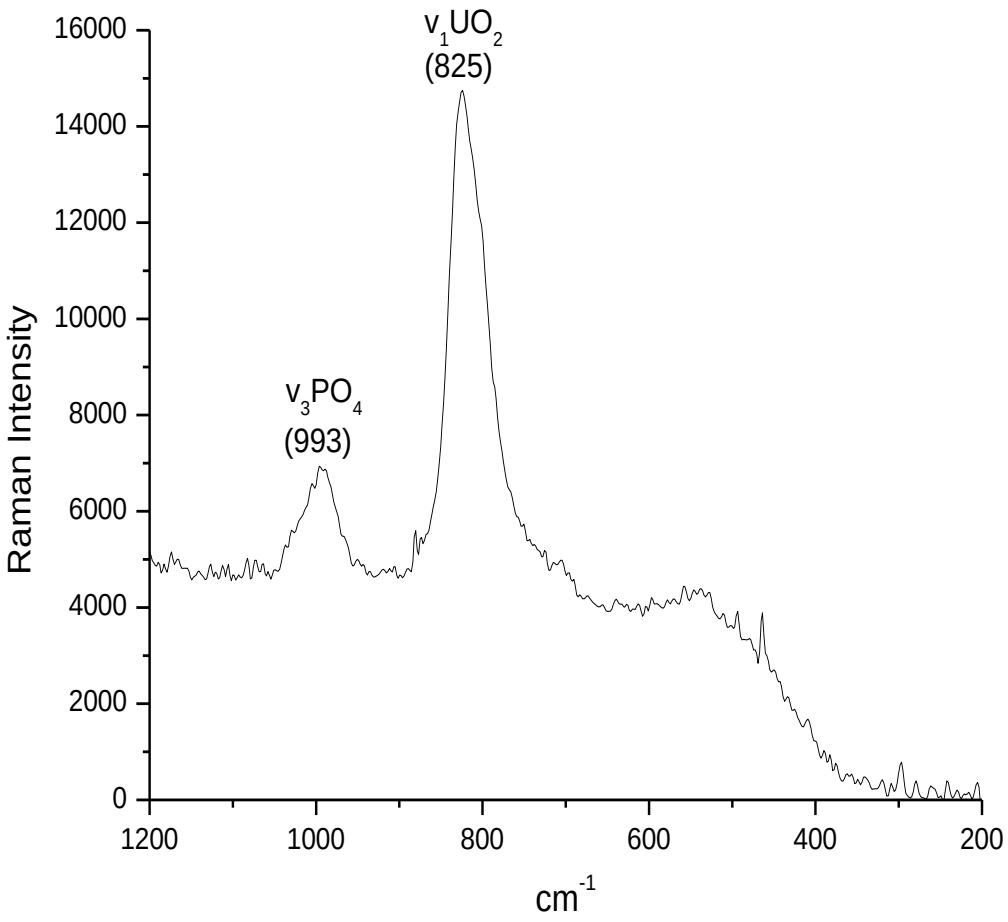

Fig. 7. Raman spectrum of francoisite-(Nd); HeNe laser; 632.8nm. Integration: 30s; Average of ten scans.

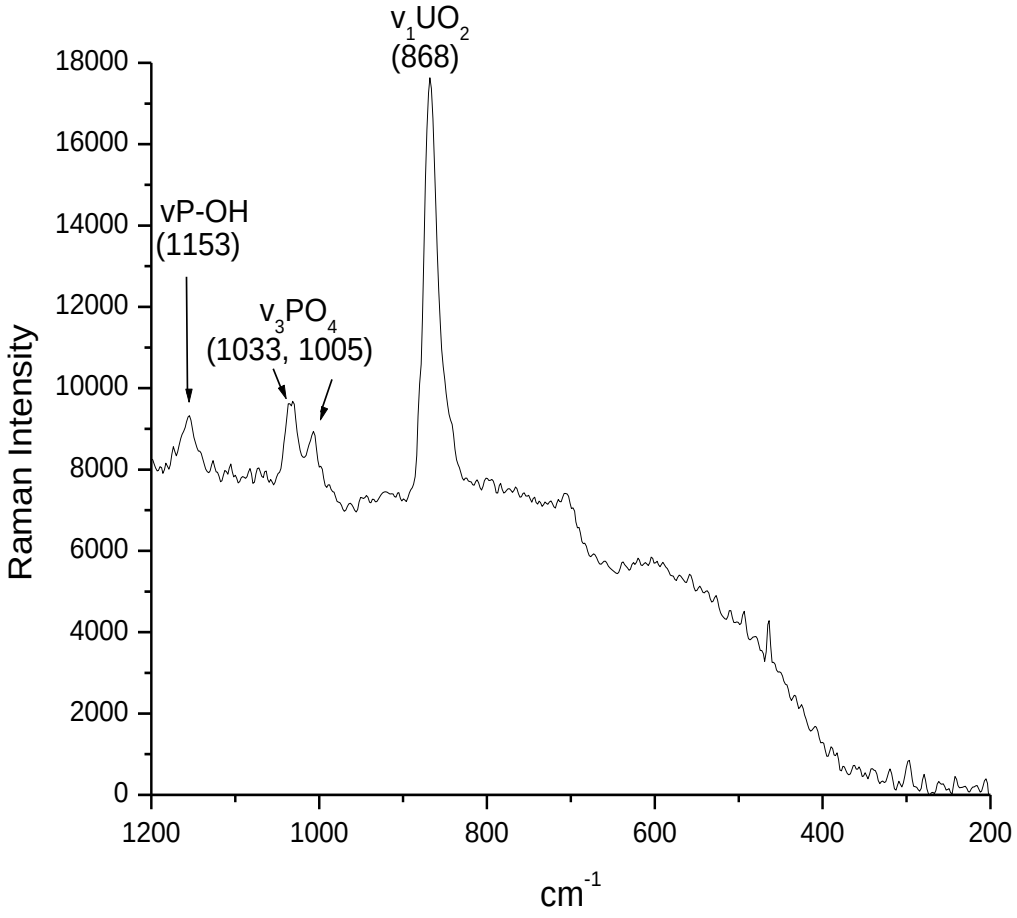

Fig. 8. Raman spectrum of TDT; HeNe laser; 632.8nm. Integration: 30s; Average of ten scans.

In general, the R_{U-O} values obtained from Equations (2) and (3) are in reasonable agreement with the U=O bond lengths obtained by crystallographic means. In the case of francoisite-(Nd) the calculated values underestimate the crystallographic U=O bond length. In contrast, the calculated R_{U-O} value for the ν_3 UO_2 mode from IR data for TDT appears to agree well with experimental value. It is possible that the ν_1 and ν_3 uranyl modes for both francoisite-(Nd) and TDT are split by crystal site splitting (Farmer and Lazarev, 1974; Vochten et al., 1984; Frost et al., 2006b). In the case of francoisite-(Nd), two distinct uranyl polyhedra are present in

the structural unit, one hexagonal bipyramid and two pentagonal bipyramids. The TDT structure features both structural and interlayer (interstitial) uranyl pentagonal bipyramids. These crystallographically nonequivalent structures are expected to result in additional uranyl vibrations in the infrared spectrum.

Table 7. Comparison between calculated and experimental uranyl bond lengths for francoisite-(Nd) (top) and TDT (bottom).

Instrument	**Mode**	**Wavenumber (cm^{-1})**	**R_{UO2} calculated (Å)**	**R_{UO2} crystall. (Å)**
Raman	ν1	825	1.785	[3]1.793
IR	ν3	905	1.781	
Instrument	**Mode**	**Wavenumber (cm^{-1})**	**R_{UO2} calculated (Å)**	**R_{UO2} crystall. (Å)**
Raman	ν1	868	1.745	[*]1.770
IR	ν3	917	1.772	

The crystallographic bond lengths shown in Table 7 represent the average of the values obtained. In addition, the bond length for francoisite-(Nd) that was obtained crystallographically is for the natural mineral (Piret et al., 1988). Therefore, small differences between the natural sample (which contains a host of impurities) and the synthetic sample are expected.

As mentioned previously, distinguishing between the antisymmetric stretching modes of PO_4 and UO_2 can be a challenge. However, these calculations can assist in the assignment of the

[3] Data obtained from single crystal XRD of natural sample (Piret et al., 1988)
[*] Data obtained from single crystal XRD of synthetic sample (Locock and Burns, 2002)

antisymmetric phosphate and uranyl stretching modes. For example the IR spectrum of TDT features the most intense band at 917 cm^{-1} (Fig. 6; Table 5). This band is in the vicinity of the antisymmetric stretching vibrations of both uranyl and phosphate. Using Equation (3), a value of 917 cm^{-1} for the ν_3 mode yields a U=O bond length of 1.772 Å. This value is in very good agreement with the reported uranyl bond length obtained from single-crystal XRD studies of TDT (Locock and Burns, 2002). Therefore it seems reasonable to assign this mode to the uranyl component, although the ν_3 mode of phosphate may be accidentally degenerate.

4.1d. Delineating OH and H_2O groups with IR spectroscopy

As noted above, Piret et al. (1988) presented data that suggested a hydroxyl group coordinated to uranyl in the structural unit of natural francoisite-(Nd). Here we attempt to verify this finding by examining well-characterized synthetic francoisite-(Nd) using IR spectroscopy. However, there are three main reasons why distinguishing between the vibrational bands of hydroxyl (U-OH) and H_2O components in francoisite-(Nd) is problematic. Firstly, the O-H stretching modes of U-OH and H_2O groups typically absorb at similar frequencies; and thus their respective bands frequently overlap. Secondly, H-bonding occurring between coordinated and occluded water in the interstitial region can result in significant ν_3 and ν_1 band broadening (ca. 3600 – 3000 cm^{-1}) effectively masking the U-OH band in this region. Lastly, regions in the spectrum that would otherwise indicate in-plane and out-of-plane U-OH bending modes are in the same spectral region as the most prominent phosphate vibrations. Thus these U-OH modes are either masked or overlapped in the high energy region of the mid IR (3600 – 3000 cm^{-1}) by water stretching modes and, correspondingly, in the middle range (ca. 1000 – 900 cm^{-1}) and at lower frequencies (700 – 490 cm^{-1}) by PO_4 components. However, by comparing the spectra of well-characterized

francoisite-(Nd) to that of TDT (no hydroxyl groups), information can be gleaned that supports the presence of U-OH bands in francoisite-(Nd).

The following tentative band assignments are made in agreement with Cejka (1999). The two weak bands at 1530 and 1360 cm^{-1} are assigned to the in-plane (δ) bending vibrations of U-OH (Fig. 5). Additionally, as noted above, it is possible that both in-plane (δ) and out-of-plane (γ) U-OH bending modes are present in roughly the same spectral regions as some phosphate stretching modes. These U-OH bending modes are common in uranyl hydroxo compounds (Cejka, 1999). For example, the shoulder at 1115 cm^{-1} might be associated with the U-OH out-of-plane bending mode. In addition, the weak mode at 798 cm^{-1} may also be attributed to a U-OH bend.

Further information can be gleaned regarding delineating H_2O and OH bands by examining the spectra of partially deuterated francoisite-(Nd) and TDT (Figs. 5 and 6 respectively). The characteristic isotopic shift to lower frequency in the stretching and bending modes of heavy water relative to H_2O is readily observed in the deuterated samples. Some additional observations are noteworthy. The weak bands tentatively assigned to δ U-OH in the protiated francoisite-(Nd) spectrum (1530 and 1360 cm^{-1}) together with the shoulder at 1115 cm^{-1} are not present in the deuterated francoisite-(Nd) spectrum. However a small band is present at 1210 cm^{-1} in the spectrum of deuterated francoisite-(Nd). In addition, the prominent band at ca. 1060 cm^{-1} is significantly broadened in the spectrum of deuterated francoisite-(Nd). It is possible that these bands are all associated with U-OH/ U-OD vibrations that are simply red-shifted in the deuterated compound. Therefore it may be possible that the δ U-OH modes shifted from ca. 1530 and 1360 cm^{-1} to ca. 1210 and 1080 cm^{-1}, respectively upon deuteration. Thus the prominent, sharp band in the H_2O compound is transformed to one encompassing both the v_3 PO_4 mode and the γ U-OD modes in the spectrum of deuterated francoisite-(Nd), resulting

in a broad overlapping band. In fact this feature looks like three unresolved bands in the spectrum of the deuterated material (Fig. 5).

This hypothesis appears to be supported by the spectra of protiated and deuterated TDT (Fig. 6). Apart from the expected isotopic H_2O – D_2O redshift, the influence of D_2O does not have the same effect as in francoisite-(Nd). The most prominent difference appears to be a weakening of intensity and sharpening of band width in the 1150 cm^{-1} band relative to the 1160 cm^{-1} band in the H_2O TDT spectrum. These features are tentatively assigned to the librational mode of H_2O. Thus, as expected, no U-OH band assignments are proposed in the TDT spectra. In general the most prominent bands in the spectrum remain relatively unchanged in the deuterated TDT spectrum. It is noteworthy that the francoisite-(Nd) and TDT compounds were synthesized with D_2O (rather than synthesized in H_2O and later deuterated) and thus minor spectral differences between the H_2O and D_2O derived materials are expected. It is also important to recognize that even though the deuterated samples were synthesized in 99% D_2O, significant H_2O is still present in the spectra. Thus the isotopic shift expected between these samples is expected to be lower than in pure H_2O and D_2O materials. It is further likely that some "OD" groups in the deuterated samples may indeed be protiated and thus no shift is observed. This would appear to be the case if the band ca. 798 cm^{-1} is indeed associated with U-OH, since negligible shifting of this band is observed between the protiated and deuterated samples, although a significant increase in intensity is observed in the deuterated francoisite-(Nd) at 798 cm^{-1}. Interestingly, an additional band appears in the deuterated sample that is seemingly not present in the protiated material at ca. 615 cm^{-1}. This may be attributed to the librational mode of water.

Although the band assignments for deuterated U-OH/U-OD are only tentative, the data presented herein appears to support the findings of Piret et al. (1988) and Locock and Burns

(2002) in their single crystal XRD studies of francoisite-(Nd) and TDT, respectively. Using a method developed by Donnay and Allman (1970) for recognizing O^{2-}, OH and H_2O groups with XRD, Piret et al. propose that a hydroxyl group acts as a central bridge between two pentagonal uranyl bipyramids and one hexagonal bipyramid. Our IR data, particularly as evidenced in the tentative U-OH assignments, appear to be in agreement with this finding.

4.1e Hygroscopic properties of francoisite-(Nd) and TDT

As mentioned previously, the width of the OH stretching bands and the degree of hydrogen bonding in the system are strongly related. However, it has also been shown that narrow, high frequency OH stretching bands are the result of weak hydrogen bonding (Libowitzky and Beran, 2006). As such, the sharp high energy band at ca. 3540 cm^{-1} in TDT likely represents the four occluded waters isolated from one another in the unit cell but H-bonded to coordinated water or oxygen in the interstitial uranyl bipyramids, each vibrating at a similar frequency. These occluded water molecules can be identified via IR spectroscopy by examining the TDT and francoisite-(Nd) samples after heating the crystals and concomitant water expulsion; see section 1.3.2 for details.

To examine the water features (ν_1, ν_2 and ν_3 vibrational modes) in the IR spectrum as a function of sample heating, separate samples of francoisite-(Nd) were heated to 80ºC and 500ºC and subsequently analyzed by ATR-IR. In the case of the sample heated to 80ºC, the francoisite-(Nd) crystals were placed in an oven overnight and subsequently allowed to cool in an enclosed oven at 25ºC for approximately two hours prior to ATR-IR analysis to minimize water readsorption. Samples heated to 500ºC were those that had been initially analyzed via TGA and allowed to cool in the open atmosphere for approximately two hours prior to ATR-IR analysis.

The spectra of the heated samples, along with that of a sample that had not been heated, are shown in Fig. EA-3 of Supplemental Data.

Samples of TDT were also heated and allowed to cool in the open atmosphere for approximately two hours prior to IR analysis. These spectra are depicted in Fig. EA-4 in Supplemental Data. The TDT heating temperatures were selected to approximate the regions between the most pronounced water expulsion events in the TGA/DSC temperature profiles (Fig. 3).

In the case of francoisite-(Nd) it is clearly seen that heating does not have a significant effect on the water features in the IR as the OH symmetric and antisymmetric stretching region (ca. 3205 and 3430 cm^{-1} respectively) and the H_2O bending mode at ca. 1630 cm^{-1} do not change appreciably due to sample heating. However the IR spectra of the TDT crystals show more pronounced changes in the stretching and bending modes of water. The sharp high energy band attributed to the antisymmetric mode of occluded water appears to weaken in the heated samples, while the water bending mode appears to sharpen as a function of temperature. Perhaps the most conspicuous change, however, is the marked decrease of band intensity at ca. 1160 cm^{-1} in the heated TDT crystals. This band may be attributed to librational water (Table 5), an external vibrational mode indicative of free (occluded) water, which is expected to be expelled from the solid as temperature is increased.

4.2. Water Sorption Verification: Reanalyzing the samples via TGA

From the TGA and DSC data presented above for francoisite-(Nd) and TDT, it is clearly seen that water is expelled from the solid as the temperature is increased from 25ºC to 500ºC. Yet IR data show that significant water remains in the samples that were heated. Two possibilities are

plausible for only minor changes observed in the water features (particularly in the case of francoisite-(Nd)) after heating (Fig. EA-3; Supplemental Data). First, it is likely that water is coordinated to the interstial Nd in francoisite-(Nd) in a manner similar to the coordination environment in the uranyl pentagonal bipyramid in TDT (Locock and Burns, 2002). In contrast to physisorbed and hydrogen bonded (occluded) water, the water molecules directly coordinated to the interstitial metal are probably difficult to expel even after considerable heating. Second, it is possible, and even probable, that some water readsorbed to the solid after the sample was subjected to heating and subsequently analyzed by ATR-IR. To test these hypotheses, duplicate samples were taken after heating to 500^{o}C and allowed to cool overnight. These duplicate samples of francoisite-(Nd) and TDT were subsequently *reanalyzed* by TGA from 25 to 500^{o}C at 5^{o}C/min, the data of which is depicted in Figs. 9 and 10, respectively. The total moles of water lost in both runs are displayed in Table 8. Clearly water is readsorbing in both francoisite-(Nd) and TDT, i.e., both samples are hygroscopic. Although the dehydration-rehydration process is not completely reversible, a significant proportion of the water lost in the initial heating experiment "resorbs", particularly with respect to TDT. In the case of francoisite-(Nd) approximately 3.35 moles of water has resorbed and 4.13 moles have reattached to the TDT solid. Although extensive studies have been undertaken on dehydration of autunite as a function of temperature by PXRD (Sowder, 1998; Wellman, 2004; Suzuki et al., 2005), to our knowledge these dehydration-rehydration TGA studies are the first to be reported.

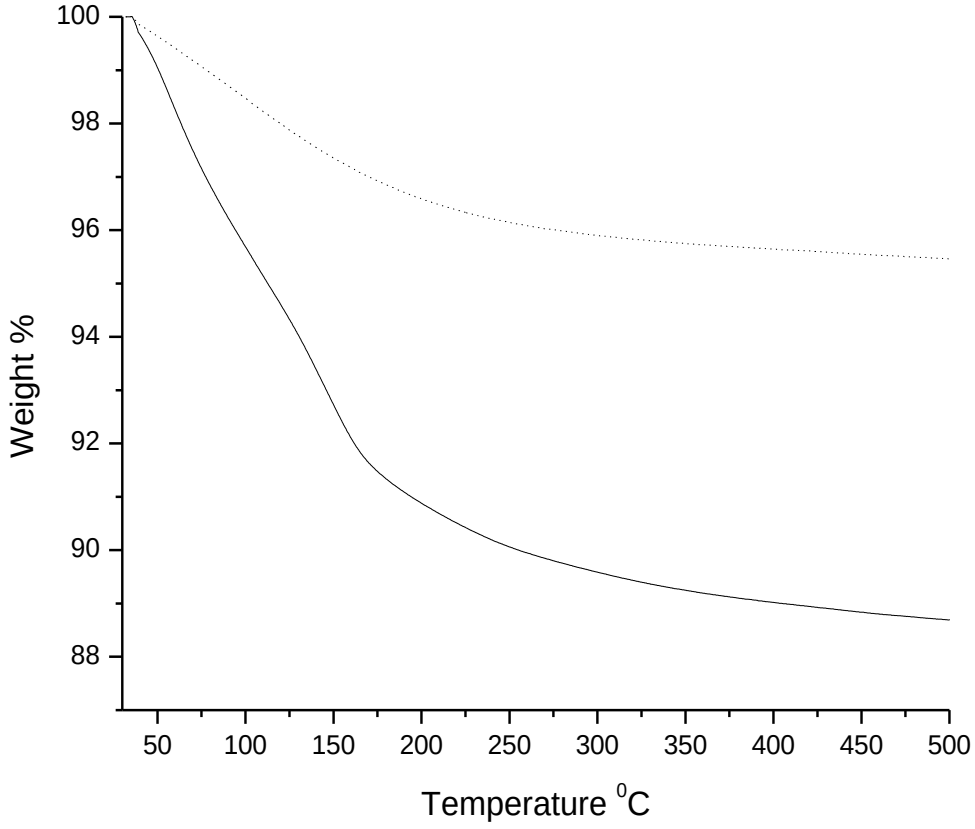

Fig. 9. Thermogravimetric analyses (TGA) conducted on francoisite-(Nd). The lower curve represents the average of duplicate runs. The upper dotted curve depicts a sample reanalyzed following a cooling period of two hours to evaluate possible water readsorption. All runs were conducted at 5 ^{o}C/min scan rate.

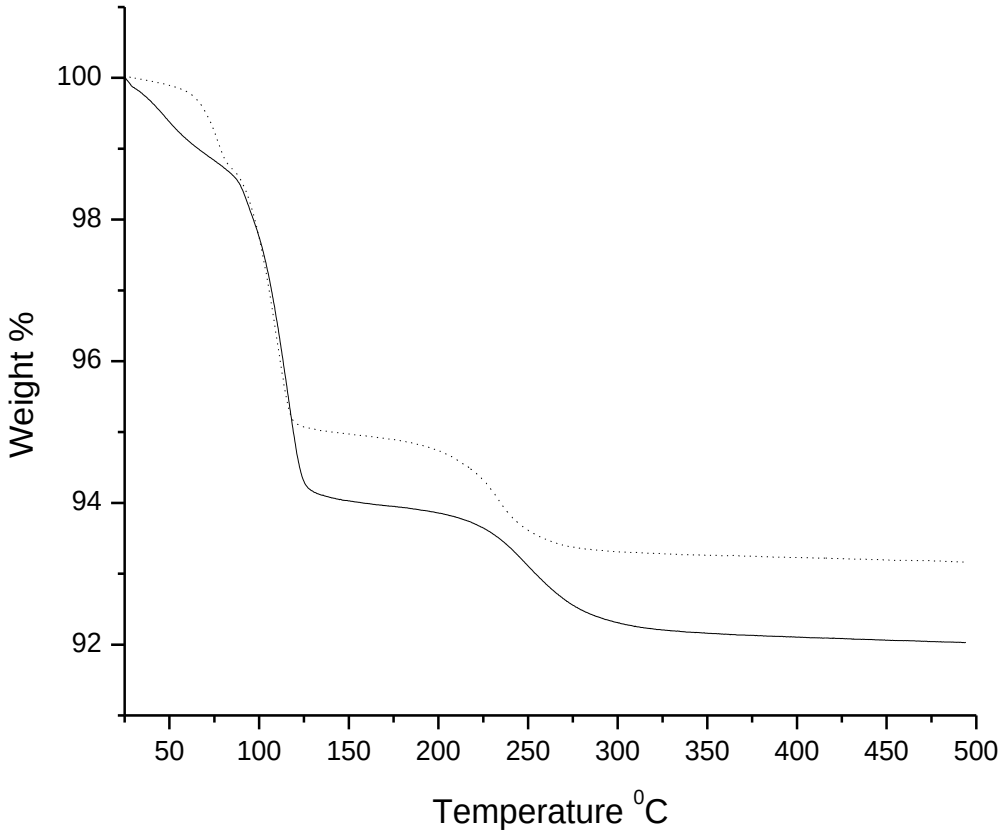

Fig. 10. Thermogravimetric analyses (TGA) conducted on TDT. The lower curve represents the average of duplicate runs. The upper dotted curve depicts a sample reanalyzed following a cooling period of two hours to evaluate possible water readsorption. All runs were conducted at 5 ^{o}C/min scan rate.

Table 8. Initial TGA and second TGA runs of the same samples following a cooling period of approximately two hours in the open atmosphere.

Material	Moles H_2O lost: Initial Run	Moles H_2O lost: 2nd Heating	% Readsorbed
Francoisite-(Nd)	8.36	3.35	40.2
TDT	4.81	4.13	85.8

Interestingly, the TDT crystals resorbed more water than francoisite-(Nd) (Table 8). Also, although in general the reheated thermograms appear to exhibit similar temperature profiles to the initial runs (albeit displaced vertically due to less water expulsion) some differences are worth noting. In the case of francoisite-(Nd) the reheated sample features a more gradual water loss profile than the initial run and no plateau is observed until the highest temperature in either run. In contrast, the reheated TDT sample features a pseudoplateau at low temperature but the slopes of both profiles are almost identical at elevated temperatures. These findings suggest that the presence of water in the IR spectra of the heated samples in Fig. E-A4 (Supplemental Data) is indicative of both interstitially occluded and coordinated water (i.e., adsorbed and absorbed water). The temperature profile in the reheated TDT suggests that the resorbed water has reincorporated back into the lattice, as evidenced by the sharp slopes and plateau regions above 100ºC. Correspondingly, TDT showed more pronounced changes in the IR spectrum due to heating than francoisite-(Nd). Therefore, the higher vibrational frequency evidenced in the OH antisymmetric stretching mode in TDT relative to francoisite-(Nd) seems likely due to i) more occluded waters and, ii) the coordination environment (divalent vs. trivalent) of uranyl relative to Nd in the interstitial metals of TDT and francoisite-(Nd), respectively.

5. SUMMARY

The empirical formula of francoisite-(Nd) was determined to be $Nd[(UO_2)_{3.38}(OH)(PO_4)_2]\bullet 5.16H_2O$, while that of triuranyl diphosphate tetrahydrate was $(UO_2)_{3.13}(PO_4)_2\bullet 3.91H_2O$. Slight deviations from the ideal stoichiometries of these materials were attributed to residual sodium present in the samples. Powder XRD was conducted on these samples and very good agreement between the samples synthesized in this study and the available published data was observed.

To delineate distinct water populations, a method developed by Hawthorne (1992) was employed and the unit formulas thus obtained for francoisite-(Nd) and TDT were $\mathbf{Nd[(UO_2)_3O(OH)(PO_4)_2]\cdot 5.2H_2O}$ and $\mathbf{UO_2(H_2O)_{1.3}[(UO_2)_5(PO_4)_4]\cdot 2.6H_2O}$, respectively.

A vibrational spectroscopic study was conducted on these materials using ATR-IR and Raman spectrometry. Tentative band assignments for the UO_2^{2+}, PO_4^{3-}, and H_2O modes were determined. The TGA, DSC, IR and Raman data showed that both francoisite-(Nd) and TDT were strongly hydrated. In addition, the rapid readsorption of water molecules on both samples was confirmed. The increased energy observed in the antisymmetric stretching mode of water in the TDT relative to francoisite-(Nd) was attributed to two factors, i) the increased number of free or weakly bound (occluded) waters in the TDT lattice and, ii) the divalent interstitial uranyl in TDT relative to the trivalent interstitial Nd in francoisite-(Nd). The bond lengths for both O-O (in intermolecular H-bonding) and U=O were estimated for both phases based upon empirical calculations and reasonable agreement between the calculated bond lengths and those reported from single-crystal XRD analyses was observed. The IR spectra of protiated and deuterated francoisite-(Nd) confirmed a coordinated hydroxyl group bridging vicinal uranyl groups in the francoisite-(Nd) structural unit.

Because of their low solubility, actinide and lanthanide phosphates are highly stable. The likelihood of these materials occurring near spent nuclear fuel in natural systems makes it necessary to understand the chemistry of *f*-element phosphate interactions in natural systems to predict the fate of such metals over a geological time scale. The studies reported above provide the basis for further thermodynamic (solubility, sorption) and geochemical modeling investigations.

ACKNOWLEDGEMENTS

At Washington State University, this work was supported primarily by the U.S. Department of Energy, Basic Energy Sciences, Heavy Element Chemistry program, contract DE-FG02-06ER15782. In addition, SBC and CRA acknowledge support from the Joint Domestic Nuclear Detection Office-National Science Foundation: Academic Research Initiative (ARI), contract number ECCS-0833548 during the preparation of this manuscript. We also thank Dr. Louis Scudiero (WSU) for his assistance with TGA and DSC analyses and the WSU Geological Sciences Department for allowing CRA to use the PXRD.

REFERENCES

Bartlett, J.R., Cooney, R.P. (1989) On the determination of uranium-oxygen bond lengths in dioxouranium(VI) compounds by Raman Spectroscopy. *J. Mol. Struc.* **193**, 295-300.

Bray, T.H., Gorden, J.D., Albrecht-Schmitt, T.E. (2008) Synthesis and structure of $[C_6H_{14}N_2][(UO_2)_4(HPO_4)_2(PO_4)_2(H_2O)]\cdot H_2O$: An expanded open-framework amine-bearing uranyl phosphate. *J. Sol. State Chem.* **181**, 2199-2204.

Buck, E.C., Brown, N.R., Dietz, N.L. (1996) Contaminant uranium phases and leaching at the Fernald site in Ohio. *Environ. Sci. Tech.* **30**, 81-88.

Burns, P.C., Miller, M.L., Ewing, R.C. (1996) U^{6+} minerals and inorganic phases: A comparison and hierarchy of crystal structures. *Can. Mineral.* **34**. 845-880.

Burns, P.C. (1999) The crystal chemistry of uranium. In: Reviews in Mineralogy Vol. 38. Eds. Burns, P.C., Finch, R. Mineralogical Society of America. 23-86.

Burns, P.C. (2005) U^{6+} minerals and inorganic compounds: Insights into an expanded structural hierarchy of crystal structures. *Can. Mineral*. **43**, 1839-1894.

Cejka, J. (1999) Infrared spectroscopy and thermal analysis of uranyl minerals. In: Reviews in Mineralogy Vol. 38. Eds. Burns, P.C., Finch, R. Mineralogical Society of America. 521-622.

Donnay, G., Allmann, R. (1970) How to recognize O^{2-}, OH^- and H_2O in crystal structure determination by X-ray. *Amer. Mineral*. **55**, 1003-1015.

Elless, M.P., Lee, S.Y. (1998) Uranium solubility of carbonate-rich uranium-contaminated soils. *Water, Air, Soil Pollut*. **107**, 147-162.

Farmer, V.C., Lazarev, A.N. (1974) The Anhydrous Oxide Minerals. In: The infra-red spectra of minerals. Ed. Farmer, V.C. Mineralogical Society and the Macauley Instutute for Soil Research. 183-205.

Felmy, A.R., Xia, Y., Wang, Z. (2005) The solubility product of $NaUO_2PO_4 \cdot xH_2O$ determined in phosphate and carbonate solutions. *Radiochim. Acta.* **93**, 401-408.

Frost, R.L., Weir, M. (2004a) Raman Spectroscopy of autunite minerals at liquid nitrogen temperature. *Spectrochim. Acta Part A.* **60**, 2399-2409.

Frost, R.L., Weir, M., Adebajo, M.O. (2004b) Thermal decomposition of metazeunerite – a high-resolution thermogravimetric and hot-stage Raman spectroscopic study. *Thermochim. Acta*. **419**, 119-129.

Frost, R.L., Cejka, J., Weir, M. (2006a) Raman spectroscopic study of uranyl oxyhydroxide hydrates: bequerelite, billietite, curite, shoepite, and vandendriesscheite. *J. Raman Spec*. **38**, 460-466.

Frost, R.L., Weir, M.L., Martens, W., Cejka, J. (2006b) The structure of phurcalite – A vibrational spectroscopic study. *Vib. Spec*. **41**, 205-212.

Giammar, D.E., Hering, J.G. (2002) Equilibrium and kinetic aspects of soddyite dissolution and secondary phase precipitation in aqueous suspension. *Geochim. Cosmochim. Acta*. **66**, 3235-3245.

Giammar, D.E. Xie, L., Pasteris, J.D. (2008) Immobilization of lead with nanocrystalline carbonated apatite present in fish bone. *Environ. Eng. Sci*. **25**, 725-736.

Gorman-Lewis, D.J., Mazeina, L., Fein, B., Szymanowski, J., Burns, P.C., Navrotzky, A. (2007) Thermodynamic properties of soddyite from solubility and calorimetry measurements. *J. Chem. Thermodyn*. **39**, 568-575.

Griffiths, P.R., de Haseth, J.A. Fourier Transform Infrared Spectrometry (2007) John Wiley & Sons, Inc. 529 pp.

Hawthorne, F.C. (1992) The role of OH and H_2O in oxide and oxysalt minerals. *Zeit. Fur Kristall*. **201**, 183-206.

Hawthorne, F.C., Schindler, M. (2008) Understanding the weakly bonded constituents in oxysalt minerals. *Zeit. Fur Kristall*. **223**, 41-68.

Ilton, E.S., Liu, C.X., Yantasee, W., Wang, Z.M., Moore, D.A., Felmy, A.R., Zachara, J.M. (2006) The dissolution of synthetic Na-boltwoodite in sodium carbonate solutions. *Geochim. Cosmochim. Acta*. **70**, 4836-4849.

Khosrawan-Sazedj, F. (1982) On the space group of threadgoldite. *Tschermaks Mineral. Petrogr. Mitt*. **30**, 111-115.

Kim, C.W., Wronkiewicz, D.J., Buck, E.C. (1999**)** Incorporation of radionuclides in the alteration phases of spent nuclear fuel. Migration Conference. Lake Tahoe, NV, USA.

Libowitzky, E. (1999) Correlation of the O-H stretching frequencies and O-H···O hydrogen bond lengths in minerals. *Monat. fur Chem*. **130**, 1047-1059.

Libowitzky, E., Beran, A. (2006) The Structure of hydrous species in nominally anhydrous minerals: Information from polarized IR spectroscopy. In: Reviews in Mineralogy Vol. 62. Eds. Keppler, H., Smyth, J.R. Mineralogical Society of America. 29-52.

Locock, A.J., Burns, P.C. (2002) The crystal structure of triuranyl diphosphate tetrahydrate. *J. Sol. State Chem.* **163**, 275-280.

Locock, A.J., Burns, P.C. (2003a) Crystal structures and synthesis of the copper-dominant members of the autunite and meta-autunite groups: torbenite, zeunerite, metatorbernite and metazeunerite. *Can. Mineral*. **41**, 489-502.

Locock, A.J., Burns, P.C. (2003b) The crystal structure of synthetic autunite. *Amer. Mineral.* **88**, 240-244.

Locock, A.J., Burns, P.C, Duke, M.J.M., Flynn, T.M. (2004) Monovalent cations in structures of the meta-autunite group. *Can. Mineral.* **42**, 973-996.

Markovic., M., Pavkovic, N. (1983) Solubility and equilibrium constants of uranyl(2+) in phosphate solutions. *Inorg. Chem.* 22, 978-982.

Meinrath, G., Kimura, T. (1993) Behavior of uranium (VI) solids under conditions of natural aquatic systems. *Inorg. Chem. Acta*. **204**, 79-85.

Nguyen, S.N., Silva, R.J., Weed, H.C., Andrews, J.E. (1992) Standard Gibbs free energies of formation at the temperature 303.15 K of four uranyl silicates: soddyite, uranophane, sodium boltwoodite, and sodium weeksite. *J. Chem. Thermodyn*. **24**, 359-376.

Novak, A. (1974) In: Structure and Bonding 18. Eds. Dunitz, J.D., Konstanz, P.H., Holm, R.H., Ibers, J. A., Jorgensen, C.K., Neilands, J.B., Reinen, D., Williams, R.J.P. Springer-Verlag. 177-216.

Nyquist, R.A. (1963) The O-H out-of-plane deformation in intramolecularly hydrogen bonded phenols. *Spectrochim. Acta* **19**, 1655-1664.

Pham-Thi, M., Colomban, Ph. (1985) Morphological, X-ray and vibrational study of various uranyl phosphate hydrates. *J. Less-Common Met*. **108**, 189-216.

Piret, P., Deliens, M., Piret-Meunier. (1988) La francoisite-(Nd), nouveau phosphate d'uranyle et de terre rares; proprietes et structures cristalline. *Bull. Mineral.* **111**, 443-449.

Rai, B.D., Felmy, A.R., Hess, N.J., LeGore, V.L., McCready, D.E. (2002) Thermodynamics of the U(VI)-Ca^{2+}-Cl^{-}-OH^{-}-H_2O system: Solubility product of becquerelite. *Radiochim. Acta* **90**, 495-503.

Rai, B.D., Xia, Y., Rao, L., Hess, N.J., Felmy, A.R., Moore, D.A., McCready, D.E. (2005) Solubility of $(UO_2)_3(PO_4)_2 \cdot 4H_2O$ in H^{+}-Na^{+}-OH^{-}- H_2PO_4 -PO_4^{3-} - H_2O and its comparison to the analogous PuO_2^{2+} system. *J. Sol. Chem.* **34**, 469-498.

Schiffer, J., Intenzo, M., Hayward, P., Calabrese, C. (1976) The FS correlation and a systematic analysis of the stretching absorptions of water in the condensed state. *J. Chem. Phys.* **64**, 3014-3020.

Schindler, M., Hawthorne, F.C. (2008) The stereochemistry and chemical composition of interstitial complexes in uranyl-oxysalt minerals. *Can. Mineral*. **46**, 467-501.

Sowder, A.G. (1998) The formation, transformation, and stability of environmentally relevant uranyl mineral phases. PhD dissertation, Clemson University.

Suzuki, Y., Sato, T., Isobe, H., Kogure, T., Murakami, T. (2005) Dehydration processes in the meta-autunite group minerals meta-autunite, metasaleeite, and metatorbernite. *Amer. Mineral*. **90**, 1308-1314.

Thomas, A., Dacheux, N., Le Coustumer, P., Brandel, V., Genet, M. (2001) Kinetic and thermodynamic studies of the dissolution of thorium-uranium (IV) phosphate-diphosphate solid solutions. *J. Nucl. Mater*. **295,** 249-264.

Van Haverbeke, Vochten, R., Van Springel, K. (1996) Solubility and spectrochemical characteristics of synthetic chernikovite and meta-ankoleite. *Mineral. Mag.* **60**, 759-766.

Vesely, V., Pekarek, V., Abbrent, M. (1965) A study of uranyl phosphates III Solubility products of uranyl hydrogen phosphate, uranyl orthophosphate and some alkali uranyl phosphates. *J. Inorg. Nucl. Chem*. **27**, 1159-1166.

Vochten, R., De Grave, E., Pelsmaekers, J. (1984) Mineralogical study of bassetite in relation to its oxidation. *Amer. Mineral.* **69**, 967-978.

Vochten, R. (1990) Transformation of chernikovite and sodium autunite into lehnerite. *Amer. Mineral*. **75**, 221-225.

Wellman, D.M. (2004) Environmental availability of uranium from secondary uranyl minerals. PhD dissertation, Washington State University.

Wellman, D.M., Icenhower, J.P., Owen, A.T. 2006. Environ. Chem. 3. 219-224.

Womack, J.C., Larkin, D.J. (1971) ARH-2035. Richland, WA, USA.

Wright, J., Conca, J. 2002. RTDF PRB Action Meeting. Nov. 6-7.

Yu, Y., Albrecht-Schmitt, T.E. (2008) Incorporation of tetrahedral Co(II) into a mixed-metal uranyl phosphate framework: Synthesis and structure of $K_2[UO_2Co(PO_4)_2]\cdot H_2O$. *Sol. State Sci.* **10**, 821-824.

Yu, Y., Zhan, W., Albrecht-Schmitt, T.E. (2008) $[H_2bipy]_2[(UO_2)_6Zn_2(PO_3OH)_4(PO_4)_4]\cdot H_2O$: An open framework uranyl zinc phosphate templated by diprotonated 4,4'-bipyridyl. *Inorg. Chem*. **47**, 9050-9054.

ELECTRONIC INDEX EA

Spectroscopic and Thermal Study of Hydrated Uranyl Phosphates: Francoisite-(Nd) and Triuranyl Diphosphate Tetrahydrate

Christopher R. Armstrong,[a,] Kenneth L. Nash,[a] Peter R. Griffiths,[b] Sue B. Clark,[a,*]

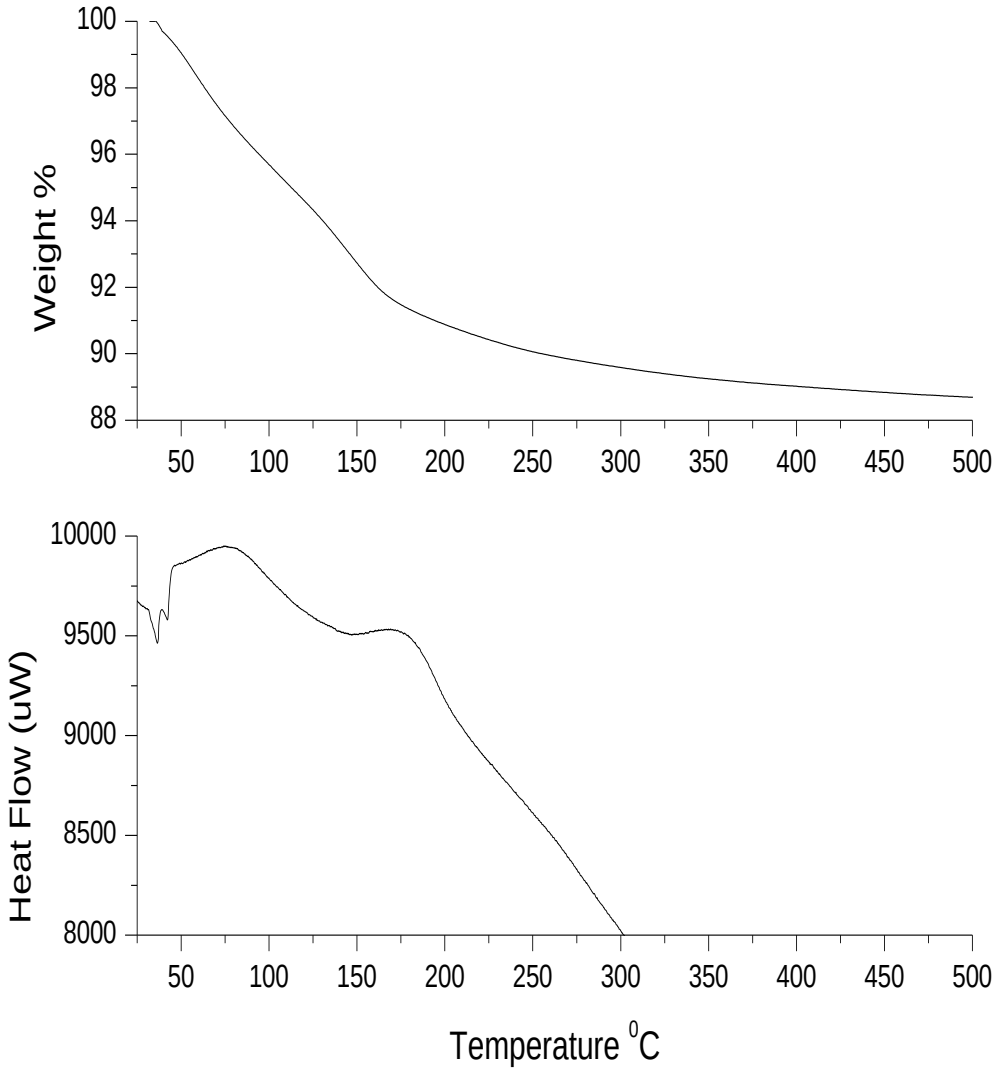

Fig.EA- 1. TGA (top) and DSC (bottom) for francoisite-(Nd). Both TGA and DSC plots represent the average of duplicate runs. All runs were conducted at 5 ^{o}C/min scan rate.

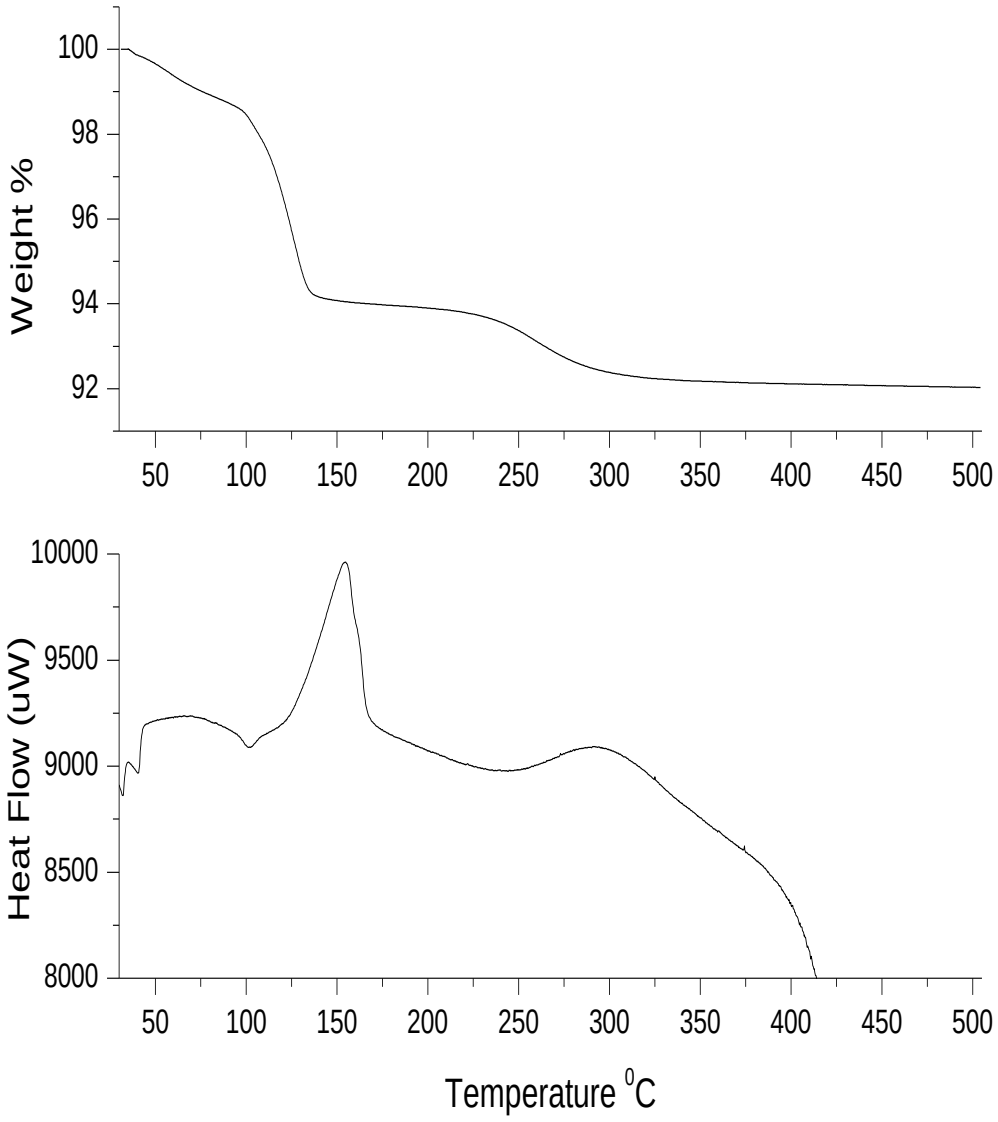

Fig. EA-2. TGA (top) and DSC (bottom) for TDT. Both TGA and DSC plots represent the average of duplicate runs. All runs were conducted at 5 ^{o}C/min scan rate.

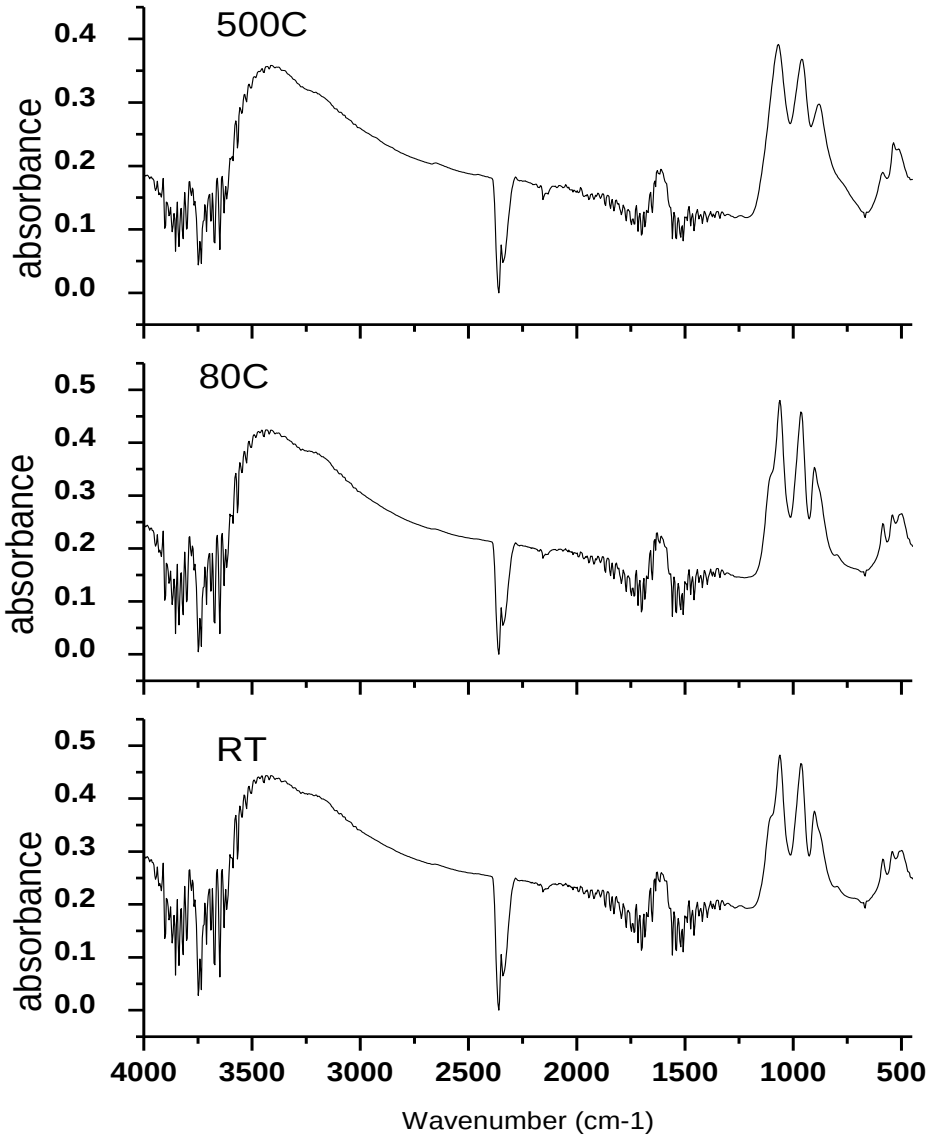

Fig.E-A3. Comparison of francoisite-(Nd) IR data for room temperature (RT) and samples heated to 80 ^{o}C and 500 ^{o}C.

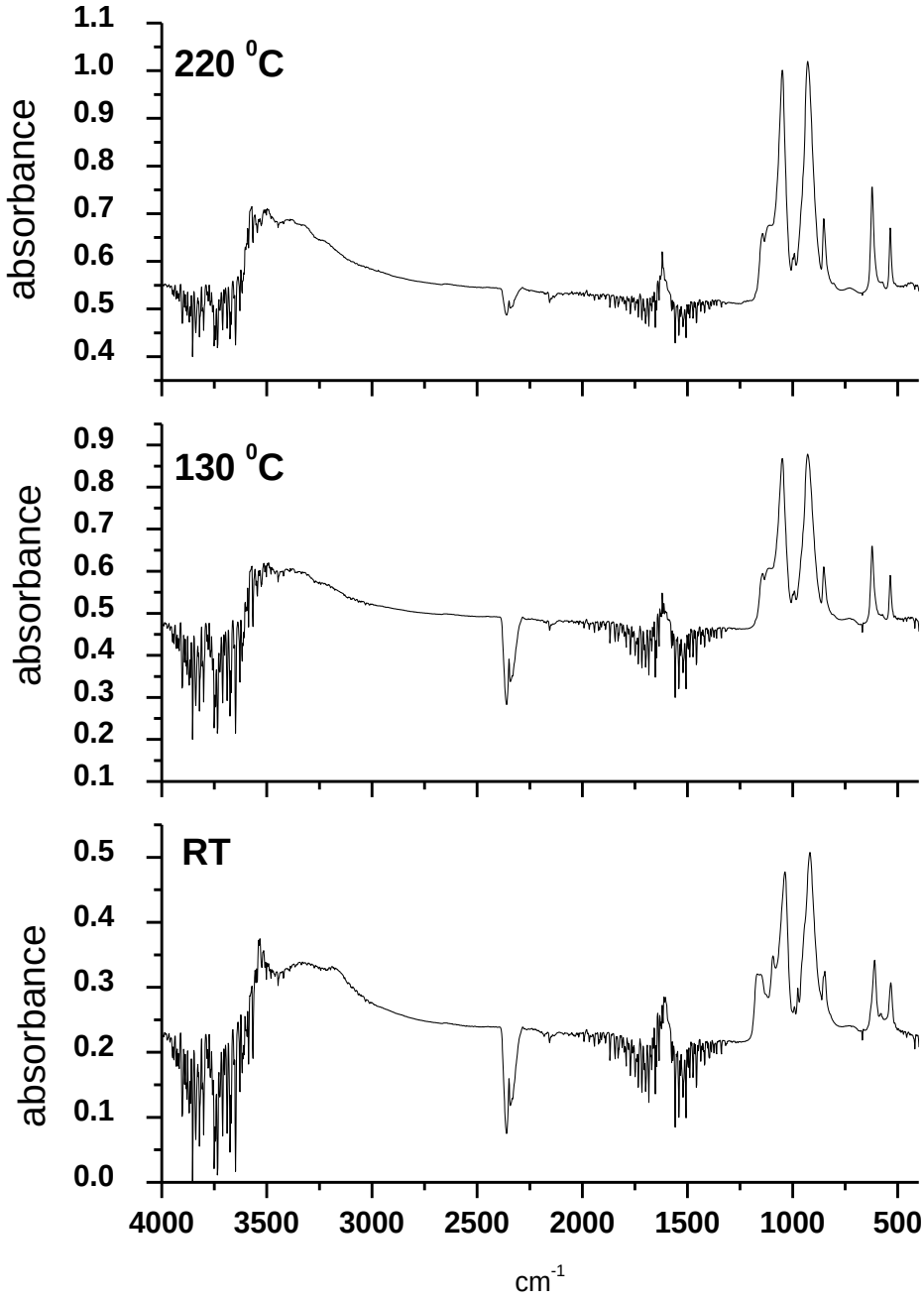

Fig. E-A4. ATR-IR spectra of TDT at various temperatures. The crystals were analyzed at room temperature (bottom spectrum) after heating overnight at 130°C (middle spectrum) and to 220°C (top spectrum).

CHAPTER THREE

Delineating Hydrated Uranyl Phosphates: Powder XRD and ATR-IR Studies

Christopher R. Armstrong and Sue B. Clark

Department of Chemistry, Washington State University, Pullman, WA 99164 U.S.A.

Corresponding author: s_clark@wsu.edu

Abstract. In this report a complementary approach using powder x-ray diffraction (PXRD) and attenuated total reflection (ATR) IR spectroscopy is evaluated with an emphasis on (i) delineating isostructural (Na autunite ($Na[(UO_2)(PO_4)]•1.5H_2O$) and chernikovite ($H_3O[(UO_2)(PO_4)]•4H_2O$)) and structurally distinct (triuranyl diphosphate tetrahydrate $(UO_2)_3(PO_4)_2•4H_2O$) hydrated uranyl phosphates. Our results show that this complementary approach, when used in conjunction with elemental analysis, affords very accurate and reliable identification and characterization of hydrated uranyl phosphates.

1. Introduction

Predicting the behavior of uranium in the environment and designing effective remediation strategies for uranium contamination require knowledge of thermodynamic parameters, such as solubilities of relevant mineral phases, to estimate groundwater concentrations and identify possible solid phases for in-situ immobilization. The hexavalent uranium phosphate phases known collectively as the autunites consist of a variety of isostructural layered minerals that vary according to the metal ion occupancy in the interlayer [1]. Unfortunately, the reported solubilities for the autunite phases often differ by many orders of magnitude [2], which may be attributed to poor characterization of the solid phase. Because of their structural similarities, delineating the end member autunites (e.g., chernikovite ($H_3O[(UO_2)(PO_4)]\bullet xH_2O$), sodium autunite ($Na[(UO_2)(PO_4)]\bullet xH_2O$), meta autunite ($Ca[(UO_2)(PO_4)]_2\bullet xH_2O$), and their solid solutions (i.e., mixtures of these phases) is challenging. Typical methods for characterization are either thermal analysis, x-ray diffraction, or vibrational spectroscopy, e.g. attenuated total reflection infrared (ATR-IR), but rarely do investigators employ all these approaches simultaneously.

For this study, three synthetic hydrated uranyl phosphates, Na autunite, chernikovite and triuranyl diphosphate tetrahydrate ($(UO_2)_3(PO_4)_2\cdot 4H_2O$) were investigated. Because they are isostructural, Na autunite and chernikovite are often difficult to distinguish. Synthetic chernikovite and TDT are of interest because although they are not isostructural, they can easily be misidentified. Here, we describe a rigorous solid phase characterization approach for the unique identification of these solids; it is based on (1) elemental analysis, (2) powder x-ray diffraction (PXRD), (3) ATR-IR and (4) thermogravimetric analysis (TGA).

1.1.General problems with U-solid characterization using PXRD

In PXRD, the scattering magnitude of an atom in a unit cell is proportional to the atom's atomic number. Hence, for uranyl compounds the diffraction of U tends to dominate the XRD profile; and consequently, diffractograms of different U-phases can be very difficult to distinguish [3]. Additionally, it has been shown that the degree of hydration in uranyl compounds can have a significant effect on the 2-theta position and d-spacing of the reflections. For example, some d-spacing distances increase with hydration; and this is attributed to interlayer swelling. For example, the same phase with different hydration, i.e., $(UO_2)_3(PO_4)_2{\cdot}4H_2O$ vs. $(UO_2)_3(PO_4)_2{\cdot}6H_2O$, can result in a shift to a lower 2-theta position [4, 5, 6, 7]. This trend has been observed in a variety of uranyl compounds, including other hydrated uranyl phosphates [8, 9], as well as uranyl silicates and oxy-hydroxides [10]. Thus, using PXRD alone to identify synthetic hydrated uranyl compounds, particularly phosphates or silicates for which the hydration state is unknown, is tenuous at best.

1.2. General problems with U-solid characterization using IR

Variations in sample preparation can greatly affect the IR spectrum [11]. For example, overgrinding the solid can result in significant structural changes that can have a marked effect on the resulting spectra. In addition, ion exchange between diluents such as KBr and the sample can result in band broadening and lower intensity [12, 13]. However, ATR-IR eliminates these issues. Because the depth of penetration, d_p, is only about a quarter of the wavelength, a very thin sample (<10 μm) is not necessary. Moreover, with ATR-IR, solid samples do not need to be diluted (e.g., with KBr) and can be analyzed in their neat state. On the other hand, because ATR-IR is largely a surface technique, the presence of atmospheric water on the surface of the hygroscopic solid is difficult to avoid. Consequently, delineating physisorbed water and

stoichiometric water (i.e., water located in the interstitial region or structural unit of the compound) is difficult.

2. Experimental Methods

All chemicals are reagent grade or higher. Distilled 18MΩ and boiled water was used in preparations of all solutions. Standards used for ICP-OES analyses were 99.9% purity.

2.1. Synthetic uranyl compounds

Solution and suspension pH was measured with a ThermoElectron Corp. Orion 4 Star pH meter equipped with a Ross combination pH electrode (Orion Model 8102). Prior to each use, the pH electrode was calibrated with NIST standards. For hydrothermal reactions, 23- and 45-mL Teflon® liners were placed inside stainless steel Parr acid digestion bombs.

2.1.1. Synthesis of TDT: $(UO_2)_2(PO_4)_3{\cdot}4H_2O(c)$. Microcrystalline TDT was synthesized according to the modified method of Rai et al. [7]. Briefly, stoichiometric volumes of 0.7 M H_3PO_4 and 0.05M $UO_2(NO_3)_2{\cdot}6H_2O$ were mixed in a jacketed reaction vessel under N_2 atmosphere at 40°C (± 0.1). Precipitation was observed immediately, and the suspension pH was ca. 1. The suspension was stirred overnight at 40°C and subsequently allowed to settle, after which the supernatant was decanted and replaced with degassed 18 MΩ water at 40°C twice. From the mixed suspension, a sample of approximately 60 mL was taken and placed in separate 45 mL Teflon® liners, which were then inserted into stainless steel Parr acid digestion bombs and put in the oven at 140°C for one week. The Parr bombs were then taken out of the oven and allowed to cool overnight at room temperature. The suspension was vacuum filtered through

0.45-µm Millipore membranes, rinsed three times with boiling DIW, covered and dried overnight at 30°C. Solids were crushed with a mortar and pestle and sieved (sieve number 100) to an approximate 150 µm particle size.

2.1.2. Synthesis of Na autunite: $Na[(UO_2)(PO_4)]\cdot 1.5H_2O$ (c). Microcrystalline sodium autunite was synthesized according to the method of Zheng et al. [14]. Stoichiometric volumes of 0.05 M H_3PO_4 and 0.1 M $UO_2(NO_3)_2\cdot 6H_2O$ were mixed in a jacketed reaction vessel under N_2 at 70°C. Standardized 0.1 M NaOH was added dropwise to the stirred suspension and the pH was adjusted to approximately 5. The suspension was stirred overnight at 70°C, and subsequently allowed to settle. The supernatant was decanted and replaced with degassed 18 MΩ DIW at 70°C (twice), stirred and allowed to settle. The final pH was ca. 7. The final suspension was extracted and vacuum filtered through 0.45-µm Millipore membranes, rinsed three times with boiling DIW, covered and dried overnight at 30°C. Solids were crushed with a mortar and pestle and sieved (sieve number 100) to an approximate 150 µm particle size. The resulting powder was placed in 20 mL borosilicate centrifuge vials and stored.

2.1.3. Synthesis of chernikovite: $H_3O[(UO_2)(PO_4)]\cdot 4H_2O$ (c). Microcrystalline chernikovite was synthesized in a manner very similar to that of TDT. However the uranyl nitrate and phosphoric acid solutions were mixed in 1:1 ratios; and the chernikovite supernatant did not undergo repeated rinsing with DIW. In addition, instead of undergoing hydrothermal reaction, the suspension of chernikovite was placed in a 125 mL polypropylene bottle, sealed and stored in the dark and allowed to age for approximately four months.

2.2. Elemental Analysis

For all of the synthetic phases in this study, duplicate solid samples of roughly 10 mg were digested in concentrated nitric acid and diluted to 100 mL in a volumetric flask with boiled 18 MΩ water. These duplicate digest samples were subsequently analyzed for dissolved metal ion content with a Perkin-Elmer Optima 3200 axial torch ion-coupled optical emission spectrometer (ICP-OES) with a precision of approximately 5%. For all samples, three replicate intensities were recorded from which the average and standard deviation was calculated (table 9).

2.3. Thermogravimetric Analyses (TGA)

To quantify the degree of hydration in the uranyl phosphates studied herein, TGA experiments were conducted using a Perkin-Elmer TGA-7 instrument. The TGA was calibrated with a 10 mg standard weight furnished by Perkin-Elmer. Powdered samples of approximately 10 mg were analyzed inside a platinum pan. In all cases, the scan rate was 10^{o}C/min and the experimental temperature ranged from 25^{o}C to 500^{o}C. A minimum of three replicate runs were conducted for each uranyl phosphate as described below. In every case excellent agreement was observed between replicate runs resulting in an experimental uncertainty of less than 1%.

2.4. Powder x-ray diffraction (PXRD)

Well-rinsed filtrates of the suspensions (~ 150 μm particle size) were prepared for PXRD analysis at room temperature using a Siemens Kristalloflex D500 diffractometer with the following parameters: Copper source (Kα; 1.5406 Å); 35 keV, 30 mA, Kβ filter: Ni; scintillation

counter detector; Continuous mode: 0.02d/min; 2θ range: 5-55. The diffractograms were produced using supporting MDI Data Scan 4 and Jade 8 software packages.

2.5. ATR-IR Spectrometry

Measurements were made on solids in this study using a Nicolet 6700 FT-IR spectrometer with an ATR accessory equipped with a ThermoElectron Smart Nexus Orbit single-reflection diamond IRE. Spectra were measured between 4000 and 400 cm^{-1} at 8 cm^{-1} resolution. A total of 200 scans were averaged for each sample and background. The system was purged with desiccated N_2 at 30 psi. As noted above, the solid samples were ground with an agate mortar and pestle and sieved to an approximate 150 µm particle size.

3. Results and Discussion

3.1. Elemental Analysis (ICP-OES and TGA)

The results of chemical digestion of duplicate samples of sodium autunite ($Na[(UO_2)(PO_4)]\cdot 1.5H_2O$), chernikovite ($H_3O[(UO_2)(PO_4)\cdot 4H_2O$) and TDT ($((UO_2)_3(PO_4)_2\cdot 4H_2O$) are shown in table 9. The concentrations of the dissolved analytes shown in table 9 are consistent with the expected stoichiometry of the solids of interest.

Table 9. Chemical digestion data for the solids in this study. In descending order: Na autunite, chernikovite and TDT. Water content was determined by taking the average and standard deviation of triplicate (for chernikovite and TDT) and quadruplicate (Na autunite) TGA runs.

Na autunite	**Concentration (M)**	**1 σ**	**Molar Ratio**
UO_2^{2+}	$3.70 \cdot 10^{-4}$	$1.73 \cdot 10^{-5}$	1.00
PO_4^{3-}	$3.58 \cdot 10^{-4}$	$5.73 \cdot 10^{-6}$	1.03
H_2O	$5.62 \cdot 10^{-4}$	$2.36 \cdot 10^{-6}$	1.52
Chernikovite	**Concentration (M)**	**1 σ**	**Molar Ratio**
UO_2^{2+}	$5.00 \cdot 10^{-4}$	$6.47 \cdot 10^{-5}$	1.05
PO_4^{3-}	$4.27 \cdot 10^{-4}$	$1.40 \cdot 10^{-5}$	1.00
H_2O	$1.76 \cdot 10^{-3}$	$4.05 \cdot 10^{-6}$	4.12
TDT	**Concentration (M)**	**1 σ**	**Molar Ratio**
UO_2^{2+}	$3.17 \cdot 10^{-4}$	$2.88 \cdot 10^{-8}$	2.98
PO_4^{3-}	$2.13 \cdot 10^{-4}$	$2.33 \cdot 10^{-6}$	2.00
H_2O	$4.47 \cdot 10^{-4}$	$1.08 \cdot 10^{-6}$	4.20

The molar proportions of water for each of these phases was determined via TGA; and the temperature profiles of Na autunite, chernikovite and TDT are shown in figure 11. Plateau regions observed at the highest temperature indicate that all water has been expelled from the solids. In all cases, excellent agreement was observed between triplicate TGA runs (< 1% uncertainty), except for Na autunite. In this case, replicate runs yielded > 1% uncertainty so the average and standard deviation was taken of four TGA analyses to yield a relative standard deviation of 0.42%.

Gradual water loss is observed in both Na autunite and chernikovite at relatively low temperature, while the TDT temperature profile features a plateau from 25°C to ca. 83°C. This suggests that a smaller weight percentage of physisorbed water is associated with TDT relative to Na autunite and chernikovite. Chernikovite undergoes the most sizeable dehydration in terms of weight percent, losing most of its water by 125°C; however the sharpest event occurs between ca. 40 to 75°C. Interestingly, both Na autunite and TDT feature the most significant dehydration events at roughly the same temperature, ending at ca. 125°C. In addition, the TDT profile exhibits a dehydration event at ca. 240°C that is not evident in either Na autunite or chernikovite.

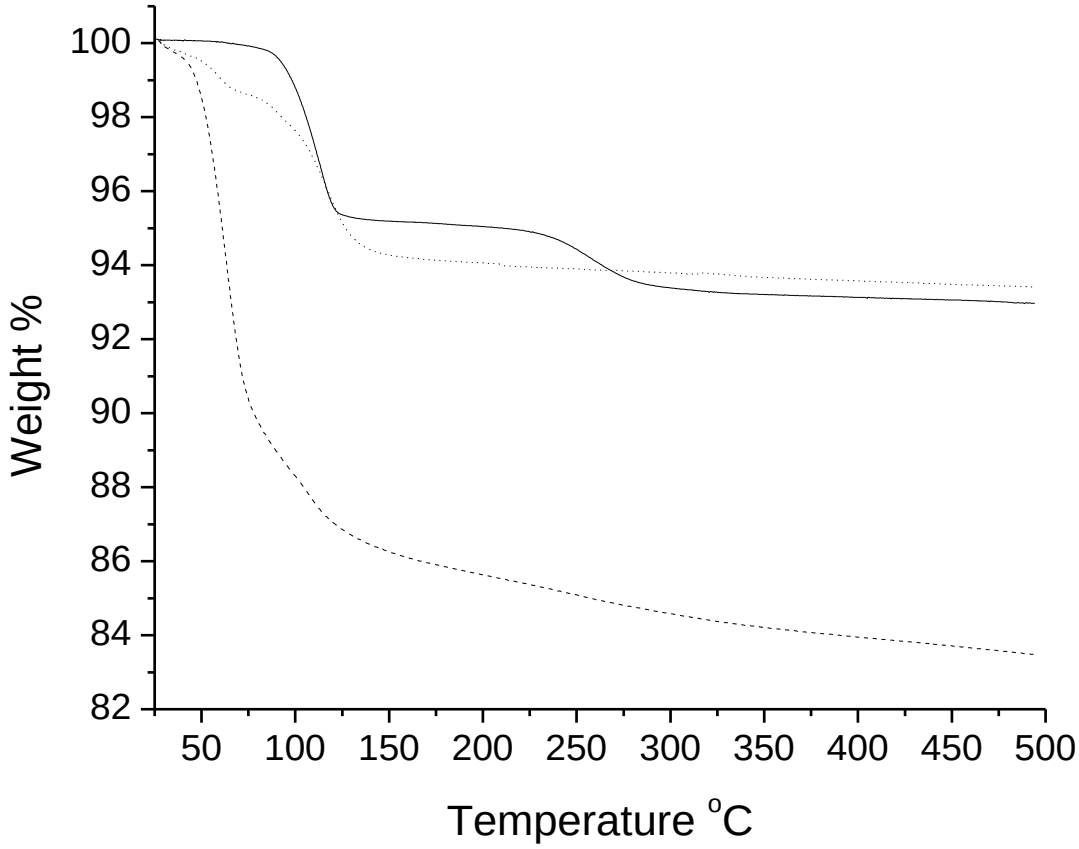

Figure 11. TGA temperature profiles of Na autunite (dotted line), chernikovite (dashed line) and TDT (solid line). These thermograms represent the average of quadruplicate TGA runs in the case of Na autunite and triplicate runs for chernikovite and TDT. All runs were conducted from 25°C to 500°C at 10°C/min.

3.2. PXRD analysis

Samples of Na autunite, chernikovite and TDT were analyzed by PXRD and compared to published powder diffraction files (PDFs). In the case of Na autunite, separate powders were analyzed by PXRD to determine the effect of hydrothermal treatment. The first consisted of a sample prepared as outlined above. The second sample was placed in a Parr bomb and heated at

140^{o}C for three days. Both of these XRD patterns are shown in figure 12 together with PDF# 29-1284 for synthetic Na autunite. With the exception of increased intensity in the hydrothermally treated Na autunite sample, which is indicative of an increase in crystallinity, very good agreement between the two samples is observed. In general, the XRD patterns for synthetic sodium autunite are consistent with the published XRD PDF# 29-1284. However, some discrepancies are noteworthy. First, as noted above, differences in hydration can result in shifts in the XRD patterns of hydrated uranyl compounds. A slight shift to higher 2-theta is noticeable in the synthetic Na autunite relative to PDF# 29-1284 (figure 12). This is expected since lower degrees of hydration can cause shifts to higher 2-theta locations. The PDF #29-1284 is for a trihydrate sodium autunite whereas the sample in this study contains 1.5 moles of water as determined by TGA (table 9). Second, there are two peaks at 2-theta of ca. 19.5 and 32.5 in the synthetic Na autunite from this study that are not present in the PDF# 29-1284. However, both of these peaks are present in the PDF for synthetic chernikovite (PDF# 08-0296, not shown). Although this suggests that this Na autunite may have some hydronium in the interlayer, i.e., a small chernikovite contribution, no evidence of H_3O^+ in Na autunite is observed with IR spectroscopy, as discussed in the following section.

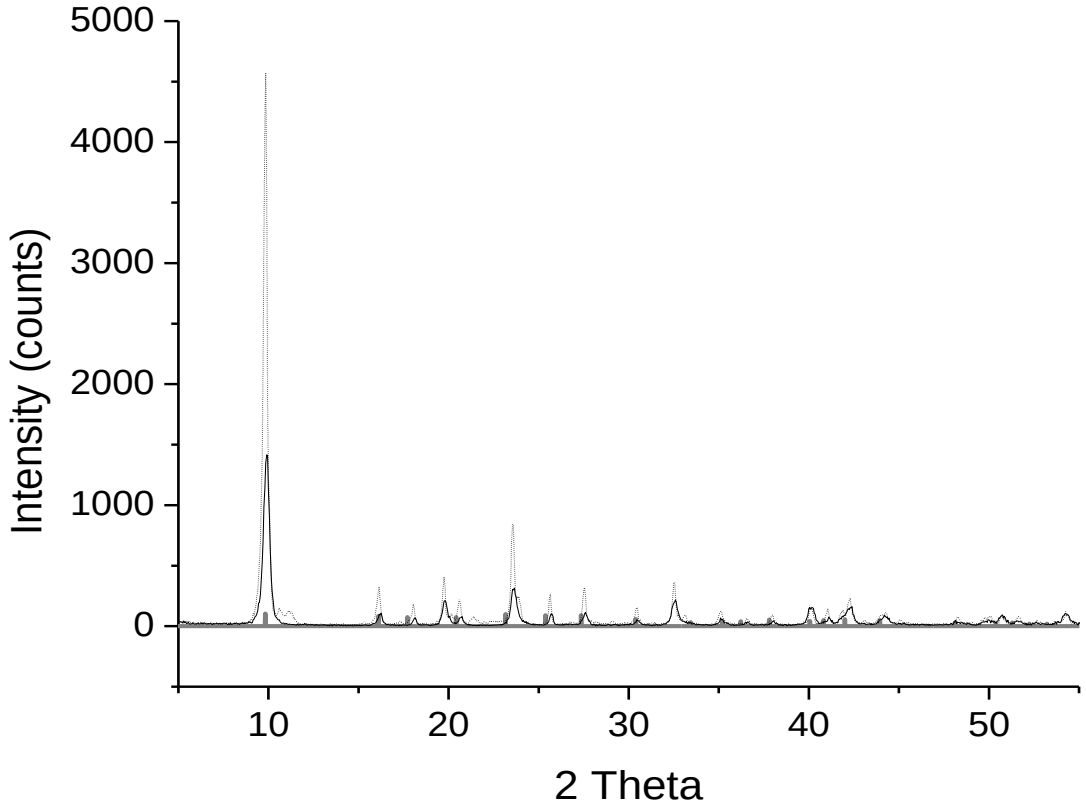

Figure 12. Powder XRD diffractograms of Na autunite synthesized by the author (black diffractogram), placed in a Parr bomb at 140^{o}C for three days (dotted line) and PDF # 29-1284 (grey lines).

Synthetic chernikovite prepared in our laboratory is in very good agreement with PDF# 29-0670 for synthetic chernikovite as shown in figure 13. However, four relatively weak peaks are present in our synthethic sample that are not ostensible in PDF# 29-0670, at ca. 19.5, 32.9, 36.0, and 52.0 2-theta degrees. However, these reflections are present in another published XRD pattern of synthetic chernikovite, PDF#08-0296 (not shown). Thus only one weak peak (at ca. 29.15) is not associated with published patterns of synthetic chernikovite. The reason for the location of this peak is unclear; however this reflection is present, albeit very faintly, in the hydrothermally treated Na autunite sample. Clearly these small differences in the PDF files of

chernikovite and Na autunite render the selection of a particular PDF for identifying chernikovite rather arbitrary.

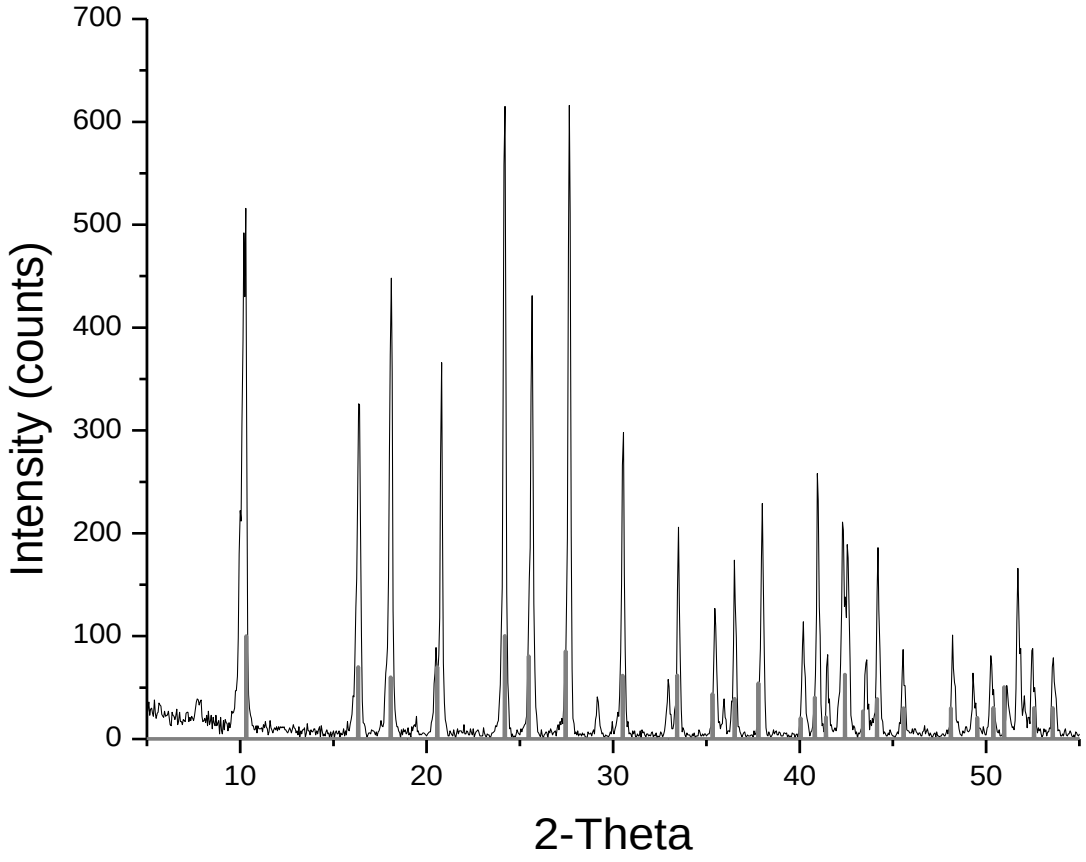

Figure 13. Powder XRD diffractograms of the well-aged chernikovite synthesized by the author (most intense diffractogram in black) and the published PDF # 29-0670 (grey lines) for synthetic chernikovite.

Figure 14 shows the PXRD pattern of TDT synthesized in this study. The most prominent band in the TDT diffractogram appears at 2θ ca. 21^{o} and a d-spacing of 4.2 Å. The

powder diffraction data were compared to PDF card 37-0369 and very good agreement was observed and no extraneous peaks are notable.

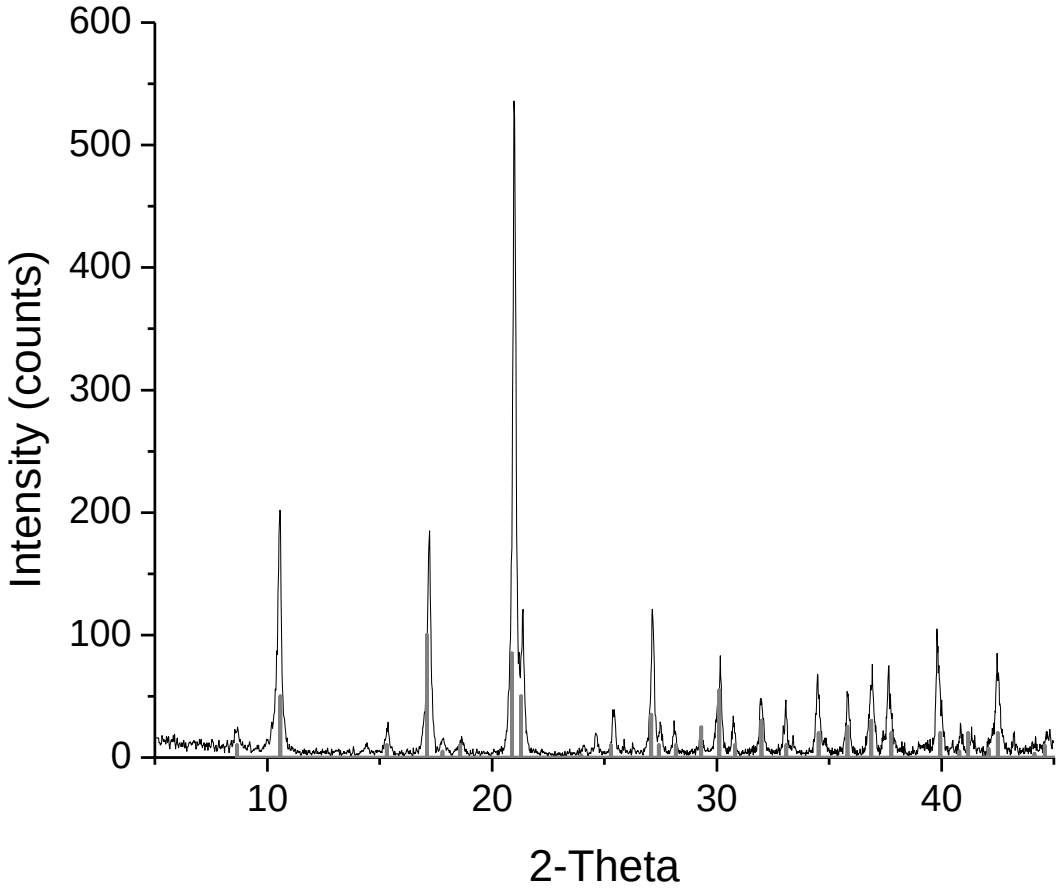

Figure 14. Powder XRD diffractogram of TDT and published XRD pattern of TDT, PDF# 37-0369 (grey lines).

3.3. ATR-IR analysis

ATR-IR was performed on Na autunite, chernikovite and TDT. The band assignments of the various components presented herein are in line with published studies of Na autunite [12], chernikovite [4, 12] and TDT [4]. The IR spectra and corresponding band assignments for these materials are shown in figure 15 and table 10 respectively.

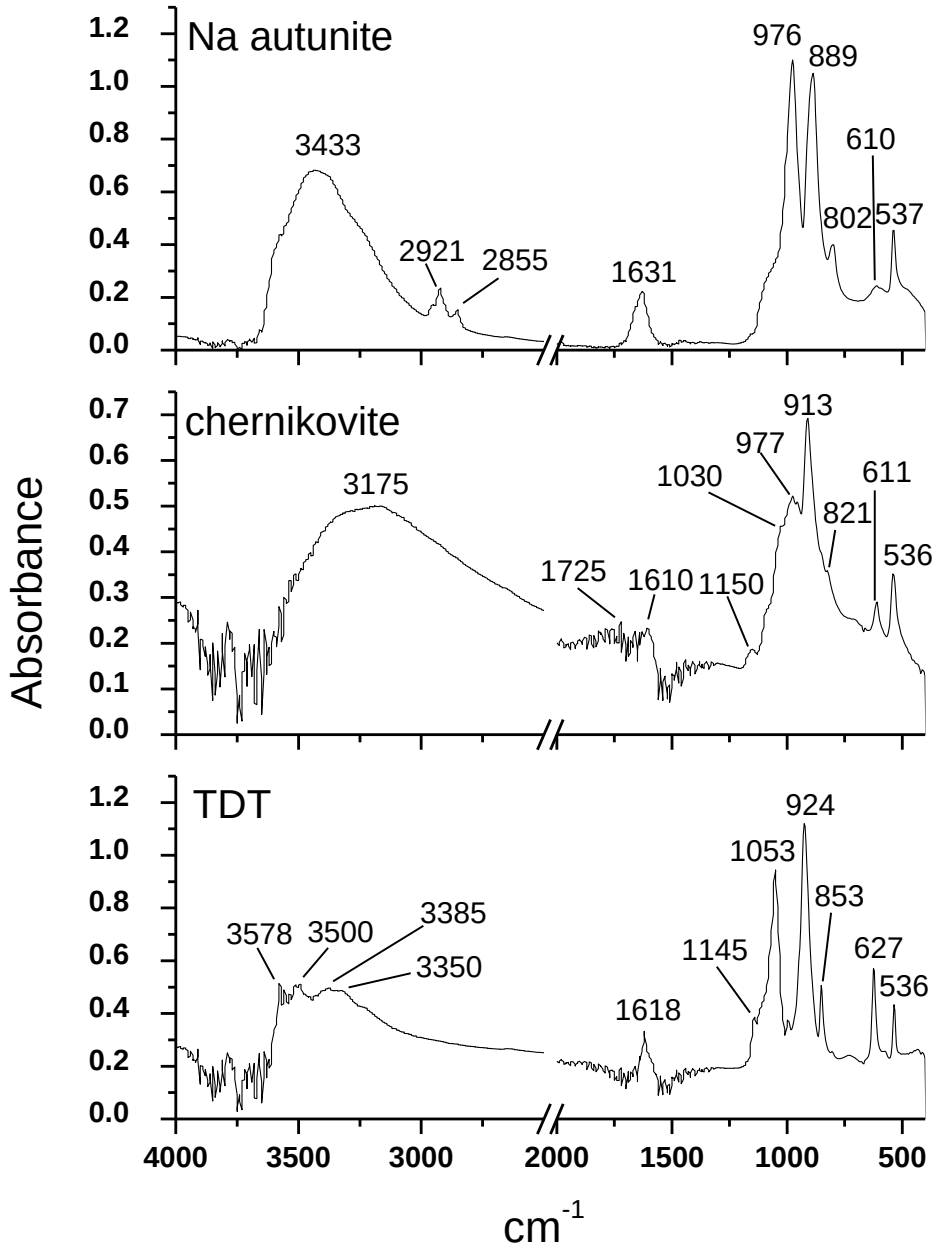

Figure 15. ATR-IR spectra of Na autunite: $Na[(UO_2)(PO_4)]\bullet 1.5H_2O$ (top), chernikovite $(H_3O[(UO_2)(PO_4)]\bullet 4H_2O$ (middle) and TDT: $(UO_2)_3(PO_4)_2\bullet 4H_2O$ (bottom) showing structural evidence of distinct phases. No spectral features were observed in the region between ca. 2500 cm^{-1} and 2000 cm^{-1}; therefore part of this region was omitted for clarity.

Table 10. Band assignments (in cm^{-1}) for Na autunite, chernikovite and TDT. The corresponding spectra are displayed in figure 15.

Na autunite	Chernikovite	TDT	Group	Vibrational Mode
537	536	536	PO_4^{3-}	Bend; ν4
610	611	627	PO_4^{3-}	Bend; ν4
802	821	853	UO_2^{2+}	Sym. stretch; ν1
889	913	924	UO_2^{2+}	Antisym. stretch; ν3
976	977	1053	PO_4^{3-}	Antisym. stretch; ν3
	1030		H_3O^+	Bend; ν2
	1150	1145	H_2O	Librational
	1610	1618	H_2O	Bend; ν2
1631			H_2O	Bend; ν2
	1725		H_3O^+	Bend; ν4
2855			Na-OH	Antisym. stretch; ν1/ν3
2921			Na-OH	Antisym. stretch; ν1/ν3
	3175		H_3O^+/OH	Stretch
3433		3350	OH	Antisym. stretch; ν1/ν3
		3385	OH	Antisym. stretch; ν1/ν3
		3500	OH	Antisym. stretch; ν1/ν3
		3578	OH	Antisym. stretch; ν3

The broad, rather featureless band from ca. 3600 – 3000 cm^{-1} observed in all three solids is a combination of many overlapping H-O-H antisymmetric and symmetric stretching vibrations which is strong evidence of significant H-bonding and multiple H_2O bonding environments in these phases. This arises from structurally nonequivalent water groups in the given unit cell [12]. In addition to these broad OH stretching vibrational modes in TDT, four relatively sharp v3/v1 OH modes at 3578, 3500, 3385 and 3350 cm^{-1} provide further insight into the structure of TDT (figure 15, bottom panel). In contrast to Na autunite and chernikovite, TDT comprises an interlayer uranyl ion resulting in an open framework structure [18] that has a significant effect on the location and bonding environment of the interlayer water molecules. In agreement with Locock and Burns [15], we hypothesize that this open framework structure results in distinct water populations that are occluded, filling the available space predominantly through hydrogen bonding to the neighboring polyhedra in the interlayer and in the "sheet". These distinct, mutually isolated, water molecules produce relatively sharp OH stretching modes compared to those observed in Na autunite and chernikovite.

The chernikovite spectrum (figure 15; middle panel) shows ample evidence of the interlayer hydroxonium ion which affords the most important evidence in distinguishing chernikovite from Na autunite. First, the broad v1 and v3 stretching modes of H_3O^+ are expected at a lower energy than their H_2O counterparts [12]. These H_3O^+ stretching modes are typically featured at ca. 2500-3500 cm^{-1}, while the corresponding modes for H_2O are observed at ca. 3200-3600 cm^{-1}. Thus, the broad band starting at ca. 2500 cm^{-1} and centered at ca. 3175 cm^{-1} observed in chernikovite is likely the result of overlapping v1 and v3 bands of H_3O^+ and H_2O. In contrast, the Na autunite and TDT OH stretching modes appear at significantly higher wavenumbers (figure 15). Second, and perhaps most conspicuously, the band at ca. 1725 cm^{-1}

for chernikovite is most likely the v4 bending mode of H_3O^+. Overlap with the v2 bending mode of H_2O centered at 1610 cm^{-1} results in a diminution of band intensity for both the H_3O^+ and H_2O bending modes. Without H_3O^+, the H_2O bending mode is typically relatively sharp and symmetric as shown in the TDT and the Na autunite spectra (at 1618 cm^{-1} and 1631 cm^{-1} respectively). Third, the weak band at ca. 1030 cm^{-1} for chernikovite is attributed to the v2 bending mode of H_3O^+. This vibrational mode is difficult to observe in hydrated uranyl phosphates [12, 16] since the relatively intense v3 PO_4 mode tends to mask the v2 bending mode of H_3O. However, in this sample of chernikovite, the significantly weakened v3 PO_4 mode centered at 977 cm^{-1} is evidence of significant band overlap between these two modes. Spectral evidence of H_3O^+ is therefore a very effective way to delineate chernikovite from other autunites, since the other non-chernikovite phases exhibit a much sharper v3 PO_4 band at ca. 977 cm^{-1} when H_3O^+ is not present (see the Na autunite spectrum in figure 15).

The ATR-IR spectrum of the hydrothermally treated Na autunite sample is shown in figure 5 (top panel). In addition, the band assignments for this phase are shown in table 10. Clearly the most prominent diagnostic features are evidenced in the appearance of relatively sharp bands at 2921 cm^{-1} (with a shoulder at 2955 cm^{-1}) and at 2855 cm^{-1} in the Na autunite spectrum. These features are lower energy vibrational modes than would be expected for typical water stretching vibrations in these solids; and they are attributed to the Na-OH (νOH) stretching mode. The Na-OH bond necessarily shifts the electron density of the oxygen donor resulting in a weakening of the νOH relative to that of H_2O. The sharpness of these bands compared to typical OH stretching modes provides strong evidence that the Na ion is occupying very specific sites in the interstitial region of the unit cell.

It has been shown that the sodium ion has a significant effect on the vibrational frequencies of vicinal groups to which it is bonded, mainly via coordinated water, (e.g., UO_2^{2+})

in the unit cell of a uranyl compound. For example, in studies of clarkeite: $Na[(UO_2)O(OH)]xH_2O$ [17, 18], IR data clearly showed a decrease in the $\nu 3UO_2$ frequency with increasing stoichiometric Na. In fact, other workers that studied synthetic clarkeite [19, 20, 21] were able to roughly predict the amount of Na in the solid based upon the red-shift of $\nu 3$ UO_2. In agreement with Baran et al., we also observed a shift to slightly lower $\nu 3$ UO_2 frequency in the sodium autunite relative to that of chernikovite and TDT. Thus it appears that an interaction between the interlayer Na and the structural uranyl is occurring. Accordingly, we propose that the bands at 2920 cm^{-1} and 2854 cm^{-1} are νOH due to bridging between the Na^+ and UO_2^{2+} moieties. Likely the interstitial Na-OH is hydrogen bonded to oxygen in the uranyl square bipyramid. This bonding scheme accounts for both the presence of Na-OH (νOH) and the reduced energy in the UO_2^{2+} antisymmetric stretch mode in synthetic sodium autunite.

4. Conclusions

For experimental investigations (solubility, sorption, etc) of hydrated uranyl compounds adequate characterization of the solid is vital. The findings presented herein suggest that this must include, at minimum, elemental analysis, PXRD, IR spectroscopy and TGA.

For relatively rapid solid phase identification, PXRD is a useful analytical tool. In addition, PXRD can be used to qualitatively observe degrees of hydration in uranyl compounds. However, delineating isostructural compounds presents a significant challenge, particularly for those containing U, since U tends to dominate the XRD pattern. On the other hand, ATR-IR is a very useful tool in delineating isostructural uranyl compounds since local bonding environments, i.e., interlayer metal occupancies can be readily elucidated. However, ATR-IR is a surface technique; and at times it can be difficult to delineate physisorbed water from stoichiometric

water in hygroscopic materials. Hence, the complementary use of both PXRD and ATR-IR is necessary, in addition to elemental analyses, to effectively characterize and delineate hydrated uranyl minerals and synthetic compounds.

In this report, we showed that variations in hydration have a significant effect on the patterns observed with powder XRD. We also showed that both isostructural hydrated uranyl phosphates (i.e., the autunites) and structurally distinct phases (i.e., TDT) exhibit very similar XRD patterns.

With ATR-IR, we showed that specific bonding environments (e.g., Na-OH), and components (e.g., H_3O^+) can be readily elucidated affording a more reliable delineation of isostructural Na autunite and chernikovite, respectively. In addition, PXRD and ATR-IR data were compared in delineating chernikovite and TDT – two phases that can be easily confused in the synthesis process, i.e., one phase can precipitate when the other is intended. Structural characteristics unique to each phase were exploited with ATR-IR.

Acknowledgements

This work was supported primarily by the U.S. Department of Energy, Basic Energy Sciences, Heavy Element Chemistry program, contract DE-FG02-06ER15782. In addition, SBC and CRA gratefully acknowledge support from the Joint Domestic Nuclear Detection Office-National Science Foundation: Academic Research Initiative (ARI), contract number ECCS-0833548 during the preparation of this manuscript.

References

[1] Burns P C 1999 *Reviews in Mineralogy Vol. 38* Ed P C Burns and R Finch (Mineralogical Society of America) 23-86.

[2] Gorman-Lewis D J, Burns P C and Fein J B 2008 *J. Chem. Thermodyn*. **40** 335-52.

[3] Hill F C 1999 *Reviews in Mineralogy Vol. 38* Ed P C Burns and R Finch (Mineralogical Society of America) 653-73.

[4] Pham-Thi M and Colomban P 1985 *J. Less-Common Met*. **108** 189-216.

[4] Thomas A, Dacheux N, Le Coustumer P, Brandel V and Genet M 2001 *J. Nucl. Mater*. **295** 249-64.

[6] Felmy A R, Xia, Y and Wang Z 2005 *Radiochim. Acta* **93** 401-08.

[7] Rai B D, Xia Y, Rao L, Hess N J, Felmy A R, Moore D A and McCready D E 2005 *J. Sol. Chem.* **34** 469-98.

[8] Suzuki Y, Sato T, Isobe H, Kogure T and Murakami T 2005 *Amer. Mineral*. **90** 1308-14.

[9] Wellman D M 2004 *Environmental availability of uranium from secondary uranyl minerals.* (PhD dissertation, Washington State University; Pullman WA, USA).

[10] Sowder A G 1998 *The formation, transformation, and stability of environmentally relevant uranyl mineral phases*. (PhD dissertation, Clemson University; Clemson SC, USA).

[11] Hofmeister A M, Keppel E, Bowey J E and Speck A K 2000 *Europ. Space Agengy. Special Pub.* **456** 343-46.

[12] Cejka J 1999 *Reviews in Mineralogy Vol. 38* Ed P C Burns and R Finch (Mineralogical Society of America) 521-622.

[13] Griffiths P R and de Haseth J A 2007 *Fourier Transform Infrared Spectrometry* (New York; John Wiley & Sons, Inc) 529 pp.

[14] Zheng Z, Wan J, Song X and Tetsu T K 2006 *Coll. Surfaces.* **274** 48-55.

[15] Locock A J and Burns P C 2002 *J. Sol. State Chem*. 1**63** 275-80.

[16] Rosiere J Thesis 1973 Universite des Sciences et Technologie du Languedoc (in French) 150 pp.

[17] Siderenko G A 1978 *Atom. Moscow.* 216 pp. (in Russian)

CHAPTER FOUR

The Hydrothermal Transformation of Chernikovite into Triuranyl Diphosphate Tetrahydrate (TDT)

Christopher R. Armstrong and Sue B. Clark[1]

Department of Chemistry, Washington State University, Pullman, WA 99164 U.S.A.

E-mail: s_clark@wsu.edu

Abstract. Isostructural hydrated uranyl phosphates, and in particular those that comprise the autunite mineral family, have been routinely synthesized by manipulating the metal occupancies in the interstitial region of the compound of interest, while leaving the chemical properties of the sheet structures intact. Hence, no alteration is intended in the structural unit as the result of these interlayer ion-exchange processes. However significant, and in some cases inadvertent, structural changes can occur, particularly when the synthesis conditions (e.g., temperature and pressure) are altered. In this report we demonstrate the efficacy of using powder x-ray diffraction (PXRD) and attenuated total reflection infrared (ATR-IR) spectrometry in monitoring the structural transformation of chernikovite into triuranyl diphosphate tetrahydrate (TDT). We show that a significant structural change occurs as the result of hydrothermal treatment of well-aged synthetic chernikovite. We demonstrate that vertex-sharing, square uranyl bipyramids convert to edge-sharing pentagonal bipyramids suggesting that, under elevated temperature and pressure conditions, the latter structural conformation is more stable. These results underscore

[1] Corresponding author: Tel: 01-509-335-1411; fax: 01-509-335-8867. E-mail: s_clark@wsu.edu

the importance of rigorously characterizing synthetic uranyl compounds before and after hydrothermal treatment; since neglecting to do so can result in highly erroneous experimental (solubility, sorption etc) interpretations.

1. INTRODUCTION

Hydrated uranyl phosphates belonging to the autunite mineral family are common in nature, particularly in uraniferous alkali igneous rocks containing accessory apatites (Langmuir, 1978). These autunites typically form as the result of chemical weathering (i.e., macroscale dissolution of bulk rock matrices), oxidation of U^{4+} to UO_2^{2+} and subsequent uranyl phosphate precipitation throughout a wide pH range. Due to their relatively low solubility, autunites are the most common uranium minerals in arid, oxidizing regions (Nininger, 1954).

In addition to the ubiquity of naturally-occurring autunites, these phases are also commonly formed by anthropogenic means. At the Hanford site in WA, between 1944 and 1951 roughly 5000 short tons of uranium were recovered from bismuth phosphate processing wastes. These materials were neutralized, subsequently precipitated as predominantly Na autunite [$Na(UO_2)(PO_4)•xH_2O$], and held in underground storage tanks (Felmy et al., 2005). However it has been since discovered that these suspensions have leaked from the storage tanks into the surrounding subsurface (Womack et al., 1971) and the chemistry of these solids is not well understood. As such, fundamental experimental studies, i.e., structural, thermodynamic, are required of these solid-solution systems thus affording insights into the environmental fate U in groundwater systems where these anthropogenic processes have taken place.

Owing to their isostructural properties, a variety of end member autunites have been synthesized from one starting material, namely chernikovite: $H_3O(UO_2)(PO_4)•xH_2O$. Van Haverbeke et al. (1996) prepared meta-ankoleite [$K(UO_2)(PO_4)•3H_2O$] via ion exchange between hydronium and potassium by refluxing synthetic chernikovite several times in a 1M KCl solution. In a similar manner, Vochten (1990) reported the transformation of both chernikovite and sodium autunite [$Na(UO_2)(PO_4)•8H_2O$] into lehnerite [$Mn(UO_2)_2(PO_4)_2•8H_2O$]. In fact, Vochten et al. reported a series of ion-exchange syntheses involving uranyl phosphates and the

chemically analogous uranyl arsenates by using chernikovite (and the chemically analogous arsenate) as the starting material in the preparation of meta-zeunerite [$Cu(UO_2)_2(AsO_4)_2 \cdot 8H_2O$] (Vochten and Goeminne, 1984), meta-kirchheimerite [$Co(UO_2)_2(AsO_4)_2 \cdot 8H2O$] (Vochten and Goehminne, 1984), bassetite [$Fe(UO_2)_2(PO_4)_2 \cdot 8H_2O$] (Vochten et al., 1984) and kahlerite [$Fe(UO_2)_2(AsO_4)_2 \cdot 12H_2O$].

All of the aforementioned studies involved the manipulation of the interlayer by the simple exchange of interstitial metals. No structural transformation was reported and in many of these studies it is not clear whether the sample was monitored for structural changes during hydrothermal reaction, i.e., reacting the suspension in a Parr bomb at elevated temperature.

In this contribution we present data using a variety of analytical techniques including attenuated total reflection infrared (ATR-IR) spectrometry, powder x-ray diffraction (PXRD), and thermogravimetric analysis (TGA). We demonstrate that a fundamental reorganization of the chernikovite unit cell takes place, resulting in the structurally distinct triuranyl diphosphate tetrahydrate (TDT) due to hydrothermal reaction. These findings suggest that hydrothermal treatment may not only increase the crystallinity of uranyl compounds, but also may result in significant structural modifications. As such, these findings convey the importance of properly characterizing these uranyl compounds before and after hydrothermal treatment to monitor structural changes, something that has not been done sufficiently in the past. Such structural conversions may be a previously unconsidered source of error in solubility studies of uranyl compounds.

2. EXPERIMENTAL MATERIALS AND METHODS

2.1. Chemicals

All chemicals are reagent grade or higher. Doubly deionized 18MΩ and boiled water (DDI) was used in preparations of all solutions. Standards used for ICP-OES analyses were 99.9% purity.

2.2. Synthetic and natural compounds

The pH was measured with a ThermoElectron Corp. Orion 4 Star pH meter equipped with a Ross combination pH electrode (Orion Model 8102). Prior to each use, the pH electrode was calibrated with NIST standards. For hydrothermal reactions, 23- and 45-mL Teflon® liners were placed inside stainless steel Parr acid digestion bombs.

2.2.1. Synthetic chernikovite: $H_3O[(UO_2)(PO_4)]\cdot 2.5H_2O$ (c)

Microcrystalline chernikovite was synthesized by mixing stoichiometric volumes of 0.7 M H_3PO_4 and 0.05 M $UO_2(NO_3)_2\cdot 6H_2O$ in a jacketed reaction vessel under N_2 atmosphere at 40°C (± 0.1). The suspension was stirred overnight at 40°C and subsequently allowed to settle at 40°C. The settled suspension was subsequently mixed and the suspension (chernikovite and its mother liquor) was placed in a 125 mL polypropylene bottle, sealed and stored in the dark and allowed to age for 4 months. The mixed suspension was then vacuum- filtered through 0.45-µm Millipore membranes, rinsed three times with boiling DIW, covered and dried overnight at 30°C. Solids were crushed with a mortar and pestle and sieved (sieve number 100) to an approximate 150 µm particle size.

2.3. Elemental Analysis

For all of the solid phases in this study, duplicate solid samples of roughly 10 mg were digested in concentrated nitric acid and diluted to 100 mL in a volumetric flask with boiled 18MΩ water. These duplicate digest samples were subsequently analyzed for dissolved metal content with a Perkin-Elmer Optima 3200 axial torch ion-coupled optical emission spectrometer (ICP-OES) with a precision of approximately 5%. For all samples, three replicate intensities were recorded from which the average and standard deviation was calculated (Table 11).

Table 11. Analytes and corresponding wavelengths and ICP detection limits in this study.

Analyte	Emission line (nm)	Detection Limit (mg/L)	1σ
P	213.617	0.08	0.03
U	367.007	0.30	0.02

2.4. Thermogravimetric Analyses (TGA)

To quantify the degree of hydration in the uranyl phosphates studied herein, TGA experiments were conducted using a Perkin-Elmer TGA-7 instrument. The TGA was calibrated with a 10 mg standard weight furnished by Perkin-Elmer. Powdered samples of approximately 10 mg were analyzed inside a platinum pan. In all cases, the scan rate was 10^{o}C/min and the experimental temperature ranged from 25^{o}C to 500^{o}C. All of the uranyl phosphates were analyzed in triplicate; and in every case excellent agreement was observed between replicate runs resulting in an experimental uncertainty of less than 1%.

2.5. Powder x-ray diffraction (PXRD)

PXRD was performed on fine grained samples (~ 150 μm) at room temperature using a Siemens Kristalloflex D500 diffractometer with the following parameters: Copper source (Kα; 1.5406 Å); 35 keV, 30 mA, Kβ filter: Ni; scintillation counter detector; Continuous mode: 0.02d/min; 2θ range: 5-55. The diffractograms were produced using MDI Data Scan 4 and Jade 8 software packages.

2.6. ATR-IR Spectrometry

Measurements were made on solids in this study using a Nicolet 6700 FT-IR spectrometer with an ATR accessory equipped with a ThermoElectron Smart Nexus Orbit single-reflection diamond IRE. Spectra were measured between 4000 and 400 cm^{-1} at 8 cm^{-1} resolution. A total of 200 scans were averaged for each sample and background. The system was purged with desiccated N_2 at 30 psi. As noted above, the solid samples were ground with an agate mortar and pestle and sieved to an approximate 150 μm particle size.

3. RESULTS

3.1. Elemental Analysis (ICP-OES and TGA)

The results of chemical digestion of duplicate samples of chernikovite [$H_3O[(UO_2)(PO_4)\cdot 4\ H_2O$] and TDT [$(UO_2)_3(PO_4)_2\cdot 4H_2O$] are shown in Table 12. The concentrations of the dissolved analytes shown in Table 12 are consistent with the expected stoichiometry of the solids investigated given the experimental uncertainty associated with each analyte. Further characterization of these synthetic phases, including PXRD, ATR-IR and TGA, is discussed below.

Table 12. Chemical digestion data for well-aged chernikovite and chernikovite-derived TDT. Water content was determined by taking the average and standard deviation of triplicate TGA runs (Na autunite).

Chernikovite	**Concentration (M)**	**1 σ**	**Molar Ratio**
UO_2^{2+}	$4.98 \cdot 10^{-4}$	$3.19 \cdot 10^{-6}$	1.02
PO_4^{3-}	$4.89 \cdot 10^{-4}$	$5.99 \cdot 10^{-7}$	1.00
H_2O	$2.01 \cdot 10^{-3}$	$4.54 \cdot 10^{-6}$	4.12
TDT	**Concentration (M)**	**1 σ**	**Molar Ratio**
UO_2^{2+}	$3.14 \cdot 10^{-4}$	$1.26 \cdot 10^{-5}$	2.95
PO_4^{3-}	$2.13 \cdot 10^{-4}$	$3.07 \cdot 10^{-6}$	2.00
H_2O	$4.47 \cdot 10^{-4}$	$1.08 \cdot 10^{-6}$	4.20

As noted above, the molar proportions of H_2O for each of these phases was determined via TGA. Experiments were conducted from 25 – 500°C at a 10°C/min scan rate; and the temperature profiles of Na autunite, chernikovite and TDT are shown in Fig. 16. Plateau regions observed at the highest temperature indicates that all water has been expelled from the solids. In all cases, excellent agreement is observed between replicate TGA runs (< 1% uncertainty).

Gradual water loss is observed in chernikovite at relatively low temperature, while the TDT temperature profile features a plateau from 25°C to ca. 83°C. This suggests that a smaller weight percentage of physisorbed water is associated with TDT relative to chernikovite as this latter phase undergoes the most sizeable dehydration in terms of weight percent losing most of its water by 125°C; however the sharpest event occurs between ca. 40 to 75°C. In addition, the TDT profile exhibits a dehydration event at ca. 240°C that is not evident in chernikovite

suggesting that a more significant contribution of relatively tightly bound waters are associated with TDT. These waters are inferred to be coordinated to the interstitial uranyl ion in the TDT unit cell.

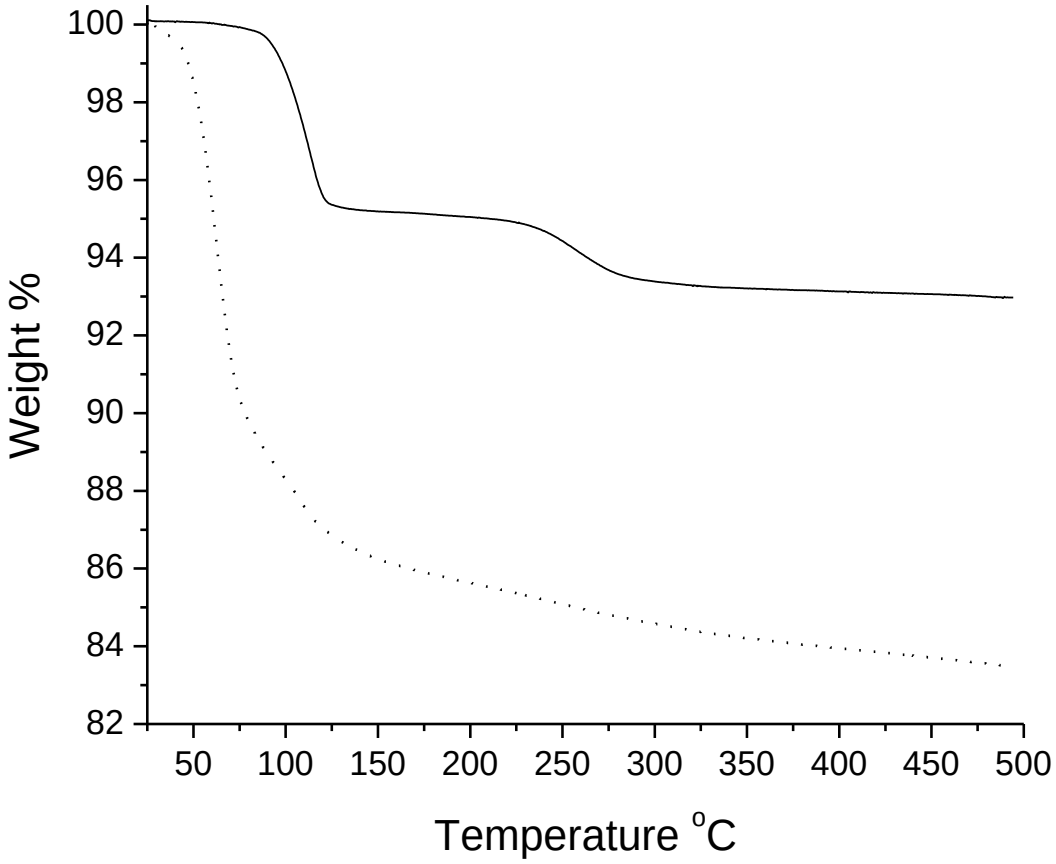

Fig. 16. TGA temperature profiles for chernikovite (dotted line) and TDT (solid line). These thermograms represent the average of triplicate runs for chernikovite and TDT. All runs were conducted from 25°C to 500°C at 10°C/min.

3.2. PXRD analysis

Synthetic chernikovite prepared in this laboratory is in very good agreement with PDF# 29-0670 as shown in Fig. 17. However, three relatively weak peaks are present in our synthethic sample that are not conspicuous in PDF# 29-0670 at ca. 19.5, 32.9 and 36.0 2-theta degrees. Interestingly, these peaks are present in another published XRD pattern of synthetic chernikovite, PDF#08-0296 (not shown). Thus only one weak peak (at ca. 29.15) is not associated with published patterns of synthetic chernikovite. The reason for the location of this peak is unclear and it could be the result of a minor impurity.

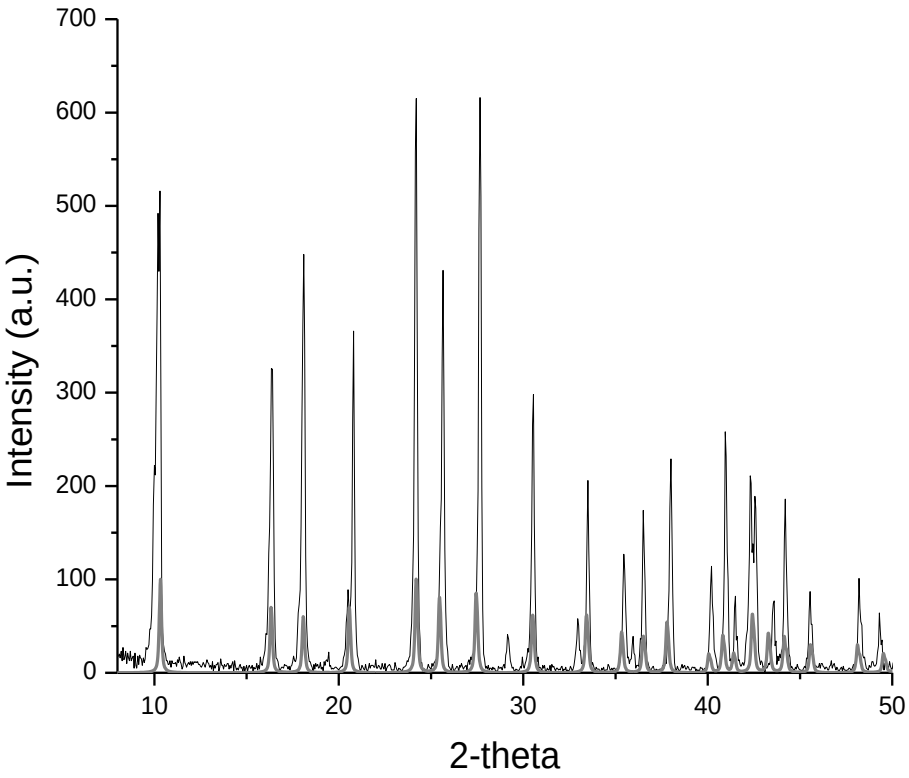

Fig. 17. Powder XRD diffractograms of the well-aged chernikovite synthesized by the author (most intense diffractogram in black) and the published PDF # 29-0670 (lower profile in grey) for synthetic chernikovite.

The XRD pattern of the chernikovite-derived TDT is shown in Fig. 18. Although PDFs cannot be directly compared to the PXRD pattern of TDT due to the latter's marked intensity, the tabulated 2-theta and d-spacing values of this TDT phase (not shown) are in very good agreement with PDF# 54-0773 and 37-0369 (Fig. 18). Note: the tabulated 2-theta and d-spacing values for all the synthetic phases in this study are available from the authors upon request. The marked intensity of the TDT suggests that it is highly crystalline; and it is clear that the transformation from chernikovite into TDT is complete. Considering the similarity of XRD patterns of hydrated uranyl phosphates, the difference between the well-aged chernikovite (Fig. 17) and the end-product TDT is rather striking.

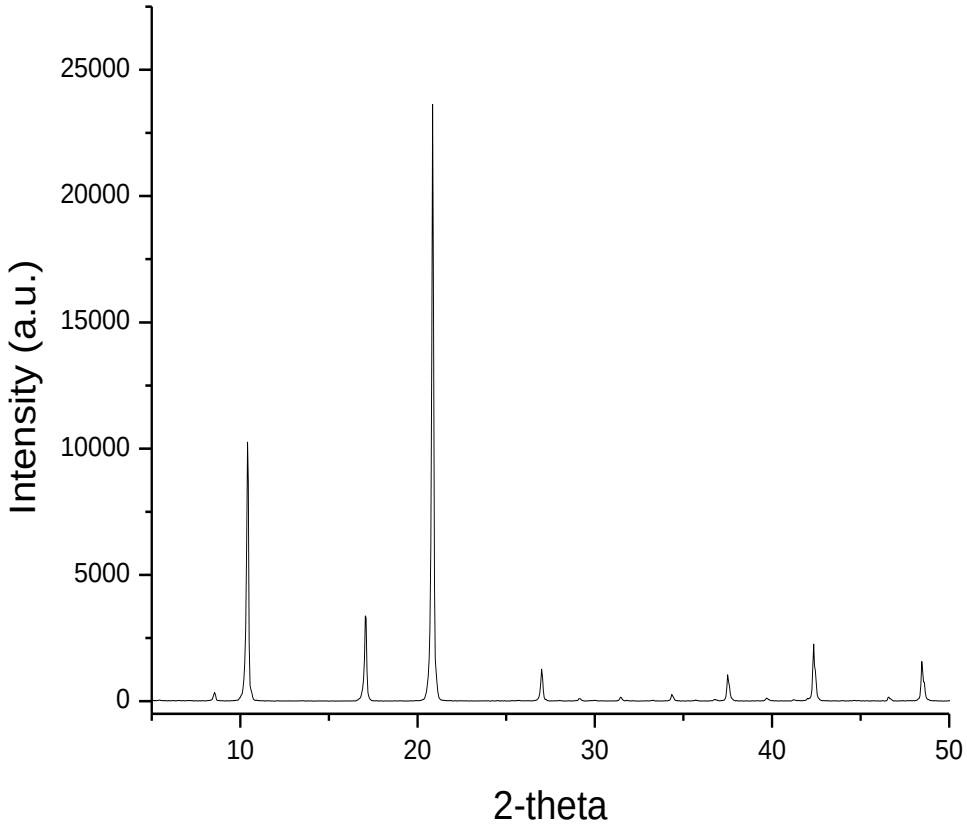

Fig. 18. Powder XRD diffractograms of TDT that was generated via hydrothermal reaction of well-aged synthetic chernikovite. Note the intensity of this XRD pattern.

3.3. ATR-IR analysis

ATR-IR was performed on chernikovite and chernikovite-derived TDT. The IR spectrum of chernikovite is shown in Fig. 19 (top panel) and the band assignments shown in Table 13 are in excellent agreement with published IR data of this phase (Pham –Thi and Columban, 1985; Cejka, 1999). Additionally, the IR spectrum of TDT shown in Fig. 19 (bottom panel) and the corresponding band assignments displayed in Table 14 are also consistent with Pham-Thi and

Columban (1985). Moreover, the IR data for this TDT phase (derived from chernikovite) is also in line with TDT synthesized by another method in a related study conducted in our laboratory (see Chapter One of this dissertation), thereby providing further evidence that complete conversion from chernikovite to TDT has taken place.

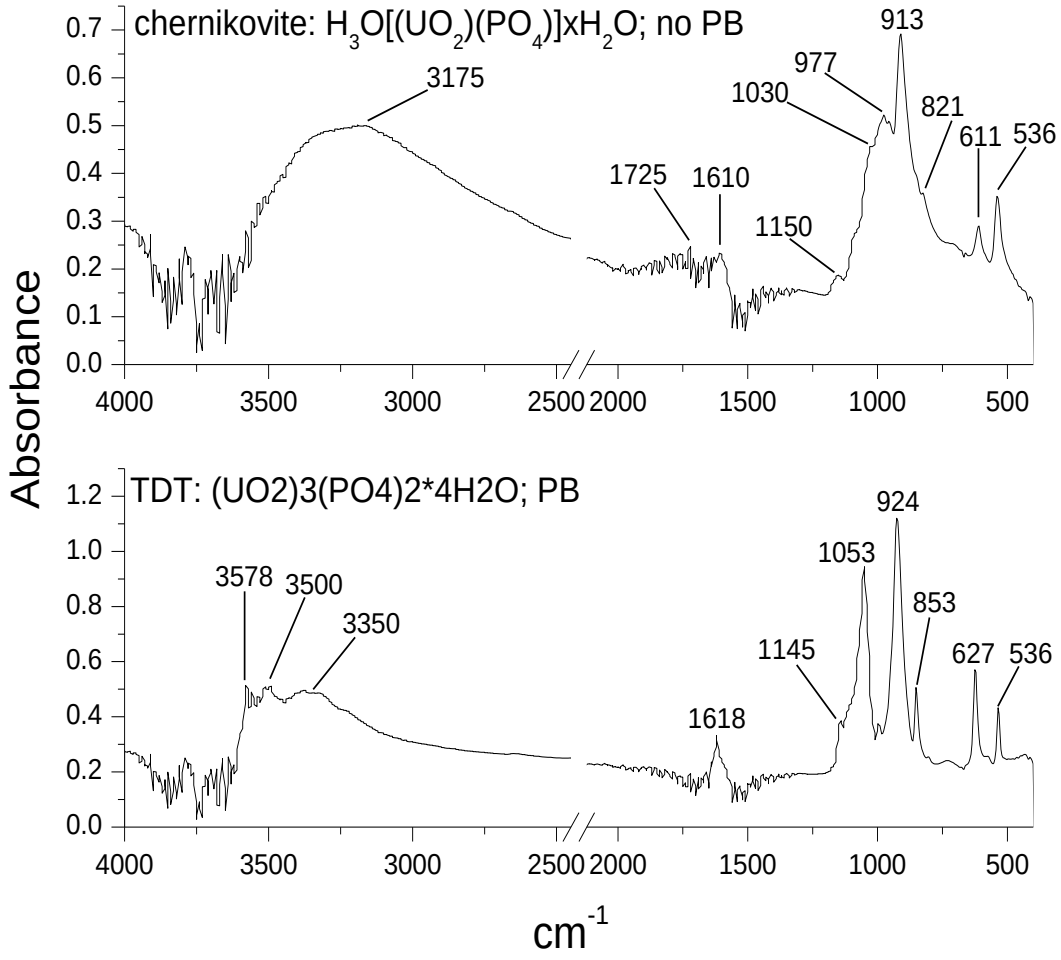

Fig. 19. ATR-IR spectra of chernikovite [$H_3O[(UO_2)(PO_4)]\bullet 4H_2O$] (top) and TDT: [$(UO_2)_3(PO_4)_2\bullet 4H_2O$] (bottom) showing structural evidence of distinct phases. No spectral features were observed in the region between ca. 2500 cm^{-1} and 2000 cm^{-1}; therefore this region was omitted for clarity.

Table 13. Band assignments for chernikovite with the corresponding IR spectrum in Fig. 19 (top panel).

Wavenumber (cm^{-1})	**Group**	**Vibrational Mode**
536	PO_4^{3-}	Bending; ν4
611	PO_4^{3-}	Bending; ν4
821	UO_2^{2+}	Antisymmetric stretch; ν1
913	UO_2^{2+}	Antisymmetric stretch; ν3
977	PO_4^{3-}	Antisymmetric stretching; ν3
1030	H_3O^+	Bending; ν2
1150	H_2O	Librational
1610	H_2O	Bending; ν2
1725	H_3O^+	Bending; ν4
3175	H_2O	Antisymmetric stretching; ν3

Table 14. Band assignments for TDT with the corresponding IR spectrum in Fig. 19 (bottom panel).

Wavenumber (cm^{-1})	Group	Vibrational Mode
536	PO_4^{3-}	Bending; ν4
627	PO_4^{3-}	Bending; ν4
853	UO_2^{2+}	Antisymmetric stretch; ν1
924	UO_2^{2+} -	Antisymmetric stretch; ν3
1053	PO_4^{3-}	Antisymmetric stretch; ν3
1145	H_2O	Librational
1618	H_2O	Bending; ν2
3350	H_2O	Symmetric stretching; ν1
3500	H_2O	ν1/ ν3
3578	H_2O	Antisymmetric stretching; ν3

Evidence of hydration abounds in both chernikovite and TDT. In addition to the rather distinct OH stretching modes at 3350, 3500 and 3578 cm^{-1} that are indicative of specific, discrete occupancies in the TDT framework, the broad, rather featureless band from ca. 3600 – 3100 cm^{-1} in TDT is a combination of many overlapping H-O-H antisymmetric and symmetric stretching vibrations and is strong evidence for significant H-bonding in the system and multiple H_2O bonding environments arising from structurally nonequivalent water groups in the unit cell (Cejka, 1999).

In addition to the strong indications of hydration (3175 and 1610 cm^{-1}), the chernikovite spectrum also shows ample evidence of the interlayer hydroxonium ion. Firstly, the v1 and v3 stretching modes of H_3O^+ are typically lower energy vibrations than their H_2O counterparts. Hence, these H_3O^+ stretching modes are observed at ca. 2500-3500 cm^{-1}, while the corresponding modes for H_2O are observed at ca. 3200-3600 cm^{-1}. Thus, the broad, rather non-descript feature starting at ca. 2500 cm^{-1} and centered at ca. 3175 cm^{-1} is likely the result of overlapping v1 and v3 bands of both H_3O^+ and H_2O. In contrast, the TDT spectrum features a considerably more gradual increase in intensity beginning at a higher wavenumber. Secondly, and perhaps most conspicuously, the band at ca. 1725 cm^{-1} is most likely the v4 bending mode of H_3O^+. Overlap with the v2 bending mode of H_2O centered at 1610 cm^{-1} results in a diminution of band intensity for both the H_3O^+ and H_2O bending modes. Without H_3O^+, the H_2O bending mode is typically relatively sharp and symmetric as shown in the TDT spectrum at 1618 cm^{-1} (bottom spectrum). Lastly, the weak band at ca. 1030 cm^{-1} is attributed to the v2 bending mode of H_3O^+. This vibrational mode is difficult to observe in hydrated uranyl phosphates (Rosiere, 1973; Cejka, 1999) since the relatively intense v3 PO_4 mode tends to mask the v2 bending mode of H_3O. However, in this sample of chernikovite, the significantly weakened v3 PO_4 mode centered at 977 cm^{-1} is evidence of significant band overlap between these two modes.

In addition to very broad features resulting from the overlap of several symmetric and antisymmetric OH stretching vibrations, highly resolved water modes are observed in both the chernikovite and TDT spectra. These are attributed to atmospheric H_2O as evidenced by the narrow bands in the bending and stretching regions of water. Additionally, the high resolution, high energy bands centered at ca. 3790 cm^{-1} are also attributed to atmospheric water. As noted above, surface water present in hygroscopic solids is readily observable with ATR-IR, typically

resembling water vapor, particularly when high resolution scans (≤ 8 cm^{-1}) are conducted and no spectral smoothing is employed.

4. DISCUSSION

Chemical digestion, PXRD and IR data provide clear evidence of the structural transformation of chernikovite into TDT. As noted above, chernikovite has been used as a starting material in the subsequent synthesis of other autunite phases via interlayer cation exchange. However, these studies involved simply the manipulation of the interlayer by substituting more favorable cations, presumably due to either stronger electrostatic affinity of divalent metals relative to H_3O^+, or a much higher concentration of the exchanging ion. Our results suggest a transformation within the structural unit and a concomitant configurational change in the uranyl ion from a square to a pentagonal bipyramid, as described in detail below.

4.1. Transformation of chernikovite into TDT

It has been suggested that under certain conditions, the edge-sharing configuration between adjacent pentagonal uranyl bipyramids may be more stable than the vertex-sharing uranyl square bipyramids and phosphate tetrahedra. A recent single crystal XRD study of synthetic uranyl phosphates and arsenates by Alekseev et al. (2008) proposed a structural pathway whereby vertex-sharing uranyl square bipyramids and phosphate tetrahedra transform into edge-sharing pentagonal uranyl bipyramids and phosphate tetrahedra (Fig. 20). Interestingly, this structural transformation comprises a uranyl polyhedral reorganization from square to pentagonal bipyramids. Alekseev et al., 2008 asserted that the hydrational state, i.e., the various roles of

water in the unit cell, played a key role in the overall topology of the structural unit in terms of determining 1-D infinite chains (dehydrated) vs. 2-D sheets (hydrated). Additionally, distinct water populations in the unit cell affect structural configurations locally by determining vertex- vs. edge- sharing polyhedral relationships and the coordination of the uranyl ion (square vs. pentagonal bipyramids).

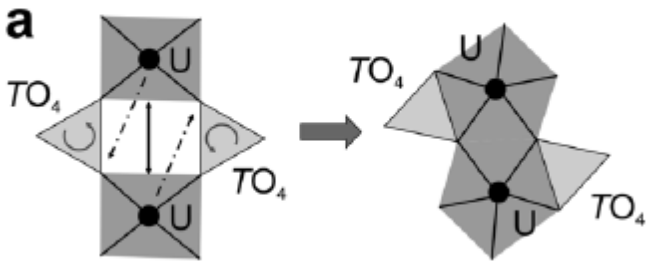

Fig. 20. Proposed structural shift from the meta-stable autunite anion topology to the more stable, edge sharing uranophane anion topology. This diagram is representative of both uranyl phosphates and arsenates, designated above as TO_4 tetrahedra (Alekseev et al., 2008).

In an analogous fashion, we propose that a similar structural transformation, from square to pentagonal bipyramids and from vertex- to edge-sharing polyhedra is taking place between chernikovite and TDT. Indeed this scheme seems plausible, at least from a thermodynamic perspective, since TDT is considerably less soluble than its autunite counterparts (particularly chernikovite).

5. Conclusion

Chemical digestion (Table 12), PXRD (Figs. 12 and 18) and IR data (Fig. 19) confirmed the transformation of chernikovite into TDT due to hydrothermal treatment. This finding suggests that, under the conditions of this study, edge-sharing uranyl pentagonal bipyramids present in the TDT structural unit are more stable than the corresponding chernikovite structural conformation, which comprises vertex-sharing uranyl square bipyramids. This study underscores the importance of rigorously characterizing synthetic uranyl compounds, particularly solids that are placed in a Parrbomb (at elevated temperature and pressure), since such treatment can result in the synthesis of a vastly different compound.

Acknowledgements

At Washington State University, this work was supported primarily by the U.S. Department of Energy, Basic Energy Sciences, Heavy Element Chemistry program, contract DE-FG02-06ER15782. In addition, SBC and CRA gratefully acknowledge support from the Joint Domestic Nuclear Detection Office-National Science Foundation: Academic Research Initiative (ARI), contract number ECCS-0833548 during the preparation of this manuscript. We also thank Dr. Louis Scudiero (WSU) for his assistance with TGA and DSC analyses and the WSU geological department for allowing CRA to use the XRD.

References

Langmuir, D. *Geochim. Cosmochim. Acta.,* **1978**, 42, 547-569.

Nininger, R.D. *Minerals for Atomic Energy,* **1954**, Van Nostrand.

Felmy, A.R., Xia, Y., Wang, Z. *Radiochim. Acta,* **2005**, 93, 401-408.

Womack, J.C., Larkin, D.J. *Investigation and evaluation of 102-BX tank leak. ARH-2035,* **1971**, Richland, WA, USA.

Van Haverbeke, L., Vochten, R., Van Springel, K. *Mineral. Mag.,* **1996**, 60, 759-766.

Vochten, R. *Amer. Mineral.,* **1990**, 75, 221-225.

Vochten, R. and Goeminne, A. *Phys. Chem. Minerals,* **1984**, 11, 95-100.

Vochten, R., De Grave, E., Pelsmaekers, J. *Amer. Mineral.,* **1984**, 69, 967-978.

Pham-Thi, M., Colomban, Ph. *J. Less-Common Met.,* **1985**, 189-216.

Cejka, J. *Reviews in Mineralogy Vol. 38.,* Eds. Burns, P.C., Finch, R. **1999**, 522-622.

Alekseev, E.V., Krivovichek, S.V., Malcherek, T., Depmeier, W. *J. Sol. State Chem.,* **2008**.

Rosiere, J. Thesis. Universite des Sciences et Technologie du Languedoc., **1973**, 150 pp.

CHAPTER FIVE

Solubility of triuranyl diphosphate tetrahydrate (TDT) and Na autunite at 23°C and 50°C

Christopher R. Armstrong[1], Andrew R. Felmy[2] and Sue B. Clark[2]*

[1]Washington State University, Pullman, WA 99164, U.S.A.
[2]Pacific Northwest National Laboratory, Richland, WA 99354, USA

Autunite / U(VI) phosphate minerals / Actinide contaminant remediation

Summary. In this report we present experimental solubility data for well-characterized triuranyl diphosphate tetrahydrate (TDT: $(UO_2)_3(PO_4)_2 \cdot 4H_2O$) and Na autunite ($Na[UO_2PO_4] \cdot xH_2O$) at 23°C and 50°C in $NaClO_4$-$HClO_4$ solutions at $pC_{H+} = 2$. Duplicate samples of TDT in 0.1, 0.5, 1.0, 2.0 and 5.0 m were equilibrated at 23°C and 50°C. TDT solid was synthesized and characterized with ICP-OES, ATR-IR and powder XRD before and after solubility experiments. The pH of the suspension was monitored throughout the experiments. Equilibrium was achieved from undersaturation with respect to TDT and Na autunite. Steady-state conditions were achieved in all cases within 82 days. TDT was unstable at ionic strengths above 0.1 m, where the complete conversion to Na autunite was observed. The ion-interaction model was used to interpret the experimental solubility data. The solubility product, log K_{sp}, for TDT was determined to be -49.7 and -51.3 at 23°C and 50°C respectively. Log K_{sp} for Na autunite was determined to be -24.4 (23°C) and -24.1 (50°C).

* Corresponding author: Tel: 01-509-335-1411; fax: 01-509-335-8867. Email: s_clark@wsu.edu

1. INTRODUCTION

Uranyl phosphates occur both naturally, in the vicinity of uraniferous alkali igneous rocks containing accessory apatite [1], and by anthropogenic means, where the interaction of U with either (i) apatite [2, 3, 4], or (ii) aqueous polyphosphates [5] results in the precipitation of these refractory phases. Consequently, several experimental studies have been conducted on the solubility of hydrated uranyl phosphates [6, 7, 8, 9]. These thermodynamic data (e.g., log K_{sp}) for relatively simple actinide-ligand systems assist in predicting the fate of *f*-elements in aquifer systems over a geological timescale. However, thermodynamic data obtained from experimental solubility studies of similar U^{6+} solids yield log K_{sp} values that are in some cases highly disparate [10]. Slight physico-chemical variations in the solid (e.g., degree of crystallinity, particle size, natural vs. synthetic sample, chemical impurities etc.) can lead to very different results. Moreover, quantification of the aqueous hydrogen concentration is often conducted improperly, leading to significantly erroneous results. In addition, inadequate characterization of both the initial solid and the final equilibrated phase render the correct interpretation of experimental results a challenge. In previous studies, we have shown that under favorable conditions, complete structural transformation of one hydrated uranyl phosphate into another occurs [11]. This finding stresses the importance of rigorously characterizing both the starting material and the end product, particularly in thermodynamic studies that involve variations in the physico-chemical conditions of the aqueous systems, e.g., temperature and/or ionic strength.

The main goal of this contribution is to determine the temperature dependence of TDT ($(UO_2)_3(PO_4)_2 \cdot 4H_2O$) and Na autunite ($Na[UO_2PO_4] \cdot xH_2O$) solubilities. Experimental thermodynamic studies have been carried out at room temperature ($23^oC \pm 1$) and a moderately elevated temperature ($50^oC \pm 0.5$) ranging in ionic strength from 0.1 m to 5.0 m. One aim of this present study is to conduct a thorough characterization of both the starting material and the end

product in solubility studies with varying ionic strength and temperature. To our knowledge these thermodynamic investigations of TDT and Na autunite at elevated temperature are the first to be reported.

2. MATERIALS AND METHODS

2.1 Chemicals

All chemicals are reagent grade or higher. Deionized (18 MΩ) and boiled water (DIW) was used in preparations of all solutions. Standards used for ICP-OES analyses were 99.9% purity. Concentrations of $HClO_4$ were verified by duplicate potentiometric titrations with standardized base solutions. A Metrohm pH meter (Model 713) equipped with a Ross combination pH electrode (Orion Model 8102) was used to measure the electromotive force (*EMF*). Prior to each use, the pH electrode was calibrated with NIST standards.

2.2 Experimental Set-Up

Experiments were carried out in 125 mL high density polyethylene bottles under room temperature conditions (23^oC ±1). For all of the samples, approximately 50 mg of solid was mixed with 50 g of DIW. The ionic strength was varied using 99.8% $NaClO_4$ and the initial pC_{H+} (negative log of hydrogen ion molality) was adjusted with 99% $HClO_4$. Duplicate samples were shaken continuously at 200 rpm using a circulating table. At selected time intervals, mixed suspensions were extracted and centrifuged using a Thermo Electron Sorvall Discovery M150 SE Ultracentrifuge at 120k rpm (7 minutes acceleration; 6 minutes at 120k rpm; 1 min deceleration). Duplicates of the supernatant were extracted, acidified with concentrated HNO_3,

diluted with degassed DIW and placed in 15 mL polypropylene centrifuge tubes and subsequently analyzed with a Perkin-Elmer Optima 3200 axial torch inductively-coupled plasma optical emission spectrometer (ICP-OES) for total U and P concentrations. Three replicates were completed for each analyte with the ICP, and the resulting concentrations were estimated from the calibration curves. The associated error was calibration, the quality control samples, the triplicate ICP readings, and the duplicate samples.

For solubility experiments conducted at 50^{o}C, a ThermoElectron shaking and circulating water bath was used, and the temperature variability was ± 0.5 ^{o}C. These samples were also constantly agitated at 200 rpm.

Attenuated total reflection infrared (ATR-IR) measurements were made on solids in this study using a Nicolet 6700 FT-IR spectrometer with an ATR accessory equipped with a ThermoElectron Smart Nexus Orbit single-reflection diamond IRE. Spectra were measured between 4000 and 400 cm^{-1} at 8 cm^{-1} resolution. A total of 200 scans were averaged for each sample and background. The system was purged with desiccated N_2 at 30 psi. As noted above, the solid samples were ground with an agate mortar and pestle and sieved to an approximate 150 µm particle size.

Powder x-ray diffraction (PXRD), was performed on fine grained samples (~ 150 µm) of TDT at room temperature using a Siemens Kristalloflex D500 diffractometer with the following parameters: Copper source (Kα; 1.54018 Å); 35 keV, 30 mA, Kβ filter: Ni; scintillation counter detector; Continuous mode: 0.02d/min; 2θ range: 5-55. The diffractograms were produced using MDI Data Scan 4 and Jade 8 software packages. No background corrections or smoothing was applied.

2.3 TDT Characterization

2.3.1 Triuranyl diphosphate tetrahydrate (TDT) synthesis

Microcrystalline TDT ($(UO_2)_3(PO_4)_2 \cdot 4H_2O$) was synthesized according to the modified method of Rai et al. [8]. Rigorous characterization of TDT including elemental analysis, PXRD, thermogravimetric analysis (TGA), differential scanning calorimetry (DSC), ATR-IR and Raman spectroscopy has been carried out in this laboratory in a separate study [11].

2.4 Activity Considerations

In this study, we measured pH on a concentration scale, which represents the negative log of hydrogen molality; and the pH is hereafter referred to as pC_{H+}. If activity coefficients and ionic strength are kept approximately constant, then pC_{H+} can be measured. To calculate the molal hydrogen concentration in all suspensions, it was necessary to prepare a series of standards, in duplicate, at all ionic strengths, at both 23 and 50^{o}C, and at pC_{H+} = 2, to construct calibration curves of pH calculated vs. pH measured. The molal hydrogen concentrations were thus obtained and the average (and 1-σ) of duplicates is expressed as pC_{H+} in Table 15. These solubility experiments were conducted in acidic media for the following reasons. First, U^{6+} phosphates are highly insoluble at or above circumneutral pH. Thus a relatively low pH was essential to ensure adequate dissolution such that total aqueous concentrations could be accurately quantified with ICP-OES. Second, the equilibria (e.g., speciation) of the system are greatly simplified at low pH. Third, by maintaining low pH systems, we can neglect carbonate and most UO_2 hydrolysis species, thereby further simplifying the interpretation of the thermodynamic data.

3. RESULTS AND DISCUSSION

3.1 Experimental results

The dissolved concentrations of both U and P were measured periodically and are shown in Figs. 21-25. For both temperatures, steady-state conditions were attained from undersaturation in the case of TDT and oversaturation in the case of Na autunite, due to the conversion of the former phase to the latter at elevated ionic strengths, as described below. The lower ionic strength samples (0.1 m and 0.5 m) reached steady-state relatively quickly, in approximately 25 days. Note that the 0.5 m (23^{o}C) system exhibits markedly non-stoichiometric TDT dissolution, as the concentration of P is inordinately low. At elevated (1.0, 2.0 and 5.0 m) ionic strengths, dissolved P decreases to concentrations that are around the detection limit of the ICP-OES (ca. 0.05 ppm). This is primarily due to the precipitation of Na autunite, as discussed in the following section. For this reason, extra time was required to demonstrate steady-state conditions. A summary of the results for all of the experimental runs is shown in Table 15. The steady-state values of U and P reported in Table 15 are the average with 1-sigma uncertainty of duplicate runs for each experimental system.

Table. 15. Summary of experimental results in $NaClO_4$-$HClO_4$ media at 23 and 50°C after 89 days and 82 days respectively.

Experimental system	**Ionic strength (m)**	**T (°C)**	**U (m)**	**P (m)**	**pC_{H+}**
0.0099 m $HClO_4$/0.09 m $NaClO_4$	0.1	23 50	5.02E-4(±7.09E-6) 3.35E-4(±2.27E-5)	3.15E-4(±2.47E-5) 2.36E-4(±3.40E-5)	2.07 (±0.06) 1.86 (±0.10)
0.0099 m $HClO_4$/0.049 m $NaClO_4$	0.5	23 50	7.70E-4(±1.2E-4) 3.50E-4(±1.68E-5)	8.24E-5(±4.03E-5) 2.44E-4(±1.76E-5)	1.90 (±0.04) 2.01 (±0.04)
0.0099 m $HClO_4$/0.99 m $NaClO_4$	1.0	23 50	9.11E-4(±1.11E-4) 8.83E-4(±3.70E-5)	4.78E-5(±2.34E-5) 5.41E-5(±6.70E-6)	1.78 (±0.07) 2.08 (±0.02)
0.0099 m $HClO_4$/1.99 m $NaClO_4$	2.0	23 50	8.31E-4(±1.53E-4) 8.96E-4(±1.84E-4)	9.90E-6(±1.40E-5) 4.99E-5(±2.33E-5)	1.85 (±0.07) 1.88 (±0.01)
0.0099 m $HClO_4$/4.99 m $NaClO_4$	5.0	23 50	8.07E-4(±1.06E-4) 7.62E-4(±2.63E-4)	3.09E-4(±4.26E-4) 1.20E-4(±1.45E-4)	2.02 (±0.27) 2.07 (±0.33)

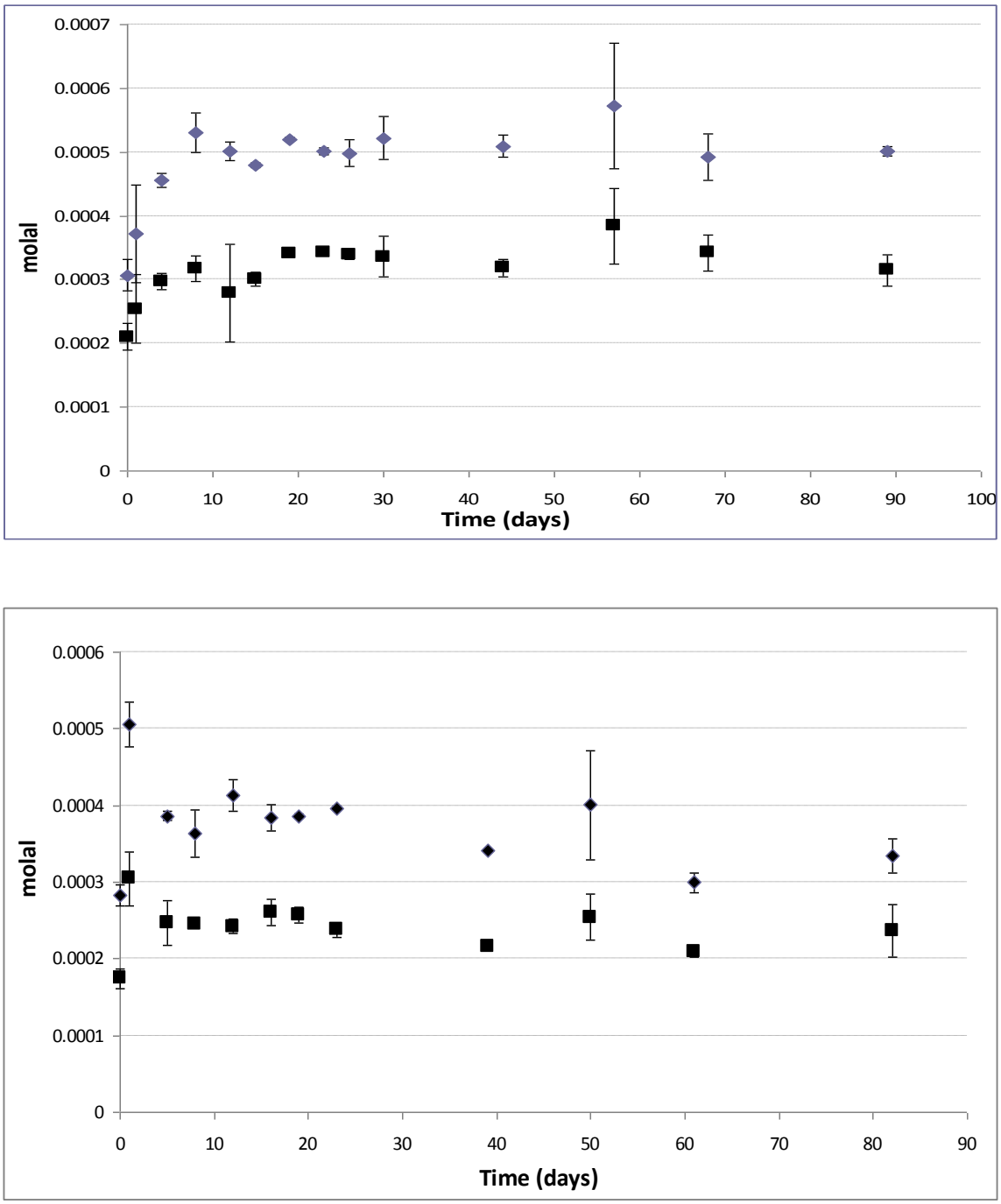

Fig. 21. Approaching equilibrium from undersaturation of $(UO_2)_3(PO_4)_2 \cdot 4H_2O$; 0.1 m $NaClO_4$; initial pC_{H^+} = 2;T= 23°C (top); 50°C (bottom). Diamonds: U; Squares: P. Error bars represent 1-sigma of duplicates.

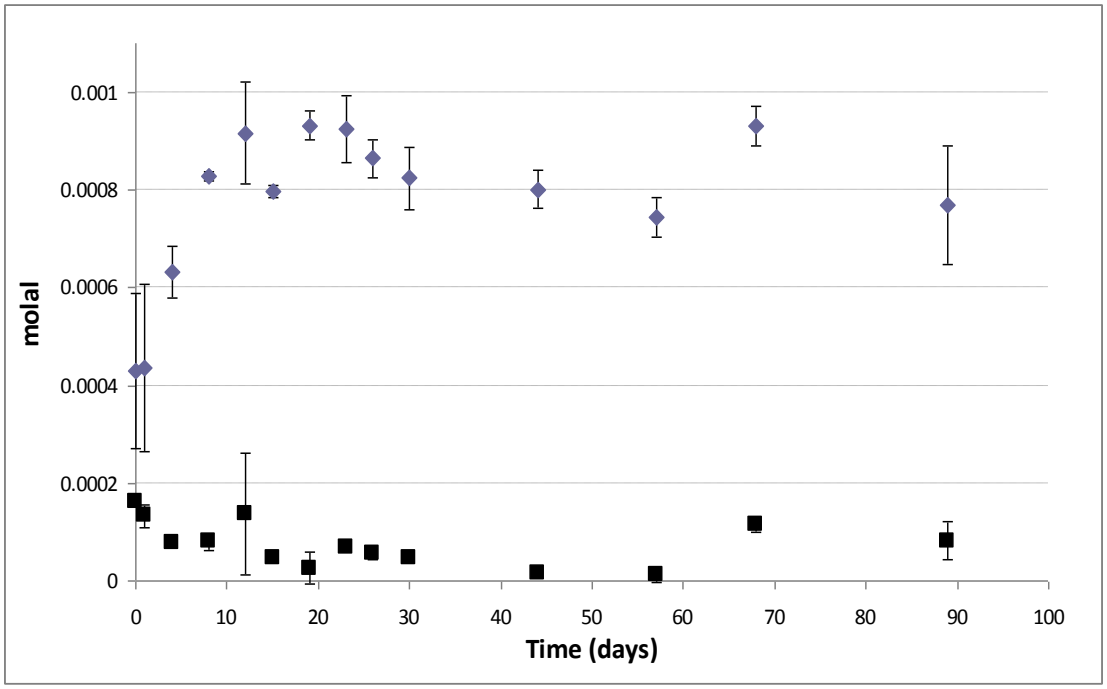

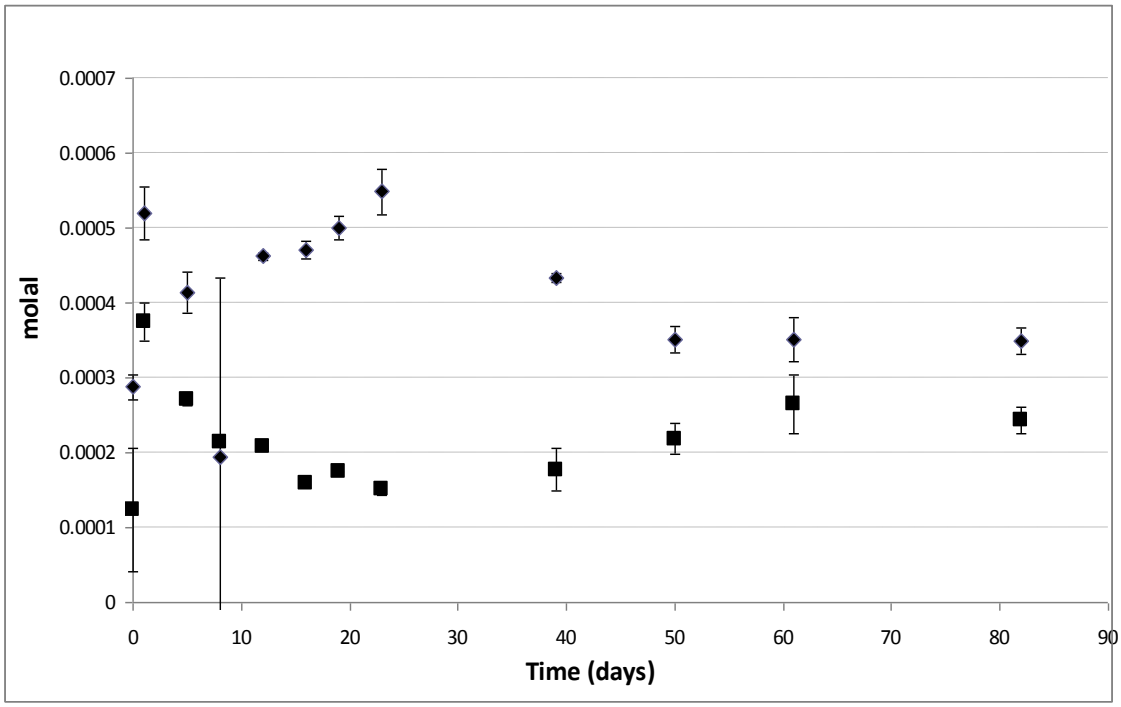

Fig. 22. Approaching equilibrium from undersaturation of $(UO_2)_3(PO_4)_2 \cdot 4H_2O$; 0.5 m $NaClO_4$; initial pC_{H^+} = 2;T= 23^{o}C (top); 50^{o}C (bottom). Diamonds: U; Squares: P. Error bars represent 1-sigma of duplicates.

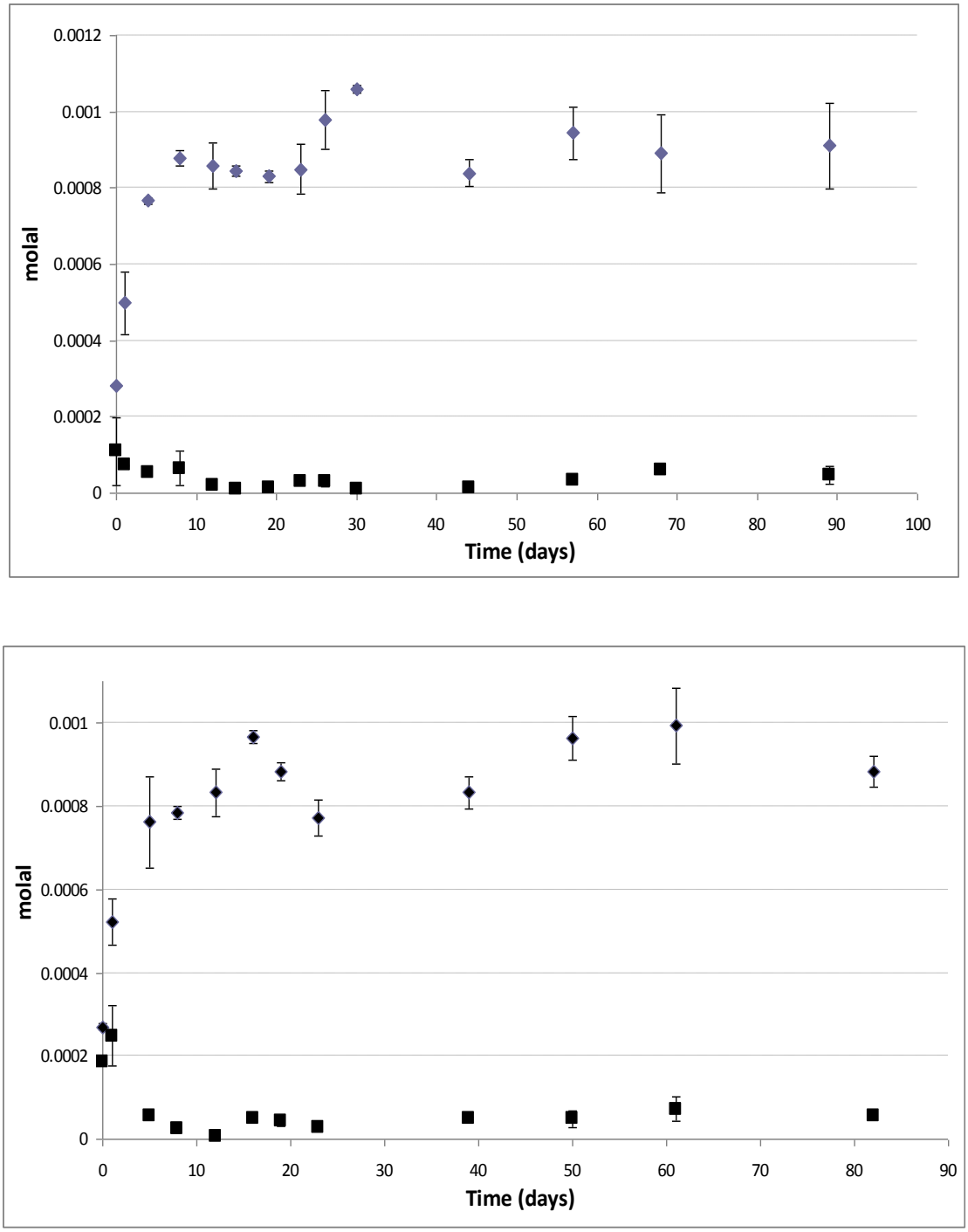

Fig. 23. Approaching equilibrium from undersaturation of $(UO_2)_3(PO_4)_2 \cdot 4H_2O$; 1.0 m $NaClO_4$; initial pC_{H+} = 2;T= 23°C (top); 50°C (bottom). Diamonds: U; Squares: P. Error bars represent 1-sigma of duplicates.

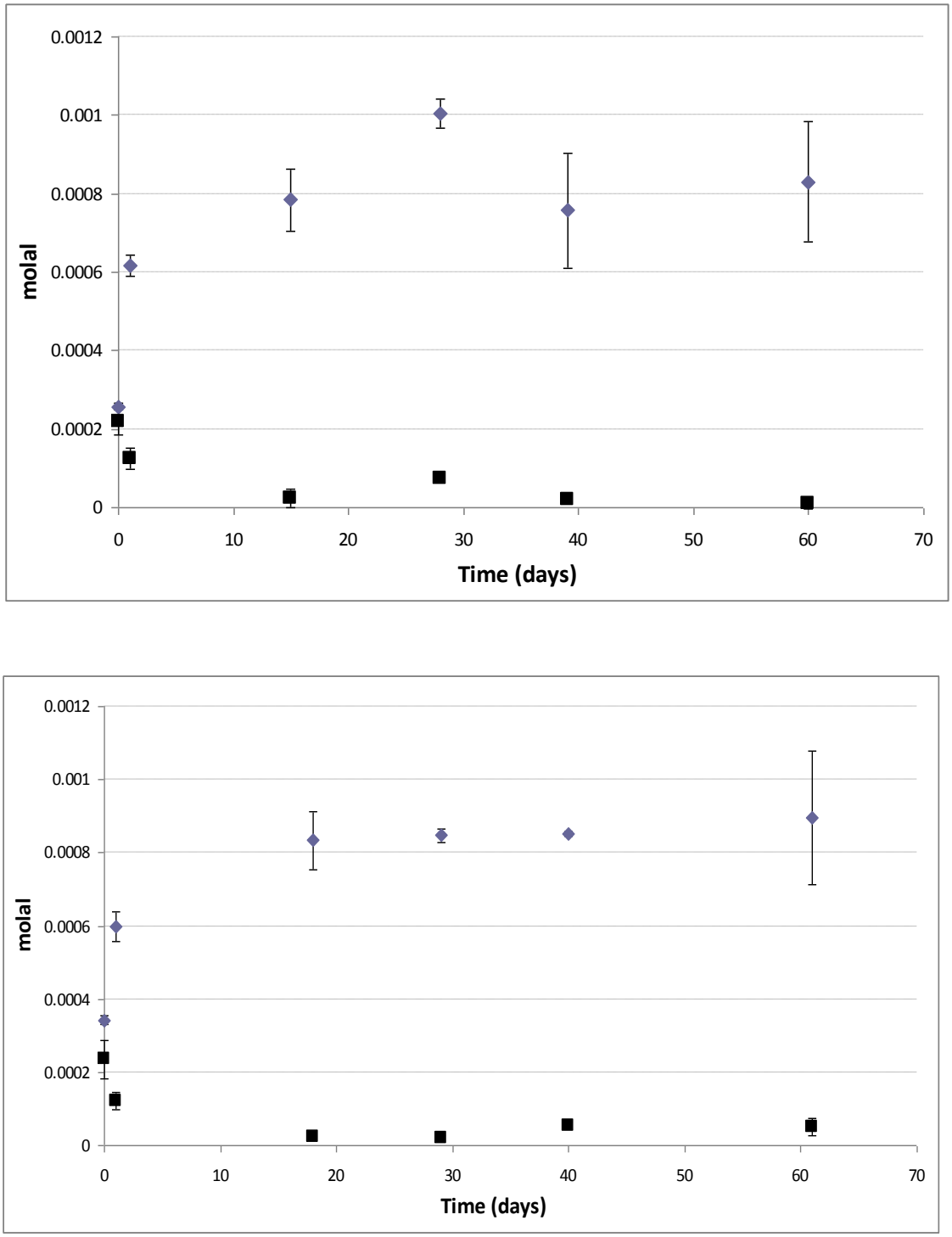

Fig. 24. Approaching equilibrium from undersaturation of $(UO_2)_3(PO_4)_2 \cdot 4H_2O$; 2.0 m $NaClO_4$; initial pC_{H^+} = 2;T= 23°C (top); 50°C (bottom). Diamonds: U; Squares: P. Error bars represent 1-sigma of duplicates.

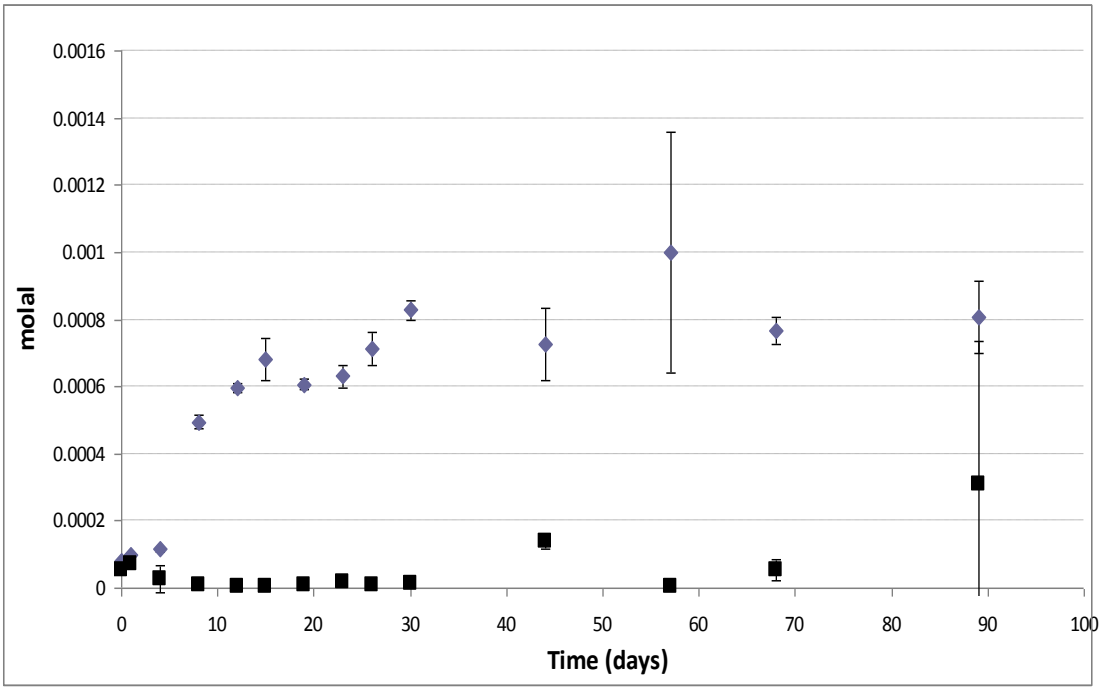

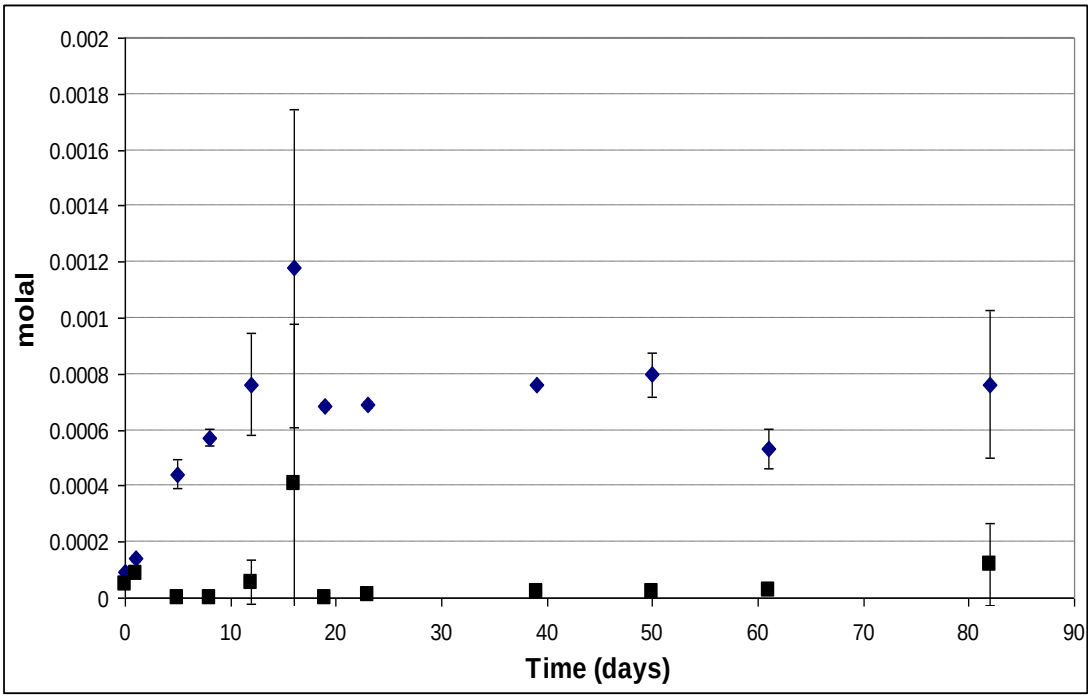

Fig. 25. Approaching equilibrium from undersaturation of $(UO_2)_3(PO_4)_2 \cdot 4H_2O$; 5.0 m $NaClO_4$; initial pC_{H^+} = 2;T= 23°C (top); 50°C (bottom). Diamonds: U; Squares: P. Error bars represent 1-sigma of duplicates.

3.2 Final TDT characterization

Due to the incongruent dissolution of TDT observed when the ionic strength exceeded 0.1 m (Figs. 21-25), it was necessary to thoroughly evaluate the end-product solid. After achieving steady-state U and P concentrations, samples at the same ionic strength (both temperatures) were compared. Elemental analysis and IR data showed excellent agreement. For PXRD, the 1.0 m and 5.0 m samples were similar, with the exception of two minor peaks in the heated 1.0 m sample. These diffractions suggest a change in hydration for the sample at elevated temperature [11]. Thus, no significant differences were observed between 23°C and 50°C samples when ionic strengths were directly compared. For these reasons, and for simplicity, we show post-run data for the 23°C samples only.

3.2.1 Final elemental analysis of the solids

Suspensions of the 0.1, 1.0 and 5.0 m ionic strength equilibrated samples were withdrawn and vacuum-filtered with 0.45µm Millipore filters. The filtered solids were rinsed repeatedly with boiling 18 MΩ DIW and air-dried. Dried samples were ground with a mortar and pestle to particle sizes of approximately 150 µm. Approximately 10 mg of the solids were digested (the remainder was stored for IR and XRD analyses) with concentrated HNO_3, diluted to 100 mL with degassed 18 MΩ DIW and analyzed with ICP-OES. These samples were prepared in duplicate. The U and P ratios obtained after chemical digestion of the end-product solids are shown in Table 16.

Table. 16. Ratios of U:P in various digested solids measured by ICP-OES. These values represent the average of duplicate samples of each solid. The 23°C samples were equilibrated for 89 days in the ionic strengths indicated and the 50°C suspensions were equilibrated for 82 days. The initial (pre-run) TDT shows a slightly high U concentration. The 0.1 m samples (both temps) yield U:P ratios that are consistent with TDT. However, both the 1.0 m and 5.0 m solids have U: P ratios that are more consistent with Na autunite ($Na[(UO_2)(PO_4)]\bullet xH_2O$).

Sample	Temp. (°C)	U/P
Initial TDT	-	1.55
0.1 m	23	1.50
0.1 m	50	1.50
1.0 m	23	0.99
1.0 m	50	1.00
5.0 m	23	0.98
5.0 m	50	1.00

For both temperatures, the 0.1 m sample did not change during the equilibration period (89 days and 82 days). However the 1.0 m and 5.0 m U:P ratios decreased from initially ca. 1.5 to ca. 1, which strongly suggests alteration of the TDT, most likely to sodium autunite: $Na[UO_2PO_4]\bullet xH_2O$. Because the P concentrations increased initially before decreasing markedly (Figs. 21-25), we believe that the TDT is dissolving before reprecipitating as Na autunite. Consequently, U remains in solution even with the precipitation of the secondary phase because of the difference in the U:P stoichiometry for the two phases.

3.2.2 Final solid phase characterization by ATR-IR

After the completion of the solubility experiments, the remaining solids were analyzed by ATR-IR. Fig. 26 shows the IR spectra of 0.1 m and 1.0 m equilibrated solids. Because the 5.0 m spectrum was almost identical to that of the 1.0 m sample, it was omitted. In addition, the IR spectrum of a sample of synthetic Na autunite is included for comparison (Fig. 26, top panel). The IR spectrum of the TDT starting material was identical to that of the 0.1 m equilibrated solid (data not shown), and these spectra were in good agreement with published data [12]. In contrast, the 1.0 m and 5.0 m samples, although almost mutually identical, are very different than both the initial TDT product and the 0.1 m solids, instead showing spectral features that are more consistent with a Na autunite phase [13].

The following uranyl and phosphate stretching modes provide the most compelling evidence for a TDT-to-Na autunite conversion at ionic strengths above 0.1 m. First, the symmetric stretching mode of uranyl ($\nu1\ UO_2^{2+}$) is shifted from 853 cm^{-1} to ca. 802 cm^{-1}. Second, a red-shift from 924 cm^{-1} to ca. 890 cm^{-1} is evident in the uranyl antisymmetric stretching ($\nu3\ UO_2^{2+}$) mode. Third, a red-shift from 1053 cm^{-1} to ca. 980 cm^{-1} in the $\nu3\ PO_4^{3-}$ mode is also observed. All of these lower energy vibrational modes are expected in autunite rather than in TDT.

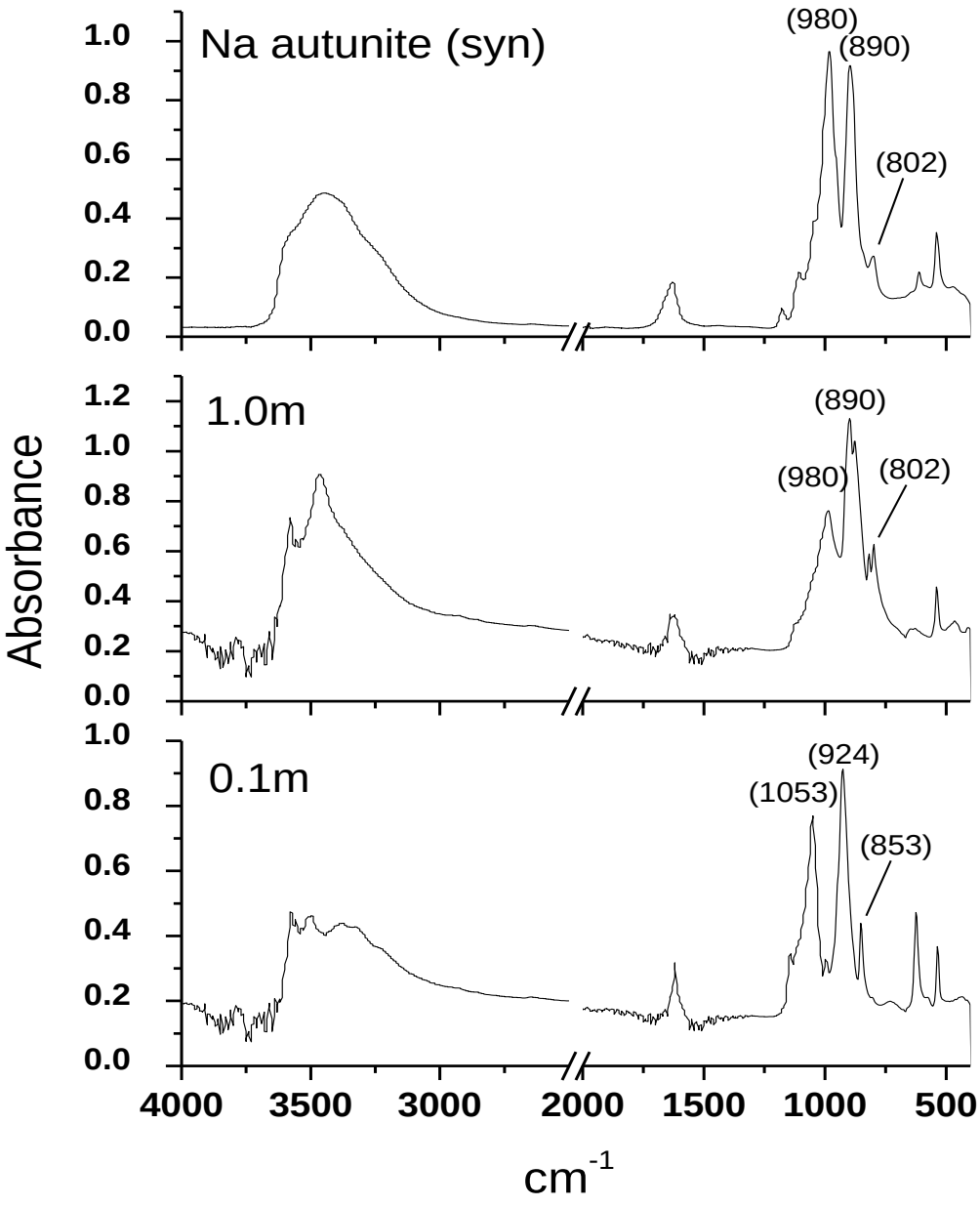

Fig. 26. IR spectra of selected final, equilibrated solids (1.0 m $NaClO_4$ sample, middle panel; 1.0 m $NaClO_4$ sample at bottom) together with a synthetic Na autunite powder (top), shown for comparison. No spectral features were observed in the region between ca. 2500 cm^{-1} and 2000 cm^{-1}; therefore part of this region was omitted for clarity.

3.2.3 Final solid phase analysis by PXRD

In agreement with ICP and IR data, the 0.1 m sample is identical to the starting material (i.e., no equilibration with a solution phase); and it is consistent with the PDF # 37-0369 for TDT (Fig. 27, bottom panel). In contrast, the 1.0 m and 5.0 m samples are very similar although they are markedly different than both the 0.1m equilibrated suspension and PDF # 39-0369, again in agreement with ICP and IR data. A comparison of these 1.0 m and 5.0 m solids and the published XRD profile for Na autunite (73-7368) shows very good agreement (Fig. 27, top panel). Thus, these XRD findings support the data obtained from IR analyses of the post-solubility 0.1 m, 1.0 m and 5.0 m solids, namely that the 0.1 m equilibrated solid does not undergo any transformation, whereas the 1.0 m and 5.0 m samples show strong evidence of a transformation of TDT to Na autunite.

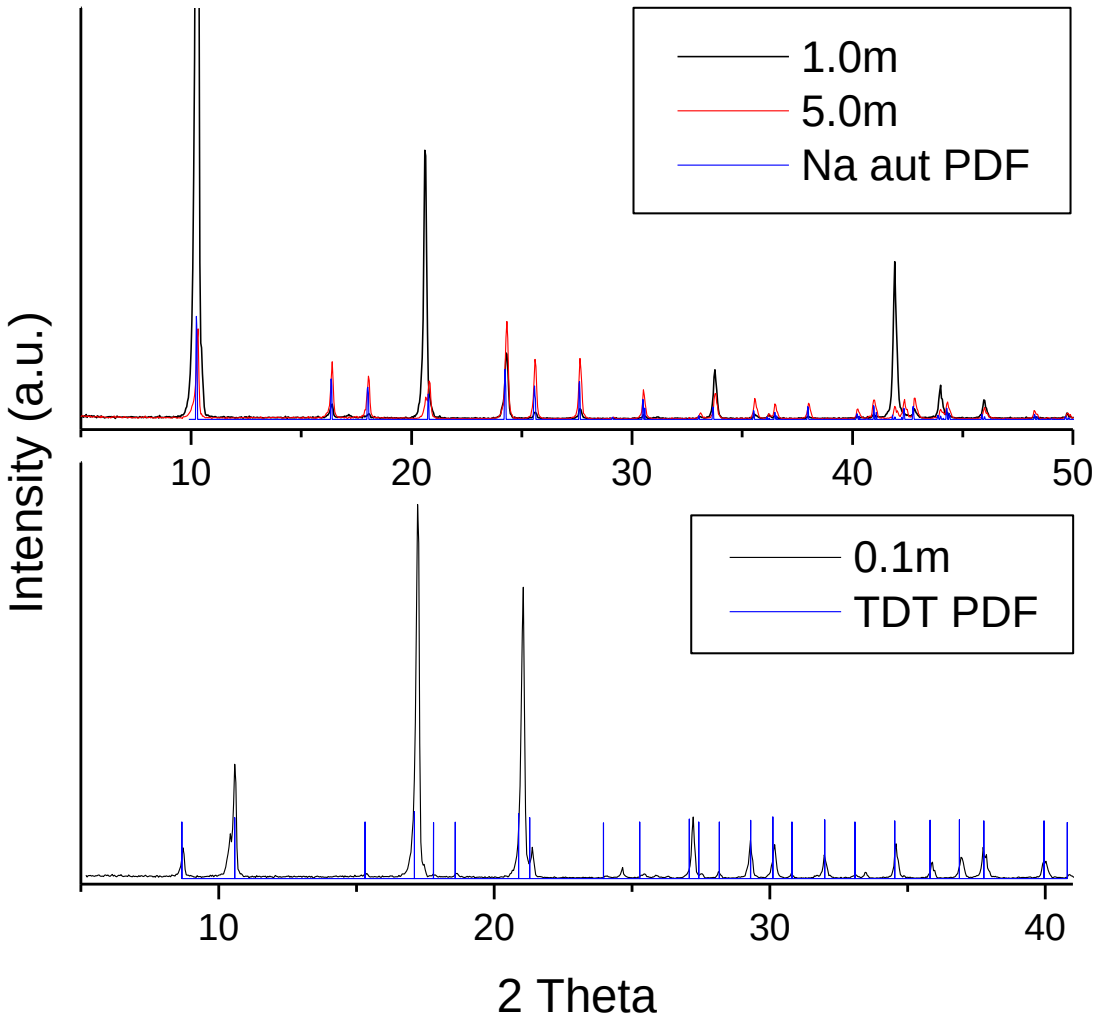

Fig. 27. XRD diffractograms of selected equilibrated solids. Top panel: 1.0 m and 5.0 m $NaClO_4$ together with the PDF for Na autunite (73-7368); bottom panel: 0.1 m $NaClO_4$ and a TDT PDF (37-0369).

3.3 Thermodynamic modeling

The aqueous thermodynamic model used in this study to interpret the solubility data is the ion-interaction model of Pitzer [14, 15]. This model emphasizes a detailed description of the specific ion interactions in the solution, the exact form of which is given elsewhere [16, 17, 18]. The Pitzer thermodynamic model was used because it is applicable from zero to high ionic strengths, and our solubility data extend to high ionic strength (I ~ 5 m).

In these calculations the stability constants for U(VI) species with phosphate were included from the recent NEA review of Guillamont et al. [19]. See Table 17 for details. In addition, Table 18 includes a summary of the Pitzer ion-interaction parameters considered in this study.

Table 17. Equilibrium constants for U(VI) aqueous speciation reactions used in this study [19].

Reaction	*logK*
$UO_2^{2+} + H_2O \rightleftharpoons UO_2OH^+ + H^+$	-5.25
$UO_2^{2+} + HPO_4^{2-} \rightleftharpoons UO_2HPO_4(aq)$	7.24
$UO_2^{2+} + H_3PO_4 \rightleftharpoons UO_2H_2PO_4^+ + H^+$	1.12
$UO_2^{2+} + H_3PO_4 \rightleftharpoons UO_2H_3PO_4^{2+}$	0.76
$UO_2^{2+} + 2H_3PO_4 \rightleftharpoons UO_2(H_2PO_4)_2\ (aq) + 2H^+$	0.64
$UO_2^{2+} + 2H_3PO_4 \rightleftharpoons UO_2H_2PO_4H_3PO_4 + H^+$	1.65

Table 18. Pitzer ion-interaction parameters used in this study. All values from Pitzer [15] except θ_{H+-Na+} from Harvie et al. [16].

Ion- Interaction	Parameter	Value
Na^+-$H_2PO_4^-$	β^0	-0.0533
	β^1	0.0396
	C^θ	0.0075
Na^+-ClO_4^-	β^0	0.0554
	β^1	0.2755
	C^θ	-0.00118
UO_2^{2+}-ClO_4^-	β^0	0.6113
	β^1	2.144
	C^θ	0.01084
H^+-ClO_4^-	β^0	0.1747
	β^1	0.2931
	C^θ	0.00819
H^+ - Na^+	θ	0.036

Using these data along with previously published solubility product constants of TDT from [9] and sodium autunite [8], we calculated the solubilities of both TDT and sodium autunite as a function of $NaClO_4$ concentration. The predicted solubilities showed that TDT should be the thermodynamically stable phase only in the 0.1 m $NaClO_4$ solution. At higher concentration sodium autunite was predicted to be stable, in agreement with the experimental observations. We then used the data for TDT solubility in the 0.1 m $NaClO_4$ solutions to estimate a solubility product for the material used in this study. The results yielded a log K_{sp} for TDT of -49.7 at 23°C and -51.3 at 50°C for the reaction ($(UO_2)_3(PO_4)_2 \cdot 4H_2O \rightleftharpoons 3UO_2^{2+} + 2PO_4^{3-} + 4H_2O$). The value of -49.7 at 23°C compares well with the values of -49.08 and -49.36 at 25°C by Rai et al. [9] and Guillaumont et al. [19] respectively. The value at 50°C is the first determination of the K_{sp} at this temperature. It should be noted that the 50°C value is only an estimate since the U(VI)-PO_4 complexation constants (Table 17) are not known as a function of temperature.

However, in these systems the uncomplexed UO_2^{2+} species dominates the overall U(VI) speciation (~90%). Therefore, the estimated K_{sp} at 50°C should be reasonable. The lower value for the K_{sp} at 50°C reflects the lower U(VI) and phosphate concentrations in solution relative to the room temperature samples and suggests that TDT may exhibit retrograde solubility, a finding that has been observed with lanthanide phosphates [20].

The determination of the K_{sp} for sodium autunite was considerably more difficult at 23°C owing to relatively large changes in the apparent K_{sp} as a function of ionic strength. However, at the lowest concentration in which sodium autunite was predicted to be stable (0.5 m $NaClO_4$), the calculated log K_{sp} for the reaction ($NaUO_2PO_4.xH_2O \rightleftharpoons Na^+ + UO_2^{2+} + PO_4^{3-} + xH_2O$) was -24.4 compared to the value determined by Felmy et al. [8] (log K_{sp} = -23.6). At 50°C the results as a function of ionic strength extending from 0.5 m $NaClO_4$ to 5.0 m $NaClO_4$ were all in reasonable agreement. Fitting all of these data together yielded a log K_{sp} of -24.1. This is the first determination of the solubility product for sodium autunite at temperatures above 25°C.

4. SUMMARY

Experimental solubility studies of TDT and Na autunite have been conducted over a wide ionic strength range (0.1 to 5.0 m) at both 23°C and 50°C. ICP-OES, PXRD and IR data were all in agreement showing that (1) at comparable ionic strengths, the 23°C and 50°C equilibrated solids showed no significant differences, and (2) the 0.1 m solids remained unchanged over the 89 day equilibration period. However, the 1.0 m and 5.0 m samples showed strong evidence of a conversion of TDT to Na autunite. The ion-interaction model of Pitzer [14, 15] was used to interpret the experimental solubility data for both TDT and Na autunite at 23°C and 50°C. The log K_{sp}'s for TDT at 23°C and 50°C respectively are: -49.7 and -51.3; and the log K_{sp}'s for Na

autunite at 23^{o}C and 50^{o}C respectively are: -24.4 and -24.1. The room temperature values for both of these phases are in agreement with published data, while the thermodynamic data obtained at 50^{o}C are the first to be reported for these phases. It appears that TDT may exhibit slight retrograde solubility, while no significant temperature dependence is evident in the case of Na autunite.

Acknowledgements

This work was supported primarily by the U.S. Department of Energy, Basic Energy Sciences, Heavy Element Chemistry program, contract DE-FG02-06ER15782. In addition, SBC and CRA gratefully acknowledge support from the Joint Domestic Nuclear Detection Office-National Science Foundation: Academic Research Initiative (ARI), contract number ECCS-0833548 during the preparation of this manuscript.

References

1. Langmuir, D. Geochim. Cosmochim. Acta. **42,** 547 (1978).
2. Jeanjean, J., Rouchaud, J.C., Tran, L., Federoff, M. J. Radioanal. Nucl. Chem., Lett. **6,** 529 (1995).
3. Fuller, C.C, Bargar, J.R., Davis, J.A., Piana, M.J. Environ. Sci. Technol, ***36,*** 158 (2002).
4. Fuller, C.C, Bargar, J.R., Davis, J.A. Environ. Sci. Technol. ***37,*** 4642 (2003).
5. Wellman, D.M. Ph.D. Dissertation, Washington State University, Pullman, WA, (2004) 196 pp.
6. Vesely, V., Pekarek, V., Abbrent, M. J. Inorg. Nucl. Chem. **27,** 1159 (1965).
7. Sandino, A., Bruno, J. Geochim. Cosmochim. Acta. **56,** 4235 (1992).
8. Felmy, A.R., Xia, Y., Wang, Z. Radiochim. Acta **93,** 401 (2005).
9. Rai, D., Xia, Y., Rao, L., Hess, N.J., Felmy, A.R., Moore, D.A., McCready, D.E. J. Sol. Chem. **34,** 69 (2005).
10. Gorman-Lewis, D., Burns, P.C., Fein, J.B. J. Chem. Thermodyn. **40,** 335 (2008).
11. Armstrong, C.R. PhD dissertation. Washington State University (2009).
12. Pham-Thi, M. and Colomban, Ph. J. Less-Common Met. **108,** 189 (1985).
13. Cejka, J. Reviews in Mineralogy Vol. 38. Eds. Burns, P.C., Finch, R. 522 (1999).
14. Pitzer, K. S. J. Phys. Chem. **77,** 268 (1973)
15. Pitzer, K. S. *Activity Coefficients in Electrolyte Solutions, 2nd ed*. Boca Raton, Florida, CRC Press (1991).
16. Harvie, C. E., Møller, N., Weare , J. H. Geochim. Cosmochim. Acta **48,** 723 (1984).
17. Felmy, A. R., Weare, J. H. Geochim. Cosmochim. Acta **50,** 2771 (1986).
18. Felmy, A. R., Rai, D., Schramke, J. A., Ryan, J. L. Radiochim. Acta **48,** 29 (1989).
19. Guillamont, R., Fanghanel, T., Fuger, J., Grenthe, I., Neck, V., Palmer, D.A., Rand, M.H. Update on the Chemical Thermodynamics of Uranium, Neptunium, Plutonium, Americium,

and Technetium. Chemical Thermodynamics, Vol. 5. Elsevier Science Publishers, Amsterdam, North-Holland (2003).

20. Cetiner, Z.S., Wood, S., Gammons, C.H. Chem. Geol. **217,** 147 (2003).

CHAPTER SIX

The enthalpy of hydration for U^{6+} solids: A thermal study

Christopher R. Armstrong, Kenneth L. Nash, Sue B. Clark[3]

Dept. of Chemistry, Washington State University, Pullman, WA 99164, U.S.A.

Abstract

A new method of delineating the types of water present in uranyl oxysalts is presented. Two well-characterized uranyl phosphates, natural meta autunite ($Ca[(UO_2)(PO_4)]_2 \cdot 6.5H_2O$) and synthetic sodium autunite ($Na_2[(UO_2)(PO_4)]_2 \cdot 3H_2O$) are investigated. Complementary data from thermogravimetric analysis (TGA) and differential scanning calorimetry (DSC) are accrued and the roles of water are elucidated. Three types of water are thus distinguished: (1) physisorbed, (2) occluded and, (3) interstitial-coordinated. Each type of water is discussed in the context of its respective enthalpy of hydration. The novel approach described herein can be readily applied to a variety of hydrated minerals and synthetic compounds.

[3]Corresponding author: Tel: 01-5093351411; fax: 01-509-3358867. Email: s_clark@wsu.edu

1. INTRODUCTION

1.1 Background

Tardy and Garrels (1974, 1976, 1977) developed a simple method of estimating the standard state free energies of formation (ΔG_f^o) for various minerals by summing the stoichiometric ΔG_f^o contributions of the constituent components. The efficacy of this approach rests upon the assumption that the standard state free energy of formation for a given component oxide is the same for all phases in which the component is present in a similar structural arrangement.

This method was subsequently used to estimate ΔG_f^o for uranyl oxides (Finch, 1997), uranyl silicates (Clark et al., 1998) and a variety of U phases (Chen et al., 1999). Clark et al. (1998) demonstrated a linear relationship between the waters of hydration and the standard state free energy of formation for hydrated uranyl nitrates, sulfates and phosphates. These workers used the mean of the slopes of free energy vs. waters of hydration to interpolate/extrapolate the contribution of free energy of the component water to the standard state free energy of formation of select uranyl silicates. Although it would appear that this method provides a rough estimate of the weighted average of component water in the summing exercise, it does not differentiate the different types of water present in these solid phases; and thus error in these assessments is unavoidable.

Chen et al. (1999) modified this approach by accounting for the coordination environments of all of the constituent components in a given unit cell. A multiple linear regression scheme was employed using experimental thermodynamic data from a host of uranyl solids. These workers demonstrated that ΔG_f^o and ΔH_f^o of uranyl minerals can be effectively estimated by summing the oxide polyhedral contributions, which they referred to as “fictive” structural components.

1.2. Rationale

As pointed out by Chen et al. (1999), estimating the standard state free energies of formation for U^{6+} phases based upon the summing of individual constituent components from available thermodynamic data is problematic for several reasons. Firstly, the free energies of these components in pure substances (e.g., MgO (pure) vs. constituent MgO (in oxysalt) can be vastly different. Secondly, the differences in stoichiometry and degrees of disorder, i.e., highly distorted uranyl polyhedra, can also greatly affect these types of estimations. Lastly, knowledge of the bonding environments of water, and the ΔG_f^o associated with these water molecules, is lacking.

As noted above, water is invariably assigned an individual ΔG_f^o which is subsequently applied to the stoichiometric contribution of water to the given solid. It has been widely shown that the role of water in hydrated oxysalts is highly complex and, to a large extent, governs the overall stability of the solid phase (Hawthorne, 1992; Hawthorne and Schindler, 2008; Schindler and Hawthorne, 2008). Thus it is clear that treating the plurality of water bonding environments as an individual component leads to erroneous ΔG_f^o estimations.

Chen et al. (1999), attempted to distinguish between two types of water, water of hydration and structural water. However it is not clear how these assignments were made, since the water of hydration could be either physisorbed or occluded water. Additionally, the designation of structural water is somewhat misleading, since many U^{6+} phases do not contain any structural water; instead these are typically water molecules that are coordinated to the interlayer metal in the interstitial region. Lastly, in cases where hydroxyl groups were present in the structural unit, Chen et al. treated these OH groups as water groups, assigning 0.5 moles of structural water for every mole of OH observed. While this approach is likely an improvement

over previous attempts to handle the complexities of uranyl mineral hydration, it does not delineate the "structural" water and waters of hydration in terms of their respective free energy contributions to the ΔG_f^o of the U solid of interest.

In this report, the importance of considering the energetic contributions arising from different hydration components in uranyl oxysalts is discussed; and we endeavor to provide specific enthalpies of hydration for these respective water populations. Here we present thermodynamic data obtained from TGA and DSC delineating distinct water populations in two hydrated uranyl phosphates: natural meta autunite and synthetic sodium autunite.

In this contribution, the convention of Hawthorne (1992) was followed, i.e., three types of water: (1) physisorbed, (2) occluded and, (3) interstitial-coordinated water are designated. A thorough discussion of these designations is presented elsewhere (see Introduction of this dissertation). Briefly, the physisorbed water represents all water molecules that are adsorbed to the surface of the solid, effectively in equilibrium with atmospheric water. Occluded water describes water molecules that are occupying available space within the interlayer (i.e., zeolitic water). These waters are held in place by hydrogen bonding. Lastly, interstitial-coordinated water describes H_2O that is coordinated to the metal cation in the interstitial region. To our knowledge, no water is present in the sheet of the structure (i.e., the region containing the uranyl and phosphate polyhedra) in the autunites presented in this study.

Using thermogravimetric analyses (TGA), the total hydration of synthetic Na autunite and natural meta autunite was quantified. Next, distinct bonding environments for respective water populations were elucidated. Lastly, differential scanning calorimetry (DSC) was used to obtain the enthalpy (ΔH_{hyd}) associated with the release of a given water population from the solid of interest.

2. EXPERIMENTAL

2.1. Chemicals

All chemicals are reagent grade or higher. Deionized (18 MΩ) and boiled water was used in preparations of all solutions. Standards used for ICP-OES analyses were 99.9% purity.

2.2. Synthetic and natural compounds

2.2.1. Synthetic Na autunite: $Na[(UO_2)(PO_4)]\cdot 1.5H_2O$ (c)

Microcrystalline sodium autunite was synthesized according to the method of Zheng et al., 2006. Stoichiometric volumes of 0.05 M H_3PO_4 and 0.1 M $UO_2(NO_3)_2\cdot 6H_2O$ were mixed in a jacketed reaction vessel under N_2 at 70°C. Standardized 0.1 M NaOH was added dropwise to the stirred suspension and the pH was adjusted to approximately 8. The suspension was stirred overnight at 70°C and subsequently allowed to settle. The supernatant was decanted and replaced with degassed 18 MΩ DIW at 70°C (twice), stirred and allowed to settle. The final pH was ca. 7. The final suspension was extracted and vacuum filtered through 0.45-µm Millipore membranes, rinsed three times with boiling DIW, covered and dried overnight at 30°C. Solids were crushed with a mortar and pestle and sieved (sieve number 100) to an approximate 150 µm particle size, placed in 20 mL borosilicate centrifuge vials and stored.

2.2.2. Natural meta autunite: $Ca[(UO_2)(PO_4)]_2\cdot 5.6H_2O)$ (c)

Meta autunite is commercially available from Excalibur Inc., obtained from the Daybreak Mine in northeastern Washington State. In addition to the rigorous characterization of meta autunite conducted in this lab, this mineral has been characterized previously by Wellman (2004). The

mineral was ground to approximately 150um particle size, and separated gravimetrically by repeated washing with DIW according to Wellman (2004) to remove minor accessory components present in this natural material.

2.3. Elemental Analysis

For both meta autunite and sodium autunite, duplicate powder samples of approximately 10 mg were digested in concentrated HNO_3 and diluted to 100 mL in a volumetric flask with DIW. Dissolved metal determination was carried out on a Perkin-Elmer Optima 3200 axial torch inductively-coupled optical emission spectrometer (ICP-OES). For all samples, three replicate intensities were recorded from which the average and standard deviation was calculated.

2.4. Powder x-ray diffraction (PXRD)

PXRD was performed on fine grained samples (~ 150 μm) of Na autunite and Ca meta autunite at room temperature using a Siemens Kristalloflex D500 diffractometer with the following parameters: Copper source (Kα; 1.54018 Å); 35 keV, 30 mA, Kβ filter: Ni; scintillation counter detector; Continuous mode: 0.02d/min; 2θ range: 5-20. The diffractograms were produced using MDI Data Scan 4 and Jade 8 software packages.

2.5. ATR-IR Spectrometry

Measurements were made on solids in this study using a Nicolet 6700 FT-IR spectrometer with an ATR accessory equipped with a ThermoElectron Smart Nexus Orbit single-reflection diamond IRE. Spectra were measured between 4000 and 400 cm^{-1} at 8 cm^{-1} resolution. A total

of 200 scans were averaged for each sample and background. The system was purged with desiccated N_2 at 30 psi. The solid samples were ground with an agate mortar and pestle and sieved to an approximate 150 μm particle size.

2.6. Thermal Analyses (TGA and DSC)

Thermogravimetric analysis (TGA) and differential scanning calorimetry (DSC) were conducted using a Perkin-Elmer TGA-7 and Perkin-Elmer DSC instruments, respectively. The TGA was calibrated with a 10 mg standard weight furnished by Perkin-Elmer. The DSC was calibrated with solid zinc and indium standard materials. For TGA, powders were were crimped inside an aluminum pan and subsequently placed in an open platinum pan for analysis. For DSC, the crimped aluminum pans were inserted directly into the instrument, i.e., no platinum pan was required. For both TGA and DSC, the scan rate was 10^oC/min and the experimental temperature ranged from 25^oC to 500^oC. Approximately 10 mg of solid was used in all of these experiments.

3. DISCUSSION

The differential scanning calorimeter (DSC) measures the power (mW) that is required to maintain equal temperature between the sample and references vessels. When a physical change occurs (i.e. melting) in the sample, heat is absorbed (endothermic reaction) and power must be added to the sample vessel to maintain the same temperature as that of the reference vessel, resulting in a distinct peak in a power vs. temperature profile. The power (W = J/s) is easily converted to heat capacity (J/g·C) when a temperature scan rate (C/s) is applied and the sample weight is known. Thus the heat capacity of the system (Cp) is measured as a function of T for a given scan rate. A local maximum in the profile (Cp_{max}) signals an endothermic dehydration

event and the temperature at this peak of the curve is the temperature of dehydration (T_{hyd}) for that particular event.

The enthalpy associated with this dehydration event, ΔH_{hyd}, is obtained by integrating the area under the curve between the minimum and maximum temperatures:

$$\Delta H_{hyd} = \int Cp\ dt \qquad (1)$$

The TGA allows one to calculate the number of moles that are lost by the solid as a function of temperature. By assimilating both the DSC and TGA data, thermodynamic data for specific hydration events are readily obtainable.

4. RESULTS

4.1 Elemental Analysis (ICP-OES)

The results of chemical digestion of duplicate samples of Na autunite and Ca meta autunite ($Ca[(UO_2)(PO_4)]_2 \cdot 6.5H_2O$) are shown in Table 19.

The concentrations of the dissolved analytes shown in Table 19 are in line with the expected stoichiometry of Ca meta autunite given the experimental uncertainty associated with each analyte. However, sodium autunite exhibits an inordinately high Na concentration. However, since the U/P ratio was in line with the expected stoichiometry, this Na is deemed an impurity that does not have a significant effect on the overall composition of Na autunite. Further characterization of Na autunite including PXRD, ATR-IR and TGA confirm the identity of this phase as discussed below.

Wellman (2004) conducted electron microprobe and ICP analyses (digestion) of natural Ca meta autunite obtained from the same location as the sample in this study. Similar dissolved concentrations were obtained. In addition both the Wellman study and this study observed a variety of trace impurities in the mineral (i.e., Pb, Sr, K, Na). It is likely that some of these impurities are due to clays that may not have been completely removed during the washing procedure of the meta autunite. In addition, Wellman approximated (by weight difference) 6.9 moles of stoichiometric water (no uncertainty given), which is reasonably close to the 6.5 moles obtained by TGA analyses in these studies (Table 19).

Table 19. Chemical digestion data for synthetic Na autunite and natural Ca meta autunite.

Na autunite	**Concentration (M)**	**1 σ**	**Molar Ratio**
Na^{+}	$7.94 \cdot 10^{-4}$	$2.45 \cdot 10^{-5}$	2.22
UO_2^{2+}	$3.70 \cdot 10^{-4}$	$1.73 \cdot 10^{-5}$	1.00
PO_4^{3-}	$3.58 \cdot 10^{-4}$	$5.73 \cdot 10^{-6}$	1.03
H_2O	$5.62 \cdot 10^{-4}$	$2.36 \cdot 10^{-6}$	1.52
Meta autunite	**Concentration (M)**	**1 σ**	**Molar Ratio**
Ca^{2+}	$1.11 \cdot 10^{-4}$	$1.00 \cdot 10^{-5}$	1.00
UO_2^{2+}	$2.36 \cdot 10^{-4}$	$9.58 \cdot 10^{-7}$	2.13
PO_4^{3-}	$2.18 \cdot 10^{-4}$	$3.19 \cdot 10^{-6}$	1.97
H_2O	$7.16 \cdot 10^{-4}$	$6.61 \cdot 10^{-5}$	6.45

4.2 PXRD analysis

Powders of sodium autunite, and calcium meta autunite were prepared as described above and analyzed by PXRD and compared to published powder diffraction files (PDF). In general good agreement is observed between the synthetic Na autunite from this study and the published PXRD pattern of the same phase (Fig. 28). However, some discrepancies are noteworthy. First, the degree of hydration has a significant effect on the d-spacing distances (and 2-theta scattering) due to interlayer swelling in these sheet structures as a function of hydration (Phi-Tham and Columban, 1988; Sowder, 1998). As determined by TGA, the synthetic Na autunite in this study contains approximately 1.5 moles of water (Table 19 and Fig 32). In contrast, the synthetic Na autunite depicted in PDF#29-1284 is a trihydrate - roughly double the stoichiometric water content. Hence, unless a PDF with similar hydration is obtainable, and in this case it was not, shifts in 2-theta scattering degrees are expected. In addition, there are two peaks at 2-theta of ca. 19.5 and 32.5 in the synthetic Na autunite from this study that are not present in the PDF# 29-1284. However, both of these peaks are present in the PDF for synthetic chernikovite (PDF#08-0296). Both being autunites with the same $(UO_2)(PO_4)^-$ structural unit, the only difference between the two phases being interlayer metal occupancies, it is not surprising that these patterns are very similar. It is highly unlikely that Na autunite contains any chernikovite because the latter phase precipitates at very low pH (ca. 1), while the former material requires relatively high synthesis pH (ca. 7). At this pH, insufficient hydronium ions are present to interchange with Na and co-occupy the autunite interlayer. However, these findings clearly illustrate the difficulty of delineating autunites with PXRD alone. Further characterization studies are necessary, such as elemental analysis and IR, as described herein.

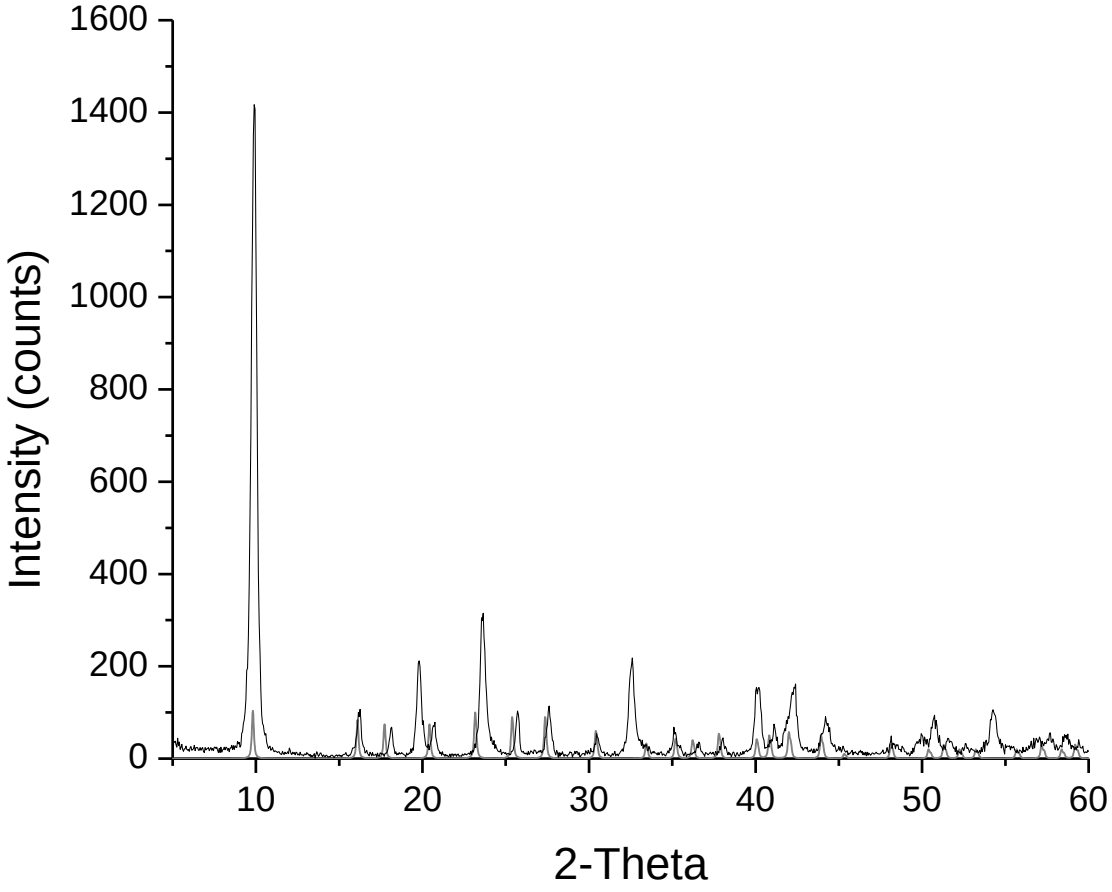

Fig. 28. PXRD profiles of synthetic Na autunite (black) and the corresponding published pattern, PDF # 29-1284 (grey).

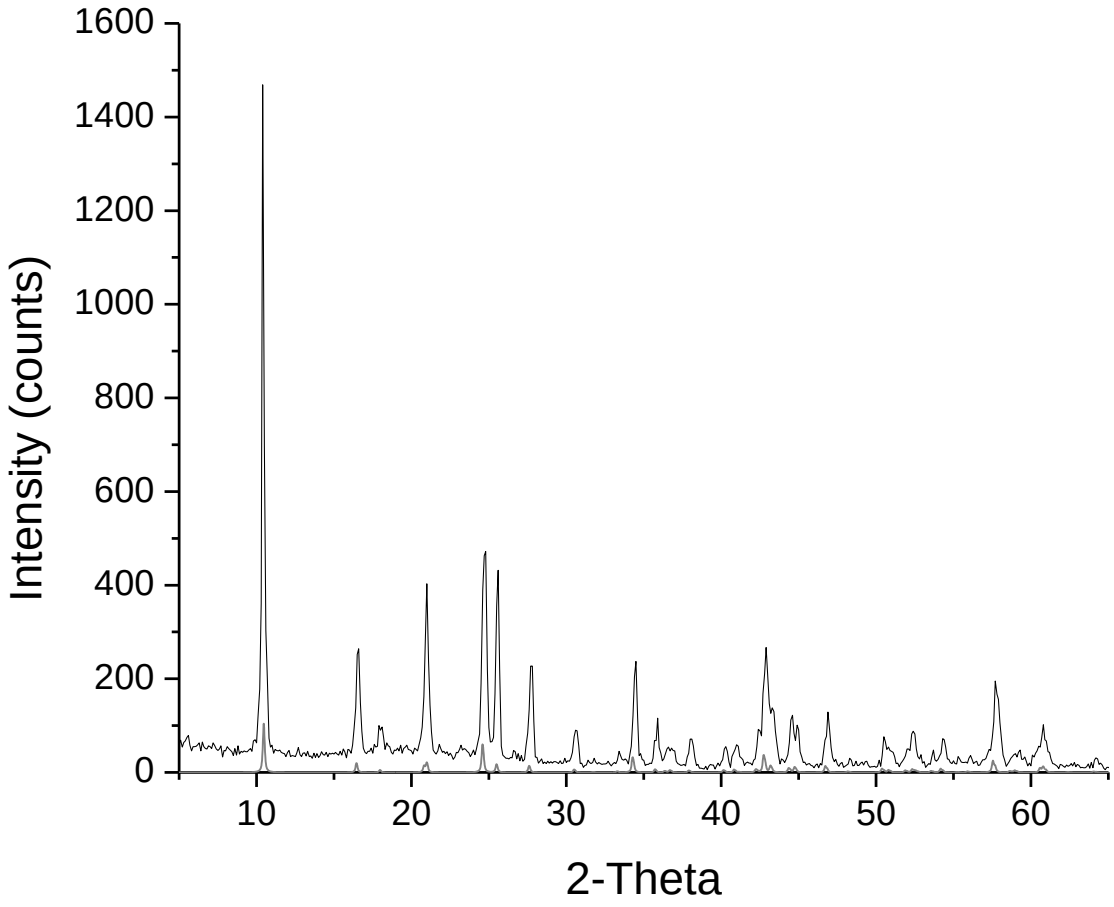

Fig. 29. PXRD profiles of calcium meta autunite (black) and published pattern for calcium meta autunite; PDF # 39-1351 (grey).

The meta autunite sample in this study was compared to a published PXRD pattern of the same phase and excellent agreement was observed (Fig 29).

4.3. ATR-IR Spectrometry

In addition to elemental analysis, TGA and PXRD, ATR-IR was performed on Na autunite and Ca meta autunite. The tentative band assignments of the various components presented herein are in line with published studies (Cejka, 1999 and references therein). The IR spectra are shown in Fig. 30 and the associated band assignments are shown in Table 20.

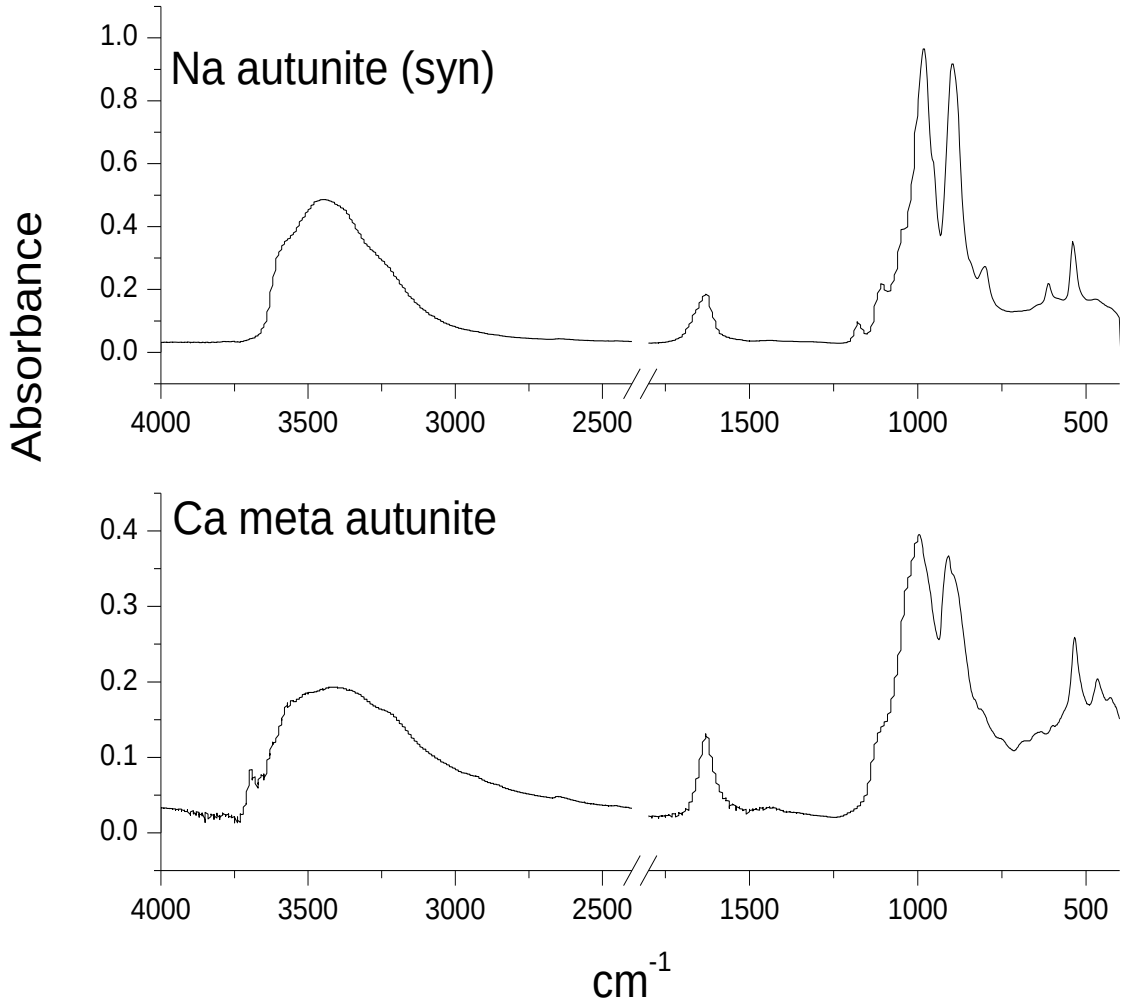

Fig. 30. ATR-IR spectra of synthetic Na autunite and meta autunite in the mid-infrared spectrum.

Table 20. IR absorption bands (in cm^{-1}) of synthetic Na autunite and natural Ca meta autunite corresponding to the spectrum in Fig. 32. s = strong, m = medium, w = weak, v = very, b = broad.

Na autunite	Meta autunite	Assignment
	3696 (m)	νOH
3592 (s,b)	3564 (s,b)	νOH
3435 (s,b)	3410 (s,b)	νOH
	3230 (s,b)	νOH
1630 (s)	1630 (s)	ν2 OH
1179 (w)		ν4 OH
1106 (w)	1112 (vw)	ν3 PO4
980 (vs)	996 (vs)	ν3 PO4
895 (vs)	911 (vs)	ν3 UO2
801 (m)		ν1 UO2
612 (m)		ν4 PO4
533 (s)	535 (s)	ν4 PO4
	466 (m)	ν4 PO4

The spectra of both synthetic and natural autunite samples are very similar. Despite the fact that meta autunite features a rather sharp mode at ca. 3700 cm^{-1} which is attributed to the antisymmetric stretch of water (v3 OH), both show appreciable hydration as evidenced by the broad, rather featureless band from ca. 3700 – 3000 cm^{-1}. This band is actually the result of many overlapping antisymmetric v3, and symmetric, v1 OH modes due to the variety of water bonding environments (e.g., physisorbed, occluded and interstitial) in these phases. The most

intense bands for both phases at ca. 980 cm^{-1} and 996 cm^{-1} for Na autunite and meta autunite respectively are the antisymmetric stretching (v3) PO_4 modes. The v3 modes of uranyl for both phases also are rather intense, and vibrating at similar frequencies (895 cm^{-1} and 911 cm^{-1} respectively). The broader, less intense modes from ca. 1200 to 400 cm-1 observed in the natural sample are likely the result of a coexisting amorphous autunite phase. As the autunites tend to coexist in nature, it also likely that crystalline autunite phases also contain small amorphous contributions, resulting in band broadening due to symmetrically non-equivalent components.

The relative intensity of the H_2O bending (v2 OH) at ca. 1610 cm^{-1} and the aforementioned stretching modes (v3/v1 OH) in the Na autunite spectrum are lower than those observed in meta autunite. This supports the finding that the meta autunite sample is markedly more hydrated than Na autunite (6.5 moles vs. 1.5 moles of stoichiometric water; Table 19).

4.4. Thermal Analyses (TGA and DSC)

For DSC analyses, pure zinc and indium metals were used as quality control (QC) monitors as well as calibration standards. As noted above, prior to each DSC analysis of a selected uranyl compound, in addition to a baseline acquisition, pure zinc was analyzed (from 25^{o}C to 500^{o}C at a 10^{o}C/min scan rate) and the measured enthalpy of fusion of the metal (ΔH_{fus}) was recorded for QC purposes. A representative run is shown in Fig 31. The values depicted in Fig. 31 were obtained by integrating the area under the endothermic curve as described above. The peak temperature (425.7 ^{o}C) is indicated. The bracketed values are the published onset temperature (i.e. melting point) and ΔH_{fus} for pure zinc. Very good agreement is observed with the thermodynamic data obtained from the DSC and the published values (less than 1 % difference).

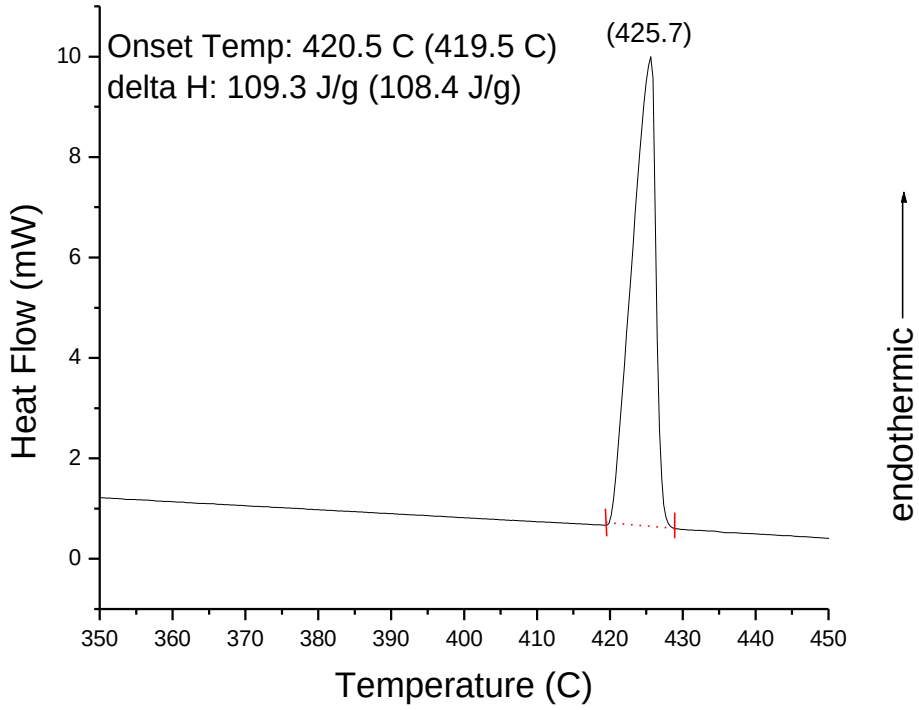

Fig. 31. DSC run of 6.3 mg of zinc. Scan rate: 10°C/min.

Using the complementary data accrued from both TGA and DSC, the stoichiometric number of moles of water and the enthalpy associated with each dehydration mode are obtained. Note: In all cases, excellent agreement was observed between replicate runs with the TGA-7 instrument. In fact, multiple TGA runs were practically indistinguishable. For this reason, only three replicate runs were conducted whereas with the DSC, ten runs were analyzed. In addition, the uncertainty associated with the replicate water loss events in the TGA temperature profiles was negligible (less than 1%). Thus no uncertainty is included with the moles of water released shown in Tables 21 and 22. In contrast, the DSC-7 exhibits relatively high random error. Although the instrument is calibrated routinely, the baseline is markedly different from day to day. In addition, although we have shown in these and other studies that these uranyl phosphates

are crystalline, small amounts of amorphous material may be present, particularly in the synthetic phases. For these reasons, a total of ten replicate DSC runs were completed for each material, and thermodynamic analyses were conducted on each individual run. From these individual runs, ΔH_{hyd} was determined for the different modes of hydration as outlined above. The average and standard deviation was taken of these data resulting in the values shown in Tables 21 and 22 with 1-sigma uncertainty.

The data obtained from both TGA and DSC are shown in Tables 21 and 22 for sodium autunite and meta autunite respectively. The moles of water were obtained by calculating the weight loss between the plateau regions of the thermograms at each dehydration event (Figs. 32 and 33; top panels). These dehydration events in the TGA correspond with the endothermic peaks (T_{hyd}) observed in the DSC (See Figs. 32 and 33 and Tables 21 and 22 respectively). In the case of physisorbed water, a pseudoplateau is observed (TGA; lowest temperature events) suggesting that these water molecules are gradually (i.e. continuously) released from the surface of these solids.

The temperature ranges that encompass the endothermic peaks that were integrated to obtain ΔH_{hyd} are shown in Tables 21 and 22. These temperatures represent the average range of the ten replicate runs for each of the three dehydration modes (physisorption, occlusion, interstitial-coordinated). The standard deviation (1σ) of the average of the ten runs is indicated in brackets.

The relatively abrupt dehydration event (both phases) evidenced by the slope changes in the TGA and corresponding endothermic peaks in the DSC are followed by a slower diffusion of water from the solid; hence a gradual, shallow slope is observed as the temperature is elevated past the peak of the event. In the case of the lowest temperature event (both phases) only a

shallow negative slope is observed. This is inferred to be physisorbed water and in this case only gradual diffusion from the surface of the solid is expected. Additionally, although a distinct plateau is not evident at the highest temperature, the final data points in all runs had indeed leveled off. Although it is possible that tightly bound waters may be still be present at 773 K, it is more likely that sodium autunite and meta autunite are almost completely dehydrated at 773 K.

An exothermic event at ca. 313 K is observed in almost all of the DSC runs in this study (Figs. 32 and 33; bottom panels). And although a broad and relatively minor endothermic event may be evidenced at a slightly higher temperature (325 K and 328 K, sodium autunite and meta autunite respectively), which may be attributed to the release of surface water (physisorption), it is unclear if this is an artifact of the DSC, particularly in the case of Na autunite, since two events are so close together. Interestingly a small, rather continuous weight loss event is evidenced in the corresponding TGA profile at roughly the same temperature in Na autunite. However, due to the exothermic artifact, the event at ca. 325 K was not included in the thermodynamic analysis of sodium autunite.

In comparing natural meta autunite and synthetic sodium autunite some observations are noteworthy. The major dehydration event in meta autunite, tentatively attributed to occluded water at 372 K, is followed by a smaller mode at 446 K which is attributed to coordinated water within the interstitial region of the mineral. In contrast, the major dehydration mode observed in Na autunite (422 K) is the highest temperature event and is likewise assigned as interstitial-coordinated water.

The thermodynamic data presented in Tables 21 and 22 yield somewhat surprising results. In the case of sodium autunite, the largest enthalpic contribution is attributed to interstitial-coordinated water, a finding that seems intuitive since the strongest (and thus most

thermodynamically favorable) bonds should require the highest temperature to break. Interestingly, this trend is not observed in the natural sample. As mentioned previously, the most significant meta autunite dehydration event is attributed to occluded water, with an enthalpy of -134 KJ/mol.

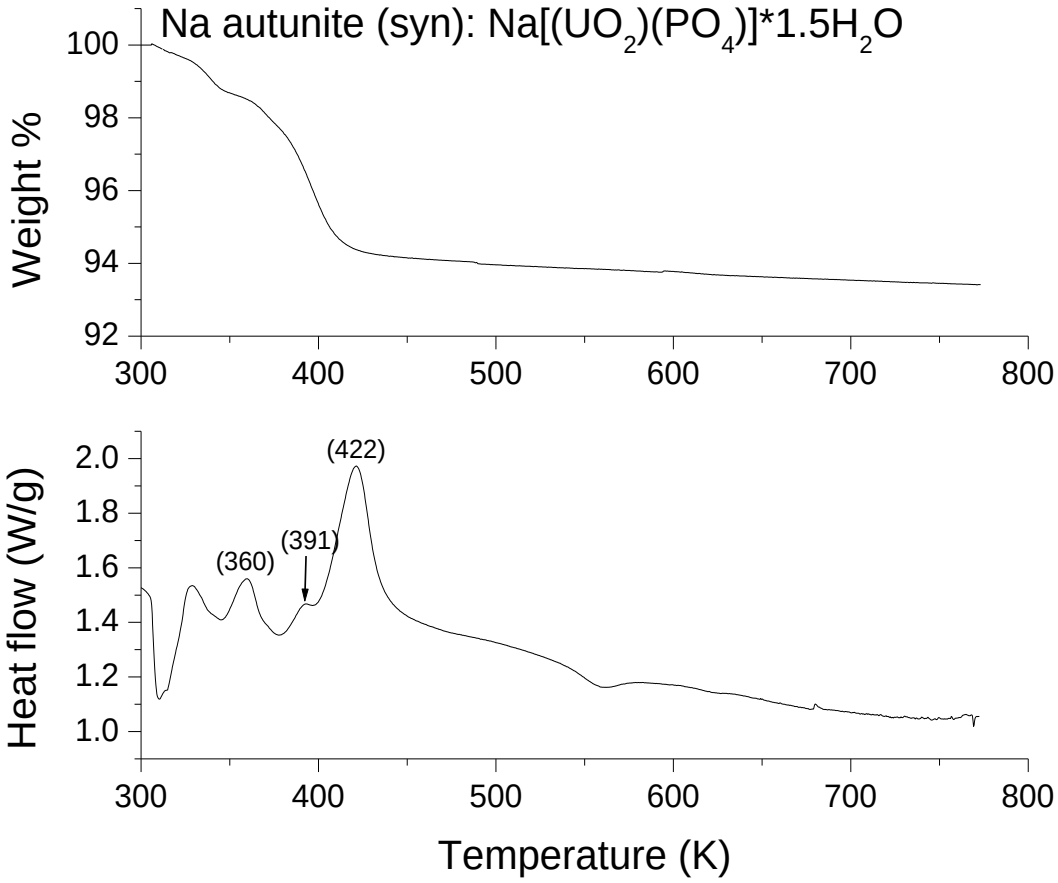

Fig. 32. Average of three TGA (top) and ten DSC (bottom) temperature profiles of synthetic sodium autunite at a scan rate of 10^{o}C/min.

From the thermal data of sodium autunite the following dehydration reactions are inferred for physisorbed (P), occluded (O) and interstitial-coordinated water (IC):

$Na[(UO_2)(PO_4)]\cdot 1.52H_2O(s) \leftrightarrow Na[(UO_2)(PO_4)]\cdot 1.40H_2O(s) + 0.12\ H_2O$ (P)

$Na[(UO_2)(PO_4)]\cdot 1.40H_2O(s) \leftrightarrow Na[(UO_2)(PO_4)]\cdot 1.15H_2O(s) + 0.25\ H_2O$ (O)

$Na[(UO_2)(PO_4)]\cdot 1.15H_2O(s) \leftrightarrow Na[(UO_2)(PO_4)](s) + 1.15\ H_2O$ (IC)

The results of these calculations for each dehydration event are depicted in Table 21.

Table 21. Thermodynamic data obtained for synthetic sodium autunite from ten replicate DSC runs and three replicate TGA runs. Bracketed values represent 1-sigma of the average of ten replicates from DSC analyses.

Dehydration Mode	**Endothermic Temperature Range (K)**	**T_{hyd} (K)**	**ΔH_{hyd} (KJ/mol)**	**Moles H_2O released**
Physisorbed	345- 377	360 (1)	-17.6 (4.6)	0.12
Occluded	378 – 398	391 (1)	-2.6 (0.4)	0.25
Coordinated	398 - 444	422 (1)	-72.6 (5.6)	1.15

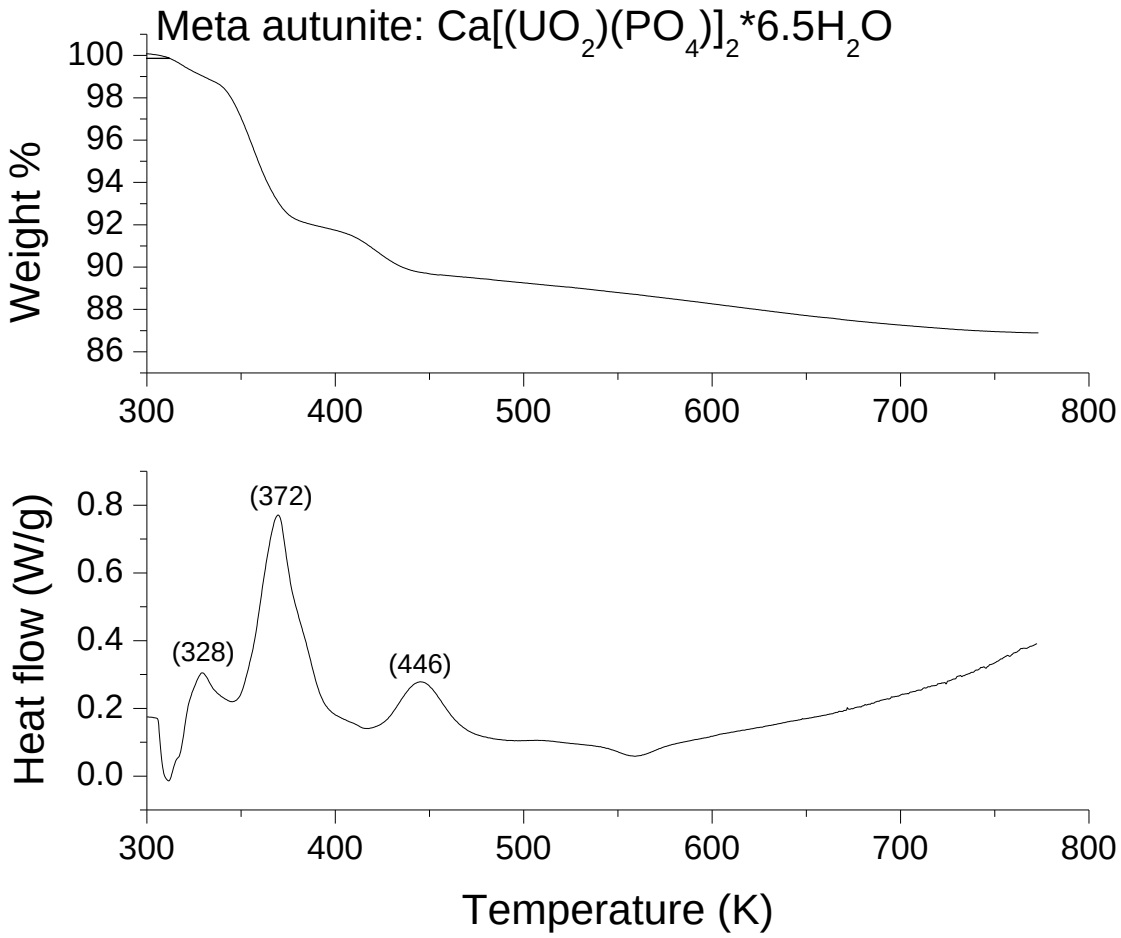

Fig. 33. Average of three TGA (top) and ten DSC (bottom) temperature profiles of meta autunite at a scan rate of 10^{o}C/min.

From these thermal data of meta autunite the following dehydration reactions are inferred for physisorbed (P), occluded (O) and interstitial-coordinated water (IC):

$Ca[(UO_2)(PO_4)]_2 \cdot 6.45H_2O(s) \leftrightarrow Ca[(UO_2)(PO_4)]_2 \cdot 5.61H_2O(s) + 0.84\ H_2O$ (P)

$Ca[(UO_2)(PO_4)]_2 \cdot 5.61H_2O(s) \leftrightarrow Ca[(UO_2)(PO_4)]_2 \cdot 2.21\ H_2O + 3.40\ H_2O$ (O)

$Ca[(UO_2)(PO_4)]_2 \cdot 2.21\ H_2O(s) \leftrightarrow Ca[(UO_2)(PO_4)]_2(s) + 2.21\ H_2O$ (IC)

The results of these calculations for each dehydration event are depicted in Table 22.

Table 22. Thermodynamic data obtained for natural meta autunite from ten replicate DSC runs and three replicate TGA runs. Bracketed values represent 1-sigma of the average of ten replicates from DSC analyses.

Dehydration Mode	**Endothermic Temperature Range (K)**	**T_{hyd} (K)**	**ΔH_{hyd} (KJ/mol)**	**Moles H_2O released**
Physisorbed	320 - 345	328 (2)	-15.2 (5.6)	0.84
Occluded	345 – 400	372 (3)	-134.1 (16)	3.40
Coordinated	420 - 475	446 (4)	-38.3 (4.2)	2.21

5. CONCLUSION

To our knowledge, the experimentally determined thermodynamic data for solid phase hydration obtained from TGA and DSC are the first to be reported. We believe that this new method of treating distinct water modes as separate thermodynamic entities provides unique insights into the specific bonding environments of water in these hydrated uranyl phosphates. This approach can be applied to all of the hydrated uranyl solid phases, potentially resulting in more accurate determinations of the thermodynamic properties of these phases, particularly for uranyl solid phases for which thermodynamic data are either lacking or unreliable. These studies provide the basis for further studies aimed toward obtaining the free energies of hydration associated with distinct water populations in these solids.

References

Clark, S.B., Ewing, R.C., Schaumloffel, J.C. (1998) A method to predict free energies of formation of mineral phases in the U(VI) – SiO_2 – H_2O system. *J. Alloys Comp.* **271-273.** (189-193).

Cejka, J. Reviews in Mineralogy Vol. 38. Eds. Burns, P.C., Finch, R. (1999) 522-622.

Chen, F., Ewing, R.C., Clark, S.B. (1999) The gibbs free energies and enthalpies of formation of U6+ phases: An empirical method of prediction. *Amer. Mineral.* **84.** (650-664).

Finch, R. (1997) Thermodynamic stabilities of U(VI) minerals: Estimated and observed relationships. *Mat. Res. Symp. Proc.* **465.** (1185-1192).

Grenthe, I., Fuger, J., Konings, R.J.M., Lemire, R.J., Muller, A.B., Nguyen-Trung, C., Warner, H. (1992) Chemical Thermodynamics of Uranium. 713 pp. North-Holland, Amsterdam.

Hawthorne, F.C. (1992) The role of OH and H_2O in oxide and oxysalt minerals. *Zeit. Fur Kristall*. **201**, 183-206.

Hawthorne, F.C., Schindler, M. (2008) Understanding the weakly bonded constituents in oxysalt minerals. *Zeit. Fur Kristall*. **223**, 41-68.

Pham-Thi, M., Colomban, Ph. J. Less-Common Met. (1989) 189-216.

Schindler, M., Hawthorne, F.C. (2008) The stereochemistry and chemical composition of interstitial complexes in uranyl-oxysalt minerals. *Can. Mineral*. **46**, 467-501.

Sowder, A.G. PhD dissertation. (1998) Clemson University.

Tardy, Y., Garrels, R.M. (1974) A method of estimating the Gibbs free energies of formation of layer silicates. *Geochim. Cosmochim. Acta* **38**. 1101-1116.

Tardy, Y., Garrels, R.M. (1976)) Prediction of Gibbs free energies of formation- I. Relationships among Gibbs free energies of formation of hydroxides, oxides and aqueous ions. *Geochim. Cosmochim. Acta* **40**. 1051-1056.

Tardy, Y., Garrels, R.M. (1977) Prediction of Gibbs free energies of formation- II. Monovalent and divalent metal silicates. *Geochim. Cosmochim. Acta* **41**. 87-92.

Wellman, D.M. (2004) Environmental availability of uranium from secondary uranyl minerals. PhD dissertation, Washington State University.

CHAPTER SEVEN

Partitioning of Neodymium into Hydroxylapatite ($Ca_5(PO_4)_3OH$)

Christopher R. Armstrong and Sue B. Clark*

Dept. of Chemistry, Washington State University, Pullman, WA 99164, U.S.A.

Contaminant remediation / Apatite / Radioactive waste disposal / Neodymium / ATR-IR

Summary. In this report the uptake of Nd onto hydroxylapatite (HA: $Ca_5(PO_4)_3OH$) as a function of pH at 25°C was investigated. The incorporation of Nd into HA was monitored with inductively-coupled plasma optical emission spectrometry (ICP-OES), powder x-ray diffraction (PXRD), and attenuated total reflection infrared (ATR-IR) spectroscopy. Probing both solid and solution phases provides insight into the mechanism(s) of lanthanide partitioning to hydroxylapatite. These results show almost complete removal (~ 99%) of 85 ppm Nd throughout the pH range of ca. 4.5 to 10, and the process for Nd uptake is pH dependent. At lower pH (ca. 4) a discrete nanocrystalline $NdPO_4 \cdot xH_2O$ solid precipitated, whereas at pH 10, Nd partitioning was attributed to isormorphic substitution.

* To whom correspondence should be addressed. Tel. 509-335-2911. Email: s_clark@wsu.edu

1. INTRODUCTION

Apatite ($Ca_5(PO_4)_3X$; where X = Cl, F or OH) incorporates a host of polyvalent metal ions and anionic species while retaining the same overall crystal structure (i.e., isomorphic substitution). In fact, apatite accommodates half of the periodic table into its lattice arrangement [1]. Although transition metal ion sequestration by apatite has been extensively studied, mechanistic studies that define the process(es) of actinide and lanthanide interactions with apatite are rather limited.

One of the earlier U-apatite studies [2] to address this issue determined that hydroxylapatite (HA) dissolution and subsequent UO_2 precipitation effectively removed uranyl from solution. In separate studies of apatite remediation in an oxidizing environment, Fuller et al. [3,4] concluded that the predominant uptake mechanism of U onto apatite was sorption followed by solubility-controlled precipitation resulting in almost complete U removal from the system. In a similar study of uranyl uptake by apatite, Ohnuki et al. [5] observed sorption followed by surface mineralization as autunite (uranyl phosphate) precipitated on the surface of apatite, even though the bulk solution was undersaturated with respect to autunite. Hence, U uptake was not solubility controlled. Workers from Florida State University [6] were the first to present sorption edge curves as a function of pH for uranyl sorption onto hydroxylapatite. Knox et al. [7] investigated Eu^{3+} (and uranyl) uptake by apatite and observed complete metal removal by apatite, which they also attributed to a sorption mechanism. In a related study, Martin et al. [8] specified a cation-exchange process between lanthanide cations (Eu^{3+} and La^{3+}) and Ca^{2+} at the apatite surface.

Thus, previous studies suggest that both electrostatic and solubility driving forces are at play in f-element uptake by HA; and these processes may not be mutually exclusive, and are not well understood. In addition to sample purity, synthetic vs. natural apatite and variations in surface charge, metal ion properties such as oxidation state, ionic radius, coordination number and hard/soft acid character all contribute to the process(es) by which a given metal ion is

sequestered by apatite. Moreover, the physico-chemical conditions of the system, e.g., solution/suspension pH, ionic strength and temperature are also very important factors [9 and references therein].

The goal of this present study is to use a variety of analytical techniques to investigate the mechanism(s) of uptake of Nd^{3+} by HA. Neodymium was investigated in this study because lanthanides are common uranium fission products. Moreover, Nd^{3+} is a reasonable chemical analogue of trivalent actinides such as Am^{3+}, Cm^{3+} and Pu^{3+} [10, 11, 12, 13].

In the present contribution, the removal of Nd by HA as a function of pH was monitored using inductively-coupled optical emission (ICP-OES) spectrometry, attenuated total reflection infrared spectroscopy (ATR-IR) and powder x-ray diffraction (PXRD) with the main objective of elucidating the predominant uptake mechanism(s) in this process. Here we show, for the first time, a complementary analytical approach, probing both the solid and solution phases, that affords an effective and reliable interpretation of Nd^{3+}- HA- H_2O systems as a function of pH.

2. EXPERMIMENTAL METHODS AND MATERIALS

2.1 Experimental

All chemicals are reagent grade or higher. To minimize dissolved CO_2, all solutions were prepared with boiled 18 MΩ doubly deionized (DDI) water. The 85 ppm Nd used in these experiments was prepared from neodymium nitrate salt (Alfa). Standards used for elemental analyses were of 99.9% purity. The synthetic hydroxylapatite is commercially available (Sigma-Aldrich). Initially, the HA powder was rinsed repeatedly with degassed 18 MΩ DDI water and vacuum filtered. The dried HA was subsequently ground with a mortar and pestle to an approximate 250 μm particle size and stored in a polystyrene bottle with a screw top. The HA-Nd solids were prepared in a similar manner as that of HA. Suspension pH was measured with a

Metrohm pH meter (Model 713) equipped with a Ross combination pH electrode (Orion Model 8102). Prior to each use, the pH electrode was calibrated with NIST standards. HA dissolution and Nd incorporation was monitored by adjusting the pH with standardized 0.1 M KOH or 0.1 M HCl solutions via potentiometric titrations using a Mettler-Toledo^{TM} autotitrator. The duration of individual experimental runs was typically between five and ten hours. Suspensions were constantly stirred under an inert N_2 atmosphere at 25^{o}C in a jacketed reaction vessel. Approximately 2 mL samples were extracted via a polystyrene syringe and polypropylene tubing at roughly 0.5 pH unit intervals. The samples were forced through a 0.2 um polyethersulfone (PES) filter, acidified with concentrated HNO_3, diluted and stored in 15 mL centrifuge tubes for subsequent ICP-OES analyses. The reaction vessel, stir bar and all the tubing were soaked in a 5% HNO_3 acid bath between titration runs. In all cases, duplicate experiments were conducted and the experimental conditions (e.g., temperature, ionic strength etc.) were held constant.

2.2. Dissolved metal concentrations

Aqueous Nd, Ca and P concentrations were obtained using a Perkin-Elmer Optima 3200 axial torch ICP-OES with a precision of approximately 5%. For all samples, three replicate intensities were recorded from which the average and standard deviation was calculated.

2.3 ATR-IR Spectrometry

Measurements were made on solids in this study using a Nicolet 6700 FT-IR spectrometer with an ATR accessory equipped with a ThermoElectron Smart Nexus Orbit single-reflection diamond IRE. Spectra were measured between 4000 and 400 cm^{-1} at 8 cm^{-1} resolution. A total of 200 scans were averaged for each sample and background. The system was purged with desiccated N_2 at 30 psi. As noted above, the solid samples were ground with an agate mortar and pestle and sieved to an approximate 250 μm particle size.

2.4 Powder x-ray diffraction (PXRD)

PXRD was performed on fine grained samples (~ 250 μm) of HA under ambient conditions using a Siemens Kristalloflex D500 diffractometer with the following parameters: Copper source (Kα; 1.54018 Å); 35 keV, 30 mA, Kβ filter: Ni; scintillation counter detector; Continuous mode: 0.02d/min; 2θ range: 5-55. The powders were sprinkled onto a zero background glass slide containing a very thin layer of Vaseline® (smear mount) to reduce preferred orientation. The XRD instrument was calibrated prior to each analysis with a corundum (α-Al_2O_3) external standard. The diffractograms were produced using supporting MDI Data Scan 4 and Jade 8 software packages.

3. RESULTS AND DISCUSSION

3.1 Hydroxylapatite dissolution and Nd partitioning as a function of pH

The dissolution of HA ($Ca_5(PO_4)_3OH$) as a function of pH at 25°C is shown in Fig. 34 (open symbols). In all cases, elevated concentrations of both Ca and P were observed below pH ca. 8, demonstrating that HA undergoes dissolution when the pH of the system drops below its point of zero charge (PZC) [14]. At pH values below 5, nearly complete HA dissolution was observed, in agreement with other studies [15, 16].

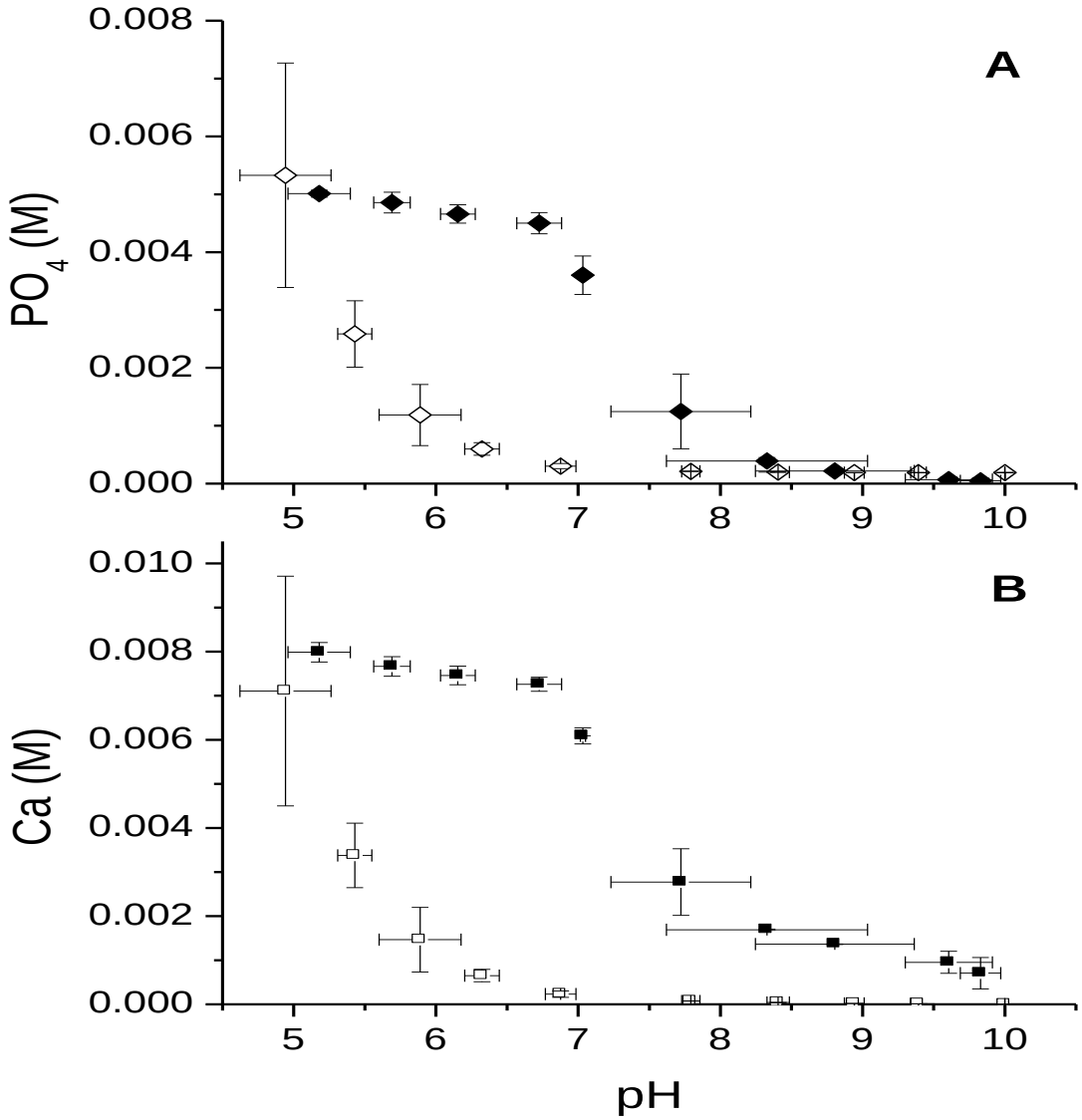

Fig. 34. Panel A: Dissolved PO_4 concentrations as a function of pH in suspensions of 1.0g/L of HA only (open diamonds) and 1.0g/L of HA equilibrated with 85 ppm Nd (solid diamonds). Panel B: Corresponding Ca dissolution observed in HA only (open squares) and HA equilibrated with 85 ppm Nd (solid squares). Suspensions were equilibrated in 0.1M KCl media at 25^{o}C under a N_2 atmosphere. Error bars represent 1σ for duplicate runs.

When Nd is present in the system, the dissolution behavior of HA is markedly different as a function of pH (Fig. 34, solid symbols). These Nd-HA systems did not exhibit a sorption edge as reported by others [7]. In these studies, near complete (~ 99%) Nd removal was observed throughout the pH range of these experiments (Fig. 35, panel B). It should be noted that several of the Nd values are approximately 0.1 ppm, which is approaching the ICP-OES limit of detection for Nd (401.225 nm emission line) of 0.05 ± 0.01 ppm.

Although Nd removal was nearly complete at all pH values, the presence of Nd in the system had a rather significant, and pH dependent, effect on HA dissolution. A marked increase in both Ca and P was observed over a wide pH range (Fig. 34). At circumneutral pHs (ca. 6 – 8), Nd had the most pronounced effect on Ca dissolution where a concentration increase of approximately 0.007M was observed at ca. pH 6.8. Although a corresponding enhancement in P dissolution was also observed due to 85 ppm Nd, it occurred over a narrower pH range (pH ca. 5.5 to 8.5) than that of Ca. Significantly, above pH ca. 8, considerable Ca dissolution was observed, whereas in HA-only systems Ca concentrations remained very low in this pH range. These results suggest that isomorphic Nd^{3+}- Ca^{2+} substitution may be taking place above pH 8.

In addition to the Nd-HA (binary) systems, duplicate 85 ppm Nd, 0.10M KCl experiments were carried out and are shown in Fig. 35, panel A. These Nd runs serve as a blank comparison of the binary systems; and thus provide insights into Nd solubility under the conditions of this study without the influence of HA.

Aqueous Nd concentrations remained relatively constant from ca. pH 2 to 7, but dropped sharply above pH ca. 7.5. The Nd dissolution data shown in Fig. 35 are in reasonable agreement with the PHREEQC^{TM} [17] prediction (Fig. 35, crosses) based upon thermodynamic data shown in Table 25 (Appendix A). The free Nd^{3+} species predominates in solution until ca. pH 7.5

where Nd hydrolysis and subsequent $Nd(OH)_3$ precipitation controls Nd solubility. These results clearly show the significant effect that HA has on the removal of Nd from solution, particularly below pH ca. 7.

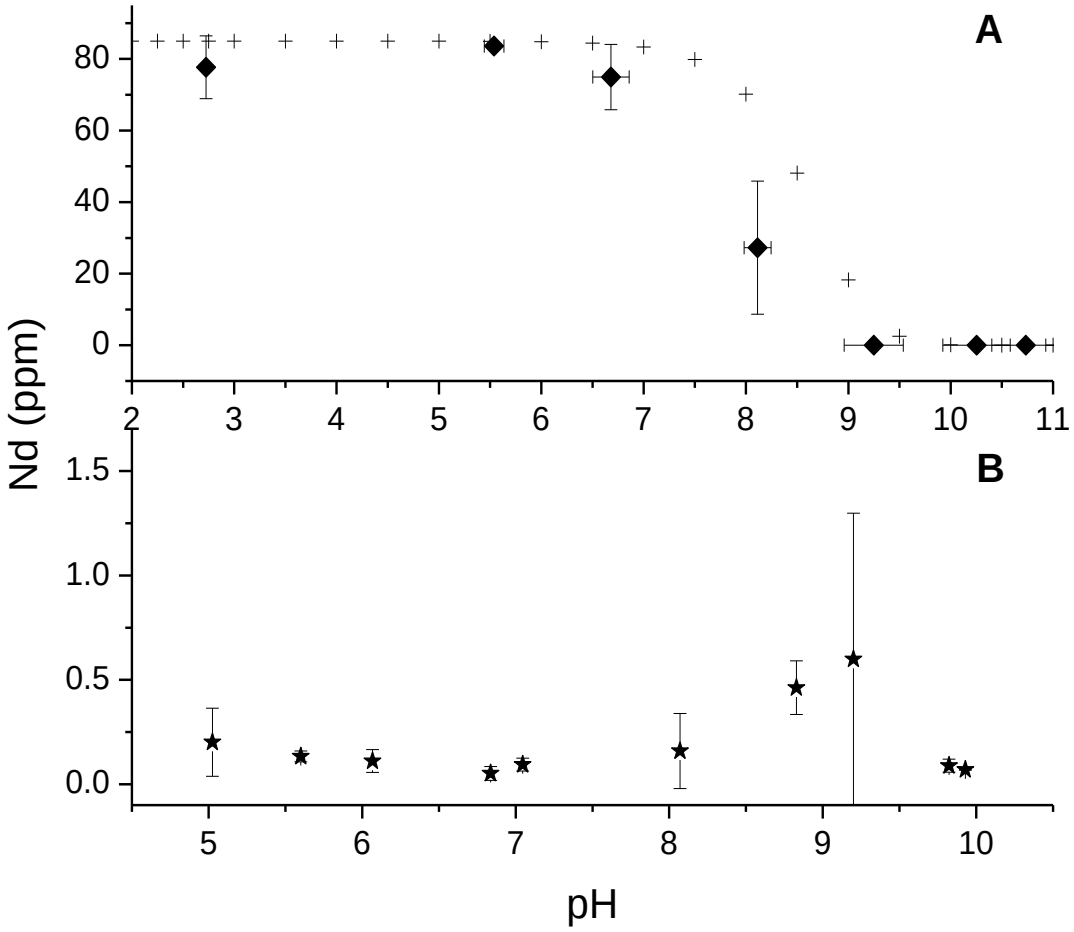

Fig. 35. Dissolved Nd as a function of pH at 25°C under a N_2 atmosphere (Panel A, diamonds). Starting system: 85 ppm Nd, 0.10M KCl. Error bars represent 1σ for duplicate runs. Crosses in Panel A represent Nd solubility modeled in PHREEQC™. Loss of Nd from solution above ca. pH 7 is largely due to Nd hydrolysis and subsequent $Nd(OH)_3$ precipitation. Panel B shows final Nd concentrations in a binary system (initially 85 ppm Nd equilibrated with HA in 0.1M KCl).

3.2. ATR-IR analysis

To examine the pH dependence of Nd uptake by HA, separate HA solids (with ~ 85 ppm Nd incorporated into each sample) equilibrated separately at pH 4 and 10 at 25^{o}C in 0.1M KCl were analyzed with ATR-IR. These spectra are shown in Fig. 36, panels B and C respectively. In addition, ATR-IR was also performed on synthetic $NdPO_4$ and HA and these spectra are also shown in Fig. 36, panels A and D respectively. The corresponding band assignments for HA and $NdPO_4$ shown in Table 23 are consistent with published IR studies of these respective phases [18, 19].

The phosphate vibrational modes dominate the IR spectra of all of these solids. In fact, the spectra of HA and $NdPO_4$ are very similar, as these phases feature three PO_4 modes that vibrate at the same frequencies (shown in red in Fig. 36).

The IR spectra of HA and the HA+Nd are virtually identical (Fig. 36), suggesting that no structural changes have occurred to HA due to the uptake of 85 ppm Nd at pH 10. Thus, under alkaline conditions where the net surface charge of HA is expected to be negative [14], it is likely that Nd partitioning is largely due to electrostatically-driven isomorphic substitution, as noted above.

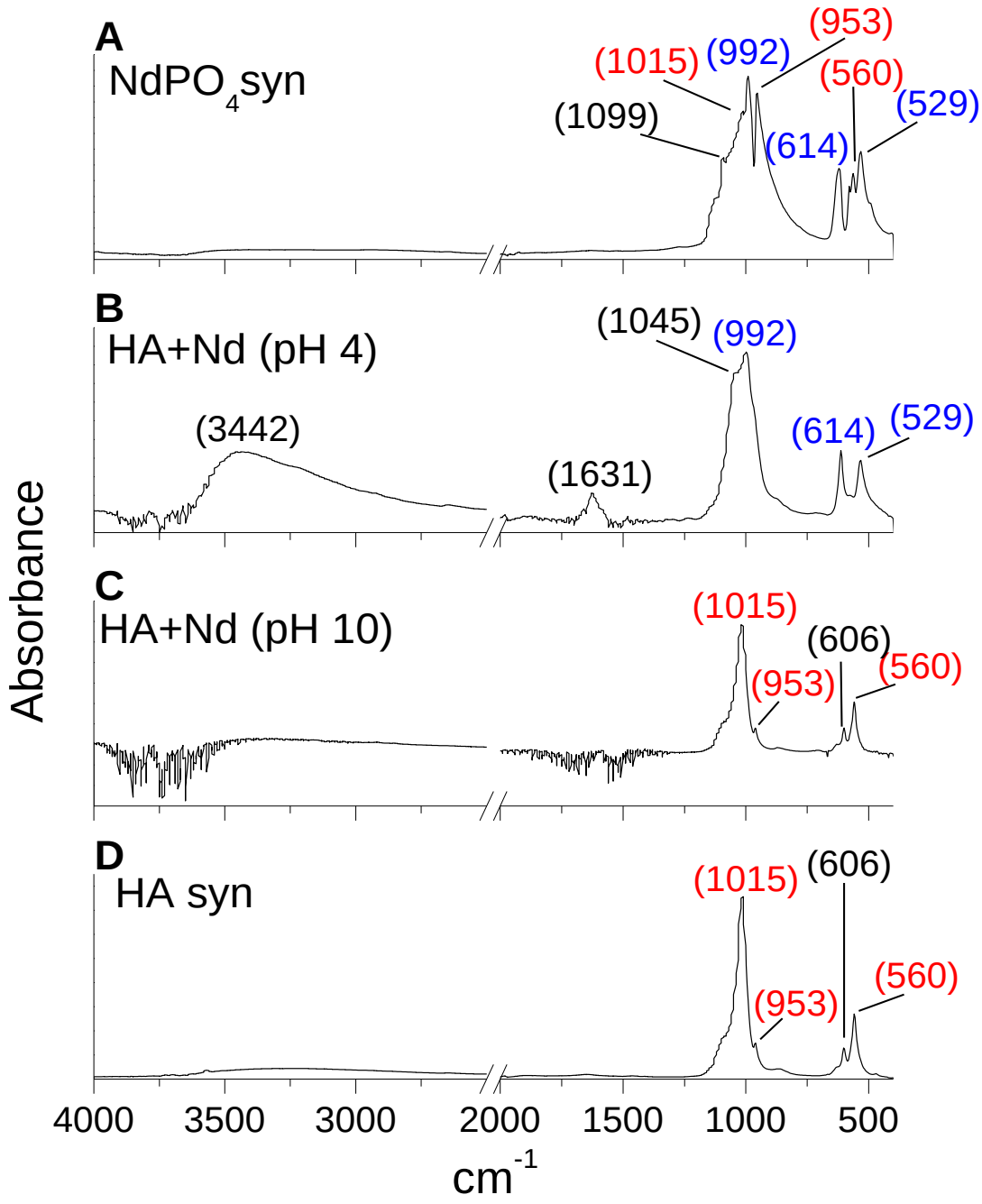

Fig. 36. IR spectra of $NdPO_4$ (Panel A); HA with 85 ppm Nd incorporation and a final equilibrated suspension pH of ca. 4 (Panel B); HA with 85 ppm Nd incorporation in a suspense

on pH of ca. 10 (Panel C); and synthetic HA (Panel D). No spectral features were observed in the region between ca. 2500 cm^{-1} and 2000 cm^{-1}; therefore part of this region was omitted for clarity.

Table 23. Band assignments (in cm^{-1}) for HA, $NdPO_4$ and HA with 85 ppm Nd incorporation at pH 4. The corresponding spectra are displayed in Fig. 36.

HA	**$NdPO_4$**	**HA+Nd (pH 4)**	**Group**	**Vibrational Mode**
560	529	529	PO_4^{3-}	Bend; ν4
606	560		PO_4^{3-}	Bend; ν4
	614	614	PO_4^{3-}	Bend; ν4
863			P-OH	Stretch; ν1/ν3
953	953		PO_4^{3-}	Sym. stretch; ν1
1015	992	992	PO_4^{3-}	Antisym. stretch; ν3
	1015	1045	PO_4^{3-}	Antisym. stretch; ν3
	1099		PO_4^{3-}	Antisym. stretch; ν3
		1631	H_2O	Bend; ν2
		3442	OH	Stretch; ν1/ν3

Although the IR spectrum of the HA-Nd solid equilibrated at pH 10 is indistinguishable from that of HA, it is very different than the solid equilibrated at pH 4. In fact, three of the phosphate modes of the pH 4 solid match those of $NdPO_4$ (Alfa) shown in blue in Fig. 36. These findings suggest that at low pH $NdPO_4$ precipitation has occurred at the expense of HA. Interestingly, the pH 4 HA-Nd solid is hydrated, as evidenced by the broad stretching (v1/v3) OH modes centered at 3442 cm^{-1} and a bending (v2 H_2O) mode centered at 1631 cm^{-1}. This finding is indicative of the precipitation of a neodymium phosphate phase with the rhabdophane crystal structure, $NdPO_4 \cdot xH_2O$ [20].

3.3 PXRD

Samples of HA, $NdPO_4$, HA-Nd (pH 4) and HA-Nd (pH 10) were analyzed by PXRD and, where possible, compared to published powder diffraction files (PDFs). The HA diffractogram, shown in Fig. 37, is in very good agreement with PDF # 76-0694 (bottom panel). In addition, the $NdPO_4$ sample also shown in Fig. 37 is consistent with PDF # 46-1328 (top panel).

The Nd-HA pH 10 diffractogram is also shown in Fig. 37 (bottom panel). Although the reflections are both broader and more intense, the XRD pattern of the Nd-HA pH 10 sample is in good agreement with both the synthetic HA and the synthetic HA PDF# 76-0694 (bottom panel), suggesting that Nd is not having a significant effect on the HA structure, thus further supporting the hypothesis of isomorphic Nd-Ca substitution, at pH 10. The increased intensity in the Nd-HA sample relative to HA may be the result of an increase in the crystal size in the former phase due to the fact that the equilibrated HA-Nd suspension was allowed to age unstirred for several months prior to PXRD analysis. In a separate study in this laboratory, a similar increase in XRD

peak intensity was observed due to hydrothermal treatment of HA; and scanning electron microscopy (SEM) results strongly suggested an increase in macrocrystallinity.

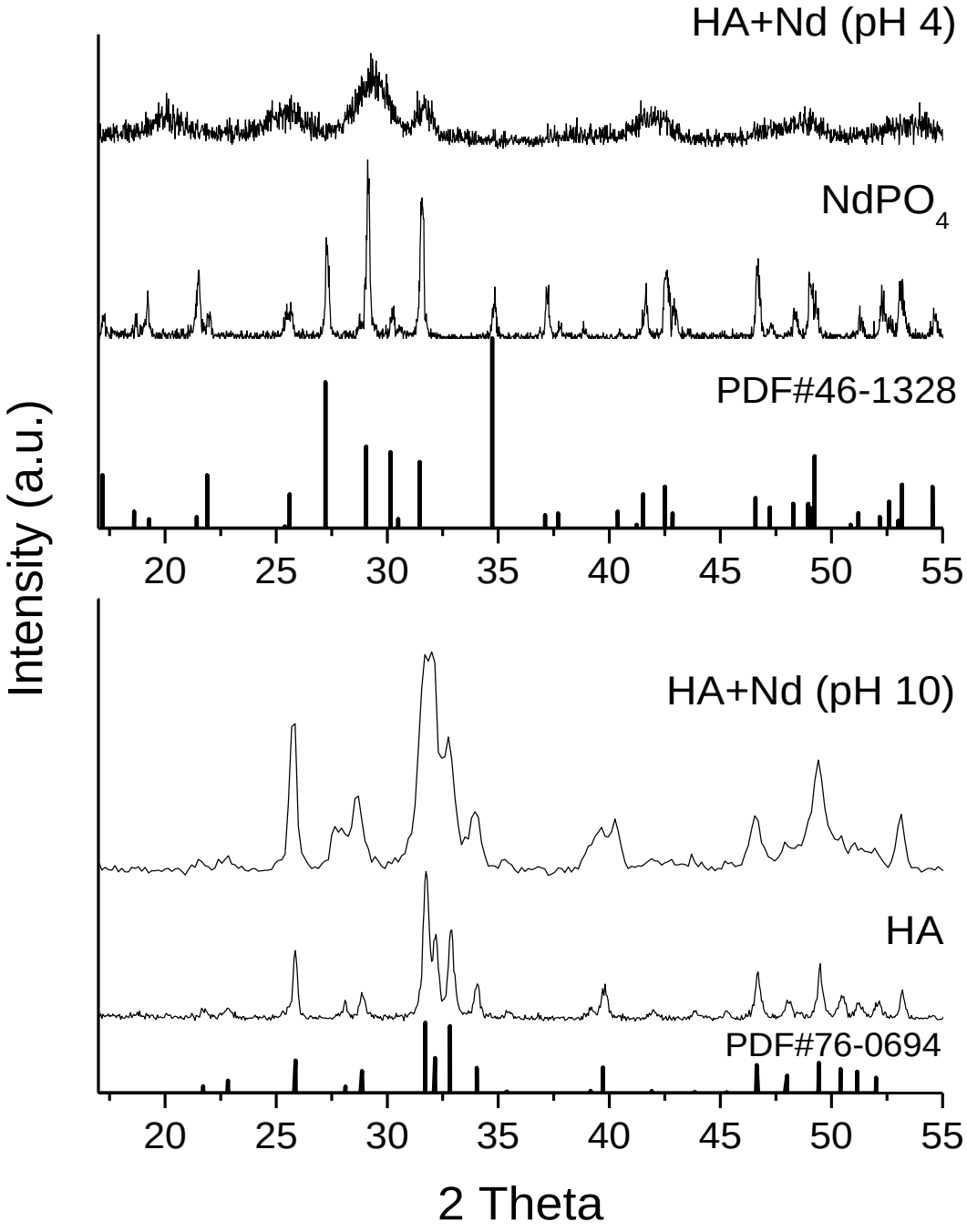

Fig. 37. XRD patterns of HA and Nd solid equilibrated at pH 10 (top), HA (middle) and HA PDF# 76-0694 (bottom).

The Nd-HA pH 4 diffractogram is shown in Fig. 37 (top). Several of the major peaks of the pH 4 solid match those of the synthetic $NdPO_4$ (Alfa) and the corresponding $NdPO_4$ PDF # 46-1328 (top panel). Additionally, the only peaks that match the HA PDF # 76-0694 are also consistent with the $NdPO_4$ pattern. Hence, similarities between HA and $NdPO_4$ due to the PO_4 ligand evidenced in the IR spectrum (Fig. 36) also emerge in the PXRD data. Thus, in agreement with IR data, $NdPO_4$ appears to be the predominant phase in the Nd-HA pH 4 solid.

Additionally, in marked contrast to the pH 10 residue, the pH 4 powder features broad XRD peaks with relatively low intensity suggesting a significant contribution of nanocrystalline material. This finding is consistent with the rapid precipitation (e.g., tens of minutes) of $NdPO_4$ at pH 4 hypothesized in this study. Moreover, our results are in agreement with Köhler et al. [20] who also reported the precipitation of nanocrystalline rhabdophane ($NdPO_4 \cdot xH_2O$) on the surface of apatite.

3.4. Chemical digestion

To monitor the molar ratios of Nd, Ca and P in the solids in this study, duplicate samples of roughly 10 mg were digested in concentrated nitric acid and diluted to 100 mL in a volumetric flask with boiled 18 MΩ DDI water and subsequently analyzed for metal ion content with ICP-OES. The molar ratios of each analyte represent the average of the duplicate samples (± 5%) for each solid and are shown in Table 24.

Table 24. Molar ratios of the solids in this study with approximately 5% uncertainty.

Sample	Nd^{3+}	Ca^{2+}	PO_4^{3-}	Ca/P
pH 4	5.97	1.00	7.76	0.13
pH 10	1.00	11.79	7.45	1.58
HA	-	1.57	1.00	1.57

The Nd:Ca:P ratio (6:1:8) of the HA-Nd pH 4 sample confirms that most of the solid is $NdPO_4$, since the molar proportion of Nd is significantly higher than that of Ca. These molar proportions also support IR and PXRD data showing $NdPO_4 \cdot xH_2O$ precipitation at the expense of HA; since a 1:1 Nd:P ratio allows the remaining P to be accounted for in HA. In contrast, the incorporation of 85 ppm Nd into the HA-Nd pH 10 solid has a negligible effect on the Ca:P molar ratio (1.58) relative to that of HA (1.57). Thus, in agreement with IR and PXRD data, chemical digestion data strongly suggests that the isomorphic substitution of Ca by Nd is the most likely uptake mechanism at pH 10.

4. SUMMARY

In this report, the uptake of Nd onto HA as a function of pH at 25^{o}C was investigated; and a complementary analytical approach using ICP-OES, ATR-IR and PXRD to monitor Nd incorporation into HA was presented. Our results show near complete Nd removal from solution throughout the pH range of this study (ca. 4.5 to 10). Although Nd sequestration was evidently independent of pH, the pathway of Nd partitioning into HA was determined to be pH dependent. Below pH ca. 5, the precipitation of discrete, nanocrystalline $NdPO_4 \cdot xH_2O$ was observed. In

contrast, at pH 10, no structural alterations of HA were evidenced; thus we conclude that isomorphic Nd-Ca substitution to be the most likely Nd partitioning pathway.

These studies show that although apatite amendments offer promise for in situ actinide remediation, pH plays a key role in the chemistry of these aqueous systems. Sorption mechanisms are thus envisaged in pHs above the PZC of HA (ca. 8) where (1) cation exchange is likely to take place and, (2) HA solubility is relatively low. In contrast, HA dissolution and subsequent actinide phosphate precipitation is expected below the PZC and particularly below pH 5.

Acknowledgements

This work was supported primarily by the U.S. Department of Energy, Basic Energy Sciences, Heavy Element Chemistry program, contract DE-FG02-06ER15782. In addition, SBC and CRA gratefully acknowledge support from the Joint Domestic Nuclear Detection Office-National Science Foundation: Academic Research Initiative (ARI), contract number ECCS-0833548 during the preparation of this manuscript.

References

1. Hughes, J.M., Rakovan, J. In: Phosphates*: Geochemical, geobiological, and Materials Importance*. Kohn, M.J., Rakovan J., Hughes, J.M., Eds. *Reviews in Mineralogy, 48,* Mineralogical Society of America: Washington, DC. (2002).

2. Jeanjean, J., Rouchaud, J.C., Tran, L., Federoff, M. J. Radioanal. Nucl. Chem., Lett. **6**, 529 (1995).

3. Fuller, C.C, Bargar, J.R., Davis, J.A., Piana, M.J. Environ. Sci. Technol. **36,** 158 (2002).

4. Fuller, C.C, Bargar, J.R., Davis, J.A. Environ. Sci. Technol. **37,** 4642 (2003).

5. Ohnuki, T., Kozai, N., Samadfam, M., Yasuda, R., Yamamoto, S., Narumi, K., Naramoto, H., Murakami, T. Chem. Geol. **211,** 1 (2004).

6. Thakur, P., Moore, R.C., Choppin, G.R. Radiochim. Acta **93,** 385 (2005).

7. Knox, A.S., Kaplan, D.I., Adriano, D.C., Hinton, T.G., Wilson, M.D. J. Environ. Qual. **32,** 515 (2003).

8. Martin, P., Carlot, G., Chevarier, A., Den-Auwer, C., Panczer, G. J. Nucl. Mat. **275,** 268 (1999).

9. Xu, Y., Schwartz, F.W. Environ. Sci. Technol. **28,** 1472 (1994).

10. Choppin, G.R. J. Less-Common Metals **93,** 323 (1983).

11. Choppin, G.R. J. Less-Common Met. **126,** 307 (1986).

12. Choppin, G.R. Mar. Chem. **28,** 19 (1989).

13. Nitsche, H. Basic research for assessment of geologic nuclear waste repositories: What solubility and speciation studies of transuranium elements can tell us. Paper presented at the

Intl. Symp. on Sci. Basis for Nuclear Waste Management, Boston, MA Conf. Proceedings (1990).

14. Armstrong, C.R. PhD dissertation. Washington State University, USA (2009).

15. Dorozhkin, S.V. J. Coll. Int. Sci. **191,** 489 (1997).

16. Dorozhkin, S.V. J. Cryst. Growth **182,** 133 (1997).

17. Parkhurst, D.L., Appelo, C.A.J. Users guide to PHREEQC (Version 2). A computer program for speciation, batch reaction, one dimensional transport and inverse geochemical calculations. U.S. Geological Survey Water Resources Investigations Report 99-4259 (1999).

18. Fowler, B.O. Inorg. Chem. **13,** 194 (1974).

19. Ross, S.D. In: The Infrared Spectra of Minerals. Ed. Farmer, V.C. Mineralogical Society, London (1974).

20. Köhler, S.J., Harouiya, N., Chaïrat, C., Oelkers, E.H. Chem. Geol. **222,** 168 (2005).

Appendix. A

Table 25. The following thermodynamic data were used with PHREEQC^{TM} in this study.

	log *K*
K_w	-14
$Nd^{3+} + H_2O \leftrightarrow NdOH^{2+} + H^+$	-8.16[a]
$Nd^{3+} + 2H_2O \leftrightarrow Nd(OH)_2^+ + 2H^+$	-17.04[a]
$Nd^{3+} + 3H_2O \leftrightarrow Nd(OH)_3^0 + H^+$	-26.41[a]
$Nd^{3+} + 3H_2O \leftrightarrow Nd(OH)_3(s) + H^+$	-18.10[b]
$Nd^{3+} + 4H_2O \leftrightarrow Nd(OH)_4^- + 4H^+$	-37.1[a]
$Nd^{3+} + Cl^- \leftrightarrow NdCl^{2+}$	0.32[a]
$Nd^{3+} + 2Cl^- \leftrightarrow NdCl_2^+$	0.02[a]
$Nd^{3+} + PO_4^{3-} \leftrightarrow NdPO_4$	11.8[b]
$Nd^{3+} + PO_4^{3-} \leftrightarrow NdPO_4(s)$	26.2[f]
$KCl(s) \leftrightarrow K^+ + Cl^-$	0.7
$K^+ + H_2O \leftrightarrow KOH + H^+$	-14.46[c]
$Ca^{2+} + 2H^+ + PO_4^{3-} \leftrightarrow CaH_2PO_4^+$	20.961[d]
$Ca^{2+} + H^+ + PO_4^{3-} \leftrightarrow CaHPO_4$	15.085[d]
$Ca^{2+} + PO_4^{3-} \leftrightarrow CaPO_4^-$	6.459[d]
$5Ca^{2+} + 3PO_4^{3-} + H_2O \leftrightarrow Ca_5(PO_4)_3OH(s)$	40.459[e]
$H_2PO_4^- + H_2O \leftrightarrow PO_4^{3-} + 2H^+$	-19.553[e]
$H_3PO_4 \leftrightarrow PO_4^{3-} + 3H^+$	-21.702[d]
$HPO_4^{2-} \leftrightarrow PO_4^{3-} + H^+$	-12.346[e]
$Ca^{2+} + H_2O \leftrightarrow CaOH^+ + H^+$	-12.78[e]

[a] Haas, J.R., Shock, E.L., Sassani, D.C. Geochim. Cosmochim. Acta **59,** 4329 (1995).

[b] Spahiu and Bruno. Swedish Nuclear Fuel and Waste Management Co. SKB Technical Report 95-35, **35**, (1995).

[c] Baes and Mesmer. *Hydrolysis of Cations*. John Wiley and Sons, New York, N.Y. (1976).

[d] Guillamont, R., Fanghanel, T., Fuger, J., Grenthe, I., Neck, V., Palmer, D.A., Rand, M.H. Update on the Chemical Thermodynamics of Uranium, Neptunium, Plutonium, Americium, and Technetium. Chemical Thermodynamics, Vol. 5. Elsevier Science Publishers, Amsterdam, North-Holland (2003).

[e] Wateq4F

[f] Liu, X. and Byrne, R.H. Geochim. Cosmochim. Acta **61,** 1625 (1997).

Appendix B.

HA surface area determination

Surface area calculations are necessary in order to approximate the number of sorbate molecules that bind to a given surface. The sorptive properties of a given material in equilibrium with an aqueous solution are proportional to its surface area and specific surface charge (Langmuir, 1997). This experimentally determined value is also a very important input parameter in geochemical codes, without which, sorption modeling would likely not be possible. Also, small discrepancies in surface area values (e.g., values obtained from solid phases with varying purity and crystallinity) can result in erroneous data. Therefore, surface area and surface charge investigations are fundamental preliminary steps in most mineral-water studies.

The surface area (m^2/g) of synthetic hydroxylapatite purchased from Sigma-Aldrich was determined using two different approaches: 1) The BET method; 2) The methylene blue (MB) method according to Giles and Nakhwa (1962). The results of HA surface area determination by the BET method can be seen in Table 26. Surface area determination by the MB method was conducted as follows.

Experiments were conducted by varying the concentrations of aqueous MB while keeping the HA concentration constant at 1.0g/L. Batch sorption experiments were conducted at circumneutral pH. Samples were equilibrated overnight by agitation at 275 rpm, filtered with 0.2 μm PES filters and analyzed by a Cary 14 UV-VIS spectrophotometer at 665 nm. A calibration curve was obtained for known MB concentrations (Fig. 38).

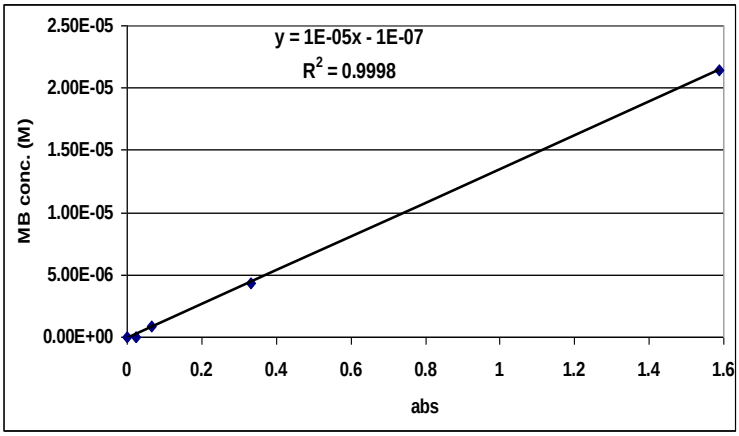

Fig. 38. Calibration curve for UV-VIS studies of HA surface area determination using the MB adsorption method.

At low MB concentrations complete MB adsorption (and thus complete MB removal from solution) was observed. At sufficiently high MB concentrations, all the HA surface sites were saturated with adsorbed MB and thus a plateau was observed. The plateau region was assumed to correspond to a saturated monolayer of MB on the surface of HA. Adsorbed MB (mmole MB/g HA) was plotted versus MB in solution (mM). The surface area (SA) was calculated as follows:

$$SA\ (m^2/g) = Y_{MB} \times N \times A_{MB} \times 10^{21} \quad (1)$$

where Y_{MB} = MB adsorbed (mmole/g)

N = Avogadro's #

A_{MB} = surface area covered by one MB molecule = $^{*}1.20\ nm^2$

[*] Determined experimentally by Giles and Nakhwa (1962).

The results of this and other studies are displayed in Table 26. With the exception of the Bell and coworkers (1972) study, the calculated surface area of 51.6m^2/g is comparable to other studies. It should be noted that the other studies obtained surface area data via the BET method.

Table 26. Comparison of various HA surface area values.

Study	HA Surface Area (m^2/g)	Technique
Xu and Schwartz, 1994	77.0 ± 0.4	BET
Duc et al., 2002	70	BET
Fuller et al., 2002	56	BET
Gomez del Rio et al., 2004	51.8	BET
Krestou et al., 2004	65	BET
Bell et al., 1972	26.6	BET
This study	111.74 ±1.31	BET
This study	51.6 ± 2.4	MB

The MB technique involves the adsorption of an aqueous solute (MB) onto the HA surface. By contrast, the BET method involves gas phase adsorption (typically N_2). The general morphology of the HA is amorphous with rounded aggregated particles. Such particles may not provide a flat surface to which the relatively large MB molecule can sorb. It is possible that the MB molecule may not be capable of forming a monolayer on the surface of the Sigma-Aldrich HA. By contrast the much smaller gaseous N_2 (0.162 nm^2; Brunauer et al., 1938) is more likely to sorb on the surface and in the pore spaces of these HA particles, thereby resulting in a higher calculated

surface area. This hypothesis could be tested by conducting BET and MB analyses on the Parr bomb HA samples. The flat, plate-like surfaces of the Parr bomb HA samples may provide relatively similar sorbent surfaces for both N_2 and the larger MB molecule. As such, closer agreement between the calculated surface area values using both methods is expected.

Appendix C.

HA surface charge and PZC determination

Many natural and synthetic mineral phases exhibit a pH dependent surface charge. That is, the surface of the mineral in contact with the bulk solution typically exhibits a positive net charge at sufficiently low pH primarily due to protonation of surface sites and a negative net charge at high pH chiefly due to deprotonation. The point of zero charge (PZC) is the pH at which the *net* surface charge is zero. The PZC is independent of ionic strength; thus, titrations conducted with varying ionic strength tend to converge at the PZC (Fig. 39). For systems involving the adsorption of solutes other than H^+, the PZC allows one to qualitatively predict the pH range of optimal metal or ligand adsorption.

The specific surface charge of HA was determined experimentally by conducting potentiometric titrations using a Mettler-Toledo autotitrator. A 200 mL solution of either 0.01M or 0.1M KCl was mixed with 0.20 g of HA and allowed to equilibrate overnight under N_2 atmosphere at 25^0 C in a jacketed borosilicate reaction vessel connected to a Thermo-Haake circulating water (and propylene glycol) bath. A Ross combination glass electrode was calibrated with standard solutions of either KOH and KCl or HCl and KCl attaining ionic strengths of 0.01M or 0.1M. Therefore, activity coefficients were assumed to be unity and pcH (designated hereafter as pH) was measured for all the experiments. In all cases, titrants of standardized 0.1M KOH for forward titrations and 0.1M HCl for reverse titrations were used.

The surface charge of HA was determined as a function of pH using the following equations (Stumm, 1992).

Mean surface charge:

$$Q \text{ (mol/kg)} = (C_A - C_B + [OH-] - [H+])/a \qquad (2)$$

where C_A and C_B = molar concentrations of acid and base respectively

a = quantity of solid (kg/L)

If the surface area is known, the *specific* surface charge (C/m^2) is thus obtainable:

$$\sigma = QF/s \qquad (3)$$

where F = Faraday's constant (94,680 C/mol)

s = surface area (predetermined value of 51.6 m^2/kg used)

The specific surface charge (C/m^2) as a function of pH for HA is shown in Fig. 39. Separate titrations with 0.1M and 0.01M KCl were conducted.

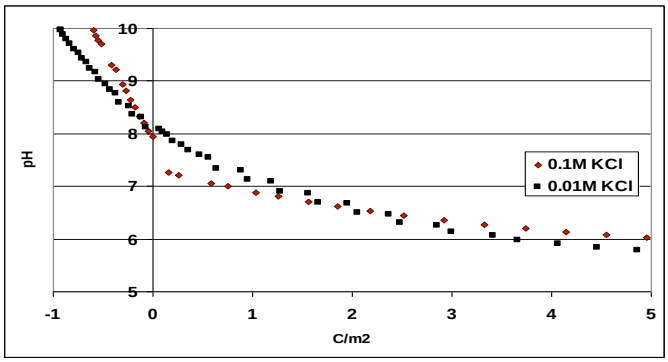

Fig. 39. HA surface charge and PZC.

Both runs converge roughly at pH 8, indicating an approximate point of zero charge (PZC) for hydroxylapatite. Based on these results we can assume the HA surface to be positively charged below ca. pH 8 and negatively charged above ca. pH 8. Others studies involving similar systems

can be seen in Table 27. It should be noted that an additional titration run using another ionic strength (e.g, 0.001M) would be desirable to obtain a more accurate and precise PZC assessment.

At this point it is unclear why the above curves cross at ca. $C/m^2 = 2.2$. Dissolution of HA occurring below pH 8 could be a significant factor. These data represent single runs. In addition, the uncertainty value in Table 27 is only an estimate based upon the scatter in Fig. 39. Replicate runs (at each ionic strength) are planned to more accurately determine the uncertainty of these data points.

Table. 27. Comparison of literature values of the PZC of hydroxylapatite.

Study	**Solid/Sol. (g/25mL)**	**Electrolyte**	**Equilibration time (hr)**	**pH at PZC**
Bell et al., 1972	0.1	KCl	16	8.6 ± 0.1
Harding et al., 2005	0.5	KCl	?	7.3 ± 0.1
This Study	0.1	KCl	24	7.9 ± 0.5

CHAPTER EIGHT

CONCLUSION

The overall goal of this study was to conduct a rigorous investigation into the chemistry of various hydrated uranyl phosphates. These phases are important primarily from an environmental remediation perspective. Here we have attempted to model natural processes where *f*-elements are expected to interact with phosphates in aqueous systems. Although it has been known for some time that phosphate solid phases resulting from both natural and anthropogenic means are highly recalcitrant, and, generally speaking, expected to effectively sequester *f*-elements, the thermodynamic properties and fundamental structure of these phases are not well understood. For these reasons, we have undertaken primarily a characterization and thermodynamic investigation of selected hydrated uranyl phosphates. Highlights of the findings in this study are as follows.

We synthesized and characterized a mixed lanthanide-actinide phosphate, namely francoisite-(Nd) and discussed the viability of encountering such a phase in scenarios where low level radioactive waste or spent nuclear fuel comes in contact with aqueous phosphate (Chapter Two).

We illustrated problems associated with characterizing hydrated uranyl phosphates with powder XRD alone; instead we argued that a complementary approach is required and a viable and effective strategy is outlined (Chapter Three). We propose that implementing the strategy outlined therein will afford greater confidence in data obtained from experimental thermodynamic studies such as solubility and sorption.

The complete conversion of one hydrated uranyl phophate into another, namely chernikovite to TDT is reported and a fundamental structural transformation is observed

(Chapter Four). In this study the importance of rigorously characterizing these synthetic uranyl materials is underscored since chernikovite and TDT can be easily confused during synthesis, potentially leading to highly erroneous thermodynamic interpretations.

Thermodynamic data for most uranyl-bearing materials are lacking at elevated temperatures; and, to obtain a more complete understanding of the chemical equilibria in nuclear waste packages, studies above room temperature are required. We investigated the temperature dependence of the solubility of TDT, at 23 and 50^{o}C. The temperature dependence was notable at some, but not all of the ionic strengths investigated (Chapter Five). In systems with ionic strengths higher than 0.5m $NaClO_4$, i.e., 1.0 to 5.0m, the conversion of TDT to Na autunite was observed.

A novel thermodynamic technique is presented in Chapter Six, wherein differential scanning calorimetry is used to determine the enthalpy associated with discrete hydration events, arising from distinct water populations in two hydrated uranyl phosphates, namely synthetic Na autunite and natural Ca autunite. We feel that this novel approach can be applied to a wide array of hydrated solids, not just uranyl-bearing materials, particularly more soluble solids, i.e., $CuSO_4 \bullet 5H_2O$, since the Gibbs free energy associated with these hydration events likely represents a more significant contribution to the overall free energy of formation.

The complete sequestration of aqueous Nd by hydroxylapatite throughout a wide pH range was presented in Chapter Seven. Thus, in this contribution we showed that metal uptake by this phosphate was pH independent. However we demonstrated that the *mechanism* of uptake was pH-dependent, with precipitation of discrete $NdPO_4(s)$ taking place at pHs below 5, and Nd sorption occuring at ca. pH 10.